

Politecnico di Torino

ScuDo
Scuola di Dottorato ~ Doctoral School
WHAT YOU ARE, TAKES YOU FAR

Doctoral Dissertation
Doctoral Program in Electrical, Electronics and Communications Engineering
(38^{th}cycle)

Bio-Impedance Measurements for Plants Health Evaluation

By

Federico Cum

******

Supervisor(s):
Prof. Danilo Demarchi, Supervisor
Prof. Umberto Garlando, Co-Supervisor

Doctoral Examination Committee:
Prof. ODEDEYI Temitope Oluseun Referee, University College London
Prof. MAZZA Marco, Referee, Hes-So Fribourg
Prof. MIGUEZ Matias, University of Uruguay

Politecnico di Torino
2026

Declaration

I hereby declare that, the contents and organization of this dissertation constitute my own original work and does not compromise in any way the rights of third parties, including those relating to the security of personal data.

Federico Cum
2026

* This dissertation is presented in partial fulfillment of the requirements for **Ph.D. degree** in the Graduate School of Politecnico di Torino (ScuDo).

Acknowledgements

Abstract

In recent years, smart agriculture has experienced significant growth, driven by the need to optimize resource use and improve crop resilience amidst climate change. This dissertation evaluates the diagnostic potential and practical limitations of a low cost, in vivo sensing approach based on plant stem electrical behavior, specifically a simplified parameter referred to as *stem frequency*, which is strongly correlated with stem electrical impedance. While previous studies demonstrated the potential of bio-electrical sensing, they were largely restricted to short term laboratory setups or high cost, complex impedance analyzer. A key gap in prior research was the lack of long term, multi environment validation and accounting of high biological heterogeneity.

This thesis addresses these gaps through a multi stage validation campaign spanning controlled, semi controlled, and real world agricultural scenarios. Initial climate chamber trials established that under optimal hydration, stem frequency tightly tracks ambient microclimatic drivers such as Vapor Pressure Deficit (VPD); however, this environmental coupling breaks down under water deficit, where signal dynamics align with soil water potential. Subsequently, a greenhouse campaign involving 73 tomato plants evaluated the system under both abiotic (drought) and biotic (*Fusarium oxysporum*) stress conditions. Utilizing linear mixed effects modeling adjusted for short term temporal autocorrelation (via a second-order autoregressive $AR(2)$ structure on a 20-minute sampling interval combined with daily cycles), the study demonstrated a statistically significant population level decline in stem frequency under water deficit ($p < 0.05$). Conversely, biotic stress induced by *Fusarium* showed no statistically separable signal once serial correlation was properly controlled. Unsupervised Dynamic Time Warping (DTW) time series clustering further highlighted high inter plant variability, revealing that raw signals cannot currently serve as standalone diagnostic classifiers for individual plants.

Finally, a multi season field deployment in a commercial apple orchard demonstrated the operational durability, electrical stability, and seasonal consistency of the embedded sensors over more than a full year, confirming that stem frequency follows plant dynamics across phenological transitions.

Overall, this work demonstrates that while stem frequency is not yet ready for uncalibrated, stress type-specific disease diagnosis, it represents a promising, highly scalable, and cost effective tool for tracking plant water status. These findings establish a realistic baseline for the technology, highlighting the need for future hardware refinements and multivariate modeling to advance real time plant health monitoring.

Contents

List of Figures **x**

List of Tables **xv**

1 Introduction **1**

1.1 Motivation and Research Objectives 2

2 Monitoring crop health **6**

2.1 Introduction 6

2.2 Crop monitoring 9

2.3 Indirect Methods for plant health 10

2.4 Direct Methods 12

2.4.1 Plant Imaging 13

2.4.2 Sap Flow Measurements 14

2.4.3 Fylloclip 15

2.4.4 Organic Electrochemical Transistors (OECT) 16

2.4.5 Impedance Monitoring and stem/trunk frequency 17

3 Materials and Methods **19**

3.1 Experimental Environments 19

3.1.1 Climate Chamber 19

3.1.2 Greenhouse 22
3.1.3 Open Field 22
3.2 Sensor System and Data Acquisition 23
3.2.1 Stem Frequency: a simplified impedance reading method . . 24
3.2.2 Soil Water Potential measurement 25
3.2.3 Camera System 26

4 Climatic Chamber Experiments 29
4.1 Introduction 29
4.2 Response to Environmental Variables of Tomato Plants 30
4.2.1 Temperature Analysis 35
4.2.2 Relative Humidity Analysis 39
4.2.3 Stratified Analysis 41
4.2.4 Vapour Pressure Deficit 42
4.2.5 Causality Analysis 45
4.3 Response under water stress 46
4.4 Photoperiod Analysis 49
4.4.1 Experimental profile 50
4.4.2 Relationship between Stem Frequency and Leaf Area 60

5 Greenhouse Experiments 71
5.1 Introduction 71
5.2 Tomato stress analysis 72
5.2.1 Different baseline measurements 74
5.2.2 Long Term Analysis 76
5.2.3 Clustering 88

6 Open Field Long Term Measurements 101

6.1 Experimental Setup 102
6.2 Methodology 103
6.2.1 Wound Healing after insertion 104
6.3 Data Collection Results and Analysis 105
6.3.1 Summary and Main Limitations 109

7 Conclusions and future works **111**
7.1 Synthesis of Experimental Findings 111
7.2 Explicit Statement of Original Contributions 112
7.3 Demonstrated Capabilities vs. Unproven Hypotheses 112
7.4 Methodological Limitations 113
7.5 Future Work and Research Outlook 114

References **115**

List of Figures

2.1 Schematic representation of plant health monitoring: primary abiotic and biotic stressors converge into overlapping physiological responses, which are in turn detected by specific direct or indirect sensing techniques. 9

2.2 Water balance example 11

2.3 Sap flow measurement principle. Courtesy of [1] 14

2.4 FylloClip sensor 15

2.5 Image from [2] 16

3.1 Main characteristics of employed climatic chambers 20

3.2 Manual characterization of climate chamber light intensity 21

3.3 Courtesy of [3]. Schematic of a *LMC555* based 50% oscillator with plant in the loop. 24

3.4 Experimental setup for relaxation oscillator applied to plant's stem . 25

3.5 Readout circuit for the Watermark sensor [4] 26

3.6 Camera-based monitoring setup inside the climate chamber. Up to 4 plants can be monitored simultaneously. 27

4.1 Climatic chamber conditions 31

4.2 Overall view if the data collected over the experimental period. The top panel shows the measured stem frequency. The middle panel presents the corresponding soil water potential. The bottom panel illustrates the applied environmental conditions, temperature and relative humidity, alongside the calculated VPD. Areas with a light orange background indicate periods when the light source was active. Note that the period approximately from *2025-03-15* to *2025-04-01* presents missing data from climatic chamber. This period will not be considered during the following analysis but it is still included in the visualization for completeness. 33

4.3 Visualization of the behaviour of VPD against the imposed temperature and RH. 35

4.4 Scatter plot representing chamber air temperature (°C) against normalized stem frequency with equation 4.5 for each of the plants under test. "X" markers in the plots indicate that the sample was with light turned off. 36

4.5 Stem frequency data for both plants under test and corresponding detrending results. Image also shows data that has no corresponding environmental measurements. This data is excluded from the following analysis. 37

4.6 Scatter plot representing chamber air temperature (°C) against normalized stem frequency with equation 4.5 , as well as detrending, for each of the plants under test. "X" markers in the plots indicate that the sample was with light turned off 38

4.7 Detail of measured stem frequency against the imposed temperature for both plants under test. 39

4.8 Scatter plot representing chamber relative humidity (%) against normalized stem frequency with equation 4.2 , as well as detrending, for each of the plants under test. "X" markers in the plots indicate that the sample was with light turned off 40

4.9 Detail of measured stem frequency against the imposed relatve humidity for both plants under test. Red points represent stem frequency samples that don't have corresponding climatic chamber measurements. 41

4.10 Stratified temperature and humidity analysis vs Stem frequency . . . 42

4.11 Detail of measured stem frequency against the vapour pressure deficit for both plants under test. 43

4.12 Detail of measured stem frequency against the imposed VPD for both plants under test. Red points represents stem frequency samples that don't have corresponding climatic chamber measurements. . . . 44

4.13 Granger causality matrix. Each environmental variable is used to predict stem frequency. 45

4.14 Detail of measured stem frequency against the imposed temperature for both plants under test. Plant 1 is subjected to water stress. 47

4.15 Detail of measured stem frequency against the imposed temperature for both plants. Overview of all the experimental periods. 49

4.16 Climatic chamber setup setup, few days before the beginning of the experiment 50

4.17 Data from 1st experimental period. Offset included. Yellow background indicates light on, white background indicates light off. Different color curves distinguish older and recent days. Dashed line indicates the temperature profile 52

4.18 Data from 1st experimental period. Offset removed. Yellow background indicates light on, white background indicates light off. Different color curves distinguish older and recent days. Dashed line indicates the temperature profile 54

4.19 Data from 2nd experimental period. Offset removed. Yellow background indicates light on, white background indicates light off. Different color curves distinguish older and recent days. Dashed line indicates the temperature profile 55

4.20 Data from 3rd experimental period. Offset removed. Yellow background indicates light on, white background indicates light off. Different color curves distinguish older and recent days. Dashed line indicates the temperature profile. 56

4.21 Data from 4th experimental period. Offset removed. Yellow background indicates light on, white background indicates light off. Different color curves distinguish older and recent days. Dashed line indicates the temperature profile. 57

4.22 Example of a climatic chamber labeled image during experiment. The plant in the center was put only for testing purposes, no stem frequency was acquired from it. 62

4.23 Overview of training metrics 63

4.24 Example of plant detection and bounding box extraction. 64

4.25 CIELAB color space representation. 65

4.26 RGB segmented plant (left) and corresponding image after color thresholding 66

4.27 Leaf area estimation (top), normalized stem frequency (middle), and raw stem frequency (bottom) over the experimental period. 68

4.28 Visual evolution of plant conditions during the experiment. 69

5.1 Experimental setup with the three plant groups 73

5.2 Example of needle insertion for stem frequency measurement. . . . 74

5.3 Boxplot of stem frequency baseline distribution for each experimental group 75

5.4 Evolution of raw daily stem frequency (top panel) and normalized daily stem frequency (bottom panel) measurements for the 3 experimental groups 77

5.5 Stem frequency evolution aligned to the onset of visible symptoms . 78

5.6 Results of the mixed-effects linear models. Top panel: base model. Middle panel: covariate-adjusted model (RH, Temperature). Bottom panel: mixed model aligned pre- and post-symptom onset. 81

5.7 Mean normalized innovation autocorrelation functions (ACF) against actual elapsed time in hours across candidate models. Left: Comparison including the naive IID baseline. Right: Zoomed detail comparing AR(2), AR(6), and AR(2) with a daily cycle. The dashed vertical line marks the 24-hour circadian lag. 85

5.8 Unique predictive contribution per lag, measured as percentage change in held-out RMSE upon lag removal conditional on other terms. 86

5.9 Residual diagnostics for the `AR(2)_daily_cycle` model. Left: Normalized innovations vs fitted frequency. Center: Normal Q-Q probability plot. Right: Normalized innovations over time. 87

5.10 Results of the clustering procedure with different time steps. 92

5.11 Silhouette score against number of clusters with different time steps 94

5.12 Clustering performance evaluated using external indices (ARI and NMI) across different temporal resolutions. 95

5.13 Clustering results within individual experimental blocks at 3-hour temporal resolution. 100

6.1 Trunk frequency raw values recorded from April 16th 2024, the installation day. During the healing period, a significant amount of signal noise from the trunk sensors can be observed. 105

6.2 Overview of trunk frequency measurements and corresponding environmental variables (air temperature, relative humidity, soil water potential, and day–night cycles), along with STL decomposition segmented by astronomical seasons. 106

List of Tables

4.1 Detailed experimental protocol used to investigate the effect of temperature and relative humidity on plant stem frequency. 32

4.2 Summary of experimental conditions across the five periods. 52

4.3 Summary of daily metrics for each plant across experimental periods (offset removed data). 60

4.4 Training hyperparameters used for the YOLO model. 63

5.1 Distribution of tomato plants across experimental blocks and treatment groups. 73

5.2 Summary of significant model results 83

5.3 Model selection metrics across residual serial correlation structures on the 20-minute uniform grid. 84

5.4 Fixed-effect slope estimates, standard error changes, and nominal p-values across correlation models. 86

6.1 Seasonality index by season and plant 107

Chapter 1

Introduction

The central theme of this doctoral dissertation is the assessment of plant health through a so called *direct approach*, i.e. monitoring a quantity that is extracted directly and in vivo from the plant. As it will be better explained later, the main focus will be on the so called *stem (or trunk) frequency*, a novel method to estimate plant electrical conductivity. The research focuses on the application and validation of this sensor's technology to monitor and interpret plant physiological responses under varying environmental conditions and biotic stress factors. The structure of this thesis reflects the experimental scenarios investigated throughout the candidate's research activity within the framework of *climate-smart agriculture*. In particular, three main experimental contexts are considered. The first is a highly controlled environment, designed to test sensor functionality and monitor plant growth under precisely regulated conditions, including light, temperature, humidity, and irrigation. The second scenario involves greenhouse cultivation, where tomato plants are monitored under less controlled conditions and subjected to both biotic and abiotic stress factors. Finally, an open-field context is considered, where perennial plants, specifically apple trees, are monitored over an extended period exceeding one year.

The thesis is organized as follows:

- *Chapter 2*: introduces the experimental context of the thesis and provides an overview of the state of the art;
- *Chapter 3*: describes the technologies employed for plant monitoring;

- *Chapter 4*: presents controlled-environment experiments on tomato plants conducted in a climate chamber;
- *Chapter 5*: analyzes greenhouse experiments focused on both biotic and abiotic stress conditions in tomato plants;
- *Chapter 6*: investigates open-field monitoring of perennial crops, with particular reference to apple trees.
- *Chapter 7*: concludes the dissertation

1.1 Motivation and Research Objectives

Agriculture plays an increasingly critical role in modern society since it is responsible for one of the most basic human needs, the nutrition, whether as direct food source or through the sustenance of animals. Although it is often not perceived, at the media level, as one of the most impactful sectors compared to industries or transportation, it has a substantial influence on both the global economy and environmental sustainability. In particular, agriculture is responsible for more than 10% of global greenhouse gas emissions, ranking just below the energy and transport sectors [5, 6]. Moreover, it represents the dominant consumer of freshwater resources, accounting for over 70% of global water withdrawals when considering the broader food production sector [7, 8].

This scenario is further complicated by the increasing intensity of climate change effects observed over the past decades, including wildfires, extreme weather events, rising temperatures, sea level rise, and desertification [9]. These phenomena are progressively impacting agricultural systems, making it more difficult to maintain stable and efficient production chains.

As a consequence, crop production is increasingly exposed to both abiotic stresses, such as high temperatures and water scarcity, and biotic stresses, including pathogens, fungi, and insects [10, 11]. These factors contribute to a higher risk of yield reduction and production instability.

At the same time, the global population continues to grow [12], leading to an increasing demand for food production. This creates a critical challenge: the need

to enhance agricultural productivity while simultaneously limiting environmental impact. Without appropriate technological and methodological innovations, this dynamic may result in a reinforcing feedback loop, where increased production leads to higher emissions and resource consumption, further exacerbating climate change and its negative effects on ecosystems and human societies.

In this context, it becomes imperative to develop new technologies for the agricultural sector in order to achieve more efficient and sustainable production. This transition is enabled by the remarkable technological advancements of recent decades, particularly in the digital domain, and is commonly framed within the paradigm of *climate-smart agriculture*. A wide range of emerging technologies contributes to this paradigm, including machine learning, computer vision, Internet of Things (IoT) systems, energy harvesting solutions, and the development of low-cost, low-power hardware platforms. These technologies represent the foundation of a rapidly expanding research field aimed at improving resource efficiency, productivity, and sustainability in agricultural systems. This doctoral thesis is positioned within this context and focuses specifically on the development and analysis of novel methods for direct plant monitoring. In contrast to traditional approaches based on environmental measurements, direct monitoring targets the plant itself, with the objective of identifying suboptimal growth conditions or stress factors at an early stage, thus enabling timely intervention. Despite its potential, direct plant monitoring is still not widely adopted. This is mainly due to the challenges associated with performing continuous in vivo measurements, as well as the relatively high costs of current sensing technologies. However, its potential impact is significant. As production scales increase, costs are expected to decrease, making these technologies more accessible. Furthermore, direct monitoring does not necessarily imply the instrumentation of every individual plant within a field. Instead, a sampling-based approach can be adopted, where a subset of plants is monitored to achieve a balance between system cost (i.e., number of deployed sensors), maintenance, and the accuracy of stress detection across the field.

The aim of this thesis is to investigate the potential of direct sensing techniques for assessing plant health, moving beyond the indirect observation of environmental variables or other external proxies. The work builds upon previous research conducted within the eLions research group, where the candidate has had the opportunity to contribute over the past years. In particular, the group has investigated the potential

of electrical impedance measurements applied to different portions of plants as a means of obtaining information related to their physiological status.

Preliminary studies conducted within the group highlighted potential relationships between the electrical properties of plant tissues and changes in plant physiological conditions, suggesting that electrical measurements may provide valuable information for monitoring and early identification of plant stress. Building upon these observations, the development of a low-cost electrical impedance sensing approach for plants led to the implementation of devices capable of monitoring a quantity referred to throughout this thesis as *stem frequency*, which is related to the electrical impedance of a portion of the plant as it will be explained better in later sections.

While the main advantage of this approach lies in its low cost and potential scalability, a fundamental question remains: whether, and to what extent, variations in stem frequency can be reliably associated with changes in plant health and physiological status. Addressing this question represents the central objective and primary novelty of this thesis: providing a systematic, multi-environment, multi-species, and long-term assessment and validation of stem frequency as a reliable indicator of plant stress and physiological status.

Such a validation is particularly challenging because plant responses are influenced by a complex interplay of biological and environmental factors. To overcome these challenges, this research relies on a comprehensive experimental validation strategy that spans both controlled conditions and realistic agricultural scenarios:

- **Greenhouse Validation Campaign:** A large-scale, greenhouse experimental campaign involving 73 individual tomato plants was conducted to evaluate stem frequency responses when plants are subjected to different stress conditions
- **Long-Term Field Deployment:** A multi agricultural season monitoring campaign was deployed in an operational apple orchard to test durability, and reliability of the sensing system under real field conditions and weather patterns.

While the core underlying concept of stem frequency measurement was previously established by the research group, the novel contributions of this doctoral work focus entirely on the validation, experimental methodology, and analytical

frameworks required to evaluate this technology. Specifically, the candidate's main contributions include:

- **Experimental Design and Setup Implementation** Conceptualized and executed experimental protocols, including the design and assembly of climate chamber testing environments.
- **Plant Care and Trial Management:** Managed the physiological care, stress induction protocols, and health monitoring of the biological specimens during climate chamber and greenhouse trials
- **Data Pipeline and Statistical Analysis**: Developed the complete data processing pipeline and conducting comparative statistical analyses to link stem frequency variations to plant status
- **Validation:** multi-species, multi-environment validation assessing the limits and diagnostic potential of stem frequency for early stress detection.

The central question of this thesis can be summarized as follows: "Can a simplified, low-cost sensing method based on electrical property, specifically the *stem frequency*, effectively evaluate plant health and physiological status?

Chapter 2

Monitoring crop health

This chapter focuses on the techniques that have been proposed and are currently used in the scientific literature to assess plant health. First, the main established and emerging approaches are introduced and compared. Then, the methodological and conceptual developments that led to the adoption of the technique central to this work are discussed. In particular, this chapter outlines the evolution toward the use of *stem frequency*, a novel parameter derived from the electrical impedance of the plant stem, which will be the primary focus of the following chapters.

2.1 Introduction

Historically, since the emergence of agriculture around 12 000 years ago, close attention has always been paid to plant health conditions, as proper growth inevitably had a direct impact on crop yield and, consequently, a significant impact on population subsistence. This process consolidated over millennia through the development of qualitative agricultural practices based primarily on observation rather than quantitative calculations, a limitation that was clearly imposed by the technological constraints of the past. Examples include practices such as crop rotation, the timing of irrigation, the amount of water supplied to specific crops, and the use of fertilizers.

Since the early 2000s, with the widespread development and diffusion of increasingly inexpensive and sophisticated electronic technologies, a broad process of digitalization has taken place across society, affecting virtually every sector, including agriculture. This evolution has led to a scenario in which agricultural systems can be

extensively instrumented with sensors, allowing for the collection of large volumes of data and effectively shifting the previously described paradigm. Management decisions that were once primarily based on experience, intuition, and established practices are now evolving towards a more quantitative and data-driven approach. The transition is evident in the availability of commercially distributed sensing platforms, often provided as integrated hardware software solutions for farmers, which combine field sensors with dedicated smartphone or web-based applications to monitor crop and environmental conditions. Examples include soil moisture sensors used to optimize irrigation scheduling, as well as fertilization and pesticide spraying systems equipped with imaging devices that enable targeted application. Such technologies allow inputs to be applied only where and when needed avoiding resources waste. In this context, a fundamental methodological shift is currently taking place. Traditional plant monitoring approaches have historically relied either on indirect environmental measurements or on visual inspection. These methods provide useful information, but offer only a partial view of the plant's actual physiological state. More advanced diagnostic techniques, such as molecular (Polymerase Chain Reaction[PCR] based) and serological Enzyme-Linked Immunosorbent Assay (ELISA) methods, represent accurate alternatives for evaluation of plant diseases. However, they are limited by delayed response times, often requiring laboratory processing and exhibiting reduced reliability during asymptomatic stages of plant stress. For these reasons, recent research has increasingly focused on the development of direct, in-vivo monitoring techniques capable of capturing plant responses in real time. This paradigm shift moves from observing environmental causes to directly measuring plant reactions, enabling earlier detection of stress conditions and more effective intervention strategies. While the potential benefits offered by digital technologies in agriculture are substantial, the need to accelerate the digital transformation of the sector is increasingly evident. This urgency is driven both by the continuously growing global population as well as by the growing challenges imposed by climate change. The challenges associated with the digital transformation of agriculture are numerous and arise, first of all, from a technological perspective. Agricultural environments worldwide are highly diverse, making it difficult to develop low-cost and efficient technologies capable of adapting to the wide range of operational conditions. In this context, collaboration plays a crucial role, as the aggregation of data collected across different environments and scenarios represents a key enabling factor for many advanced technologies, one example is Artificial Intelligence (AI).

A second major challenge is represented by infrastructure. To fully benefit from digital technologies, reliable high-speed network connectivity is essential. Significant efforts have been made in recent years to reduce the internet connectivity gap between urban and rural areas, the latter being those most heavily involved in agricultural activities. However, even where network coverage is available, high-speed internet access is not always feasible for field sensors. This limitation is particularly relevant for battery-powered monitoring devices, for which high data transmission rates can lead to increased energy consumption. In large-scale agricultural fields, where maintenance operations and battery replacement require substantial time and labor, this issue can become a constraint. As a result, there has been a growing adoption of wireless communication protocols that prioritize wide-area coverage at the expense of reduced data rates. Such trade-offs can be acceptable in specific scenarios, for example in the case of field-deployed weather stations, where acquiring a measurement once per hour does not require high communication bandwidth (it is possible to send a sensor's reading on a minute-scale instead of millisecond-scale). In this sense, the *LoRa* communication protocol [13, 14], which will be briefly discussed later, and more in general the concept of LPWAN (*Low-Power Wide-Area*) can be of significant importance.

A further critical aspect concerns the high initial investment required for the adoption of advanced agricultural technologies. In many cases, these costs are not sustainable for small and medium-sized farms. As a consequence, such technologies tend to be accessible primarily to large-scale agricultural enterprises. This imbalance may lead to unintended systemic effects, including increased agricultural homogenization and a potential reduction in biodiversity.

Plant monitoring techniques can therefore be broadly categorized based on the target of observation. Indirect approaches focus on environmental variables such as temperature, humidity, and soil conditions, while direct approaches aim to measure the physiological state of the plant itself. This distinction is fundamental and will guide the structure of the following sections, where both indirect and direct monitoring methods are presented and analyzed.

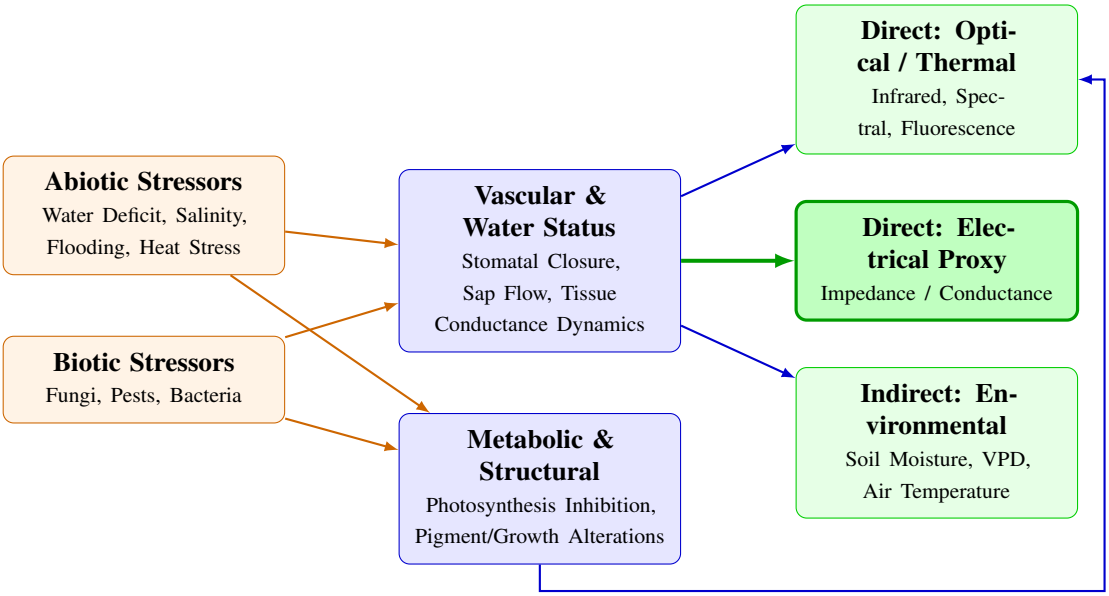


Fig. 2.1 Schematic representation of plant health monitoring: primary abiotic and biotic stressors converge into overlapping physiological responses, which are in turn detected by specific direct or indirect sensing techniques.

2.2 Crop monitoring

Plant health assessment is inherently complex. Similarly to the human body, although in a somewhat simplified manner, plants are complex living organisms characterized by articulated interactions with their surrounding environment. Plant health assessment is complex because multiple primary stressors converge into overlapping physiological responses. As an example, stomatal closure, which can be interpreted as a response to adverse conditions, is also a normal physiological mechanism regulating plant hydration and photosynthesis [15, 16]. However, this same response can be observed under a broad range of primary stresses, including water deficit [], excessively high soil salinity, and root flooding. Different sensors are capable of identifying, with varying degrees of accuracy, the presence of specific physiological responses of a plant to a given condition. These responses can then be associated, following careful analysis, with the possible presence of a primary stress. This concept is schematically represented in Figure 2.1.

For this reason, combining multiple sensors is beneficial in order to achieve a more comprehensive diagnosis. However, it is not always feasible to have access to all available sensing technologies, both due to cost considerations and because certain

sensors may be more suitable in specific contexts while being less effective in others, restricted by power constrains or applicable to some plant species but not to others, not feasible for large field monitoring (e.g. laboratory methods which are very accurate but less scalable). As schematically illustrated in Figure 2.1, numerous technologies have been reported in the literature for monitoring crops at different levels. The first distinction (which the author of this dissertation considers to be the most important) is between *indirect methods*, which monitor the surrounding environment, and *direct (plant-focused) methods*, which target physiological parameters of the plant itself.

2.3 Indirect Methods for plant health

This first category of methods represents the most traditional approaches and can constitute a valuable asset for the overall assessment of plant health. Indirect methods refer to all those techniques that monitor the environmental conditions in which a plant is embedded, such as air temperature, relative humidity, and light intensity. The scientific literature provides extensive indications regarding the optimal climatic conditions under which a crop can thrive. By using weather stations capable of collecting climatic data, together with soil matric potential sensors, it becomes possible to determine whether intervention by the farmer is required. A relevant example developed at Politecnico di Torino is the WAPPFRUIT project, for which further details can be found in [17–19], as well as in the doctoral dissertation of Mattia Barezzi [20]. These works demonstrate that excellent results, in terms of both crop productivity and water savings in commercial settings, can be achieved by combining temperature and humidity sensors with soil matric potential measurements. In particular, nearly identical productivity in apple orchards was obtained using a threshold-based irrigation strategy driven by soil matric potential, while achieving approximately 50% water savings [17].

Other approaches for stress evaluation, particularly for water stress prevention, are based on water balance methods (see Figure 2.2). These techniques estimate crop water requirements indirectly by monitoring environmental variables and modeling the plant–atmosphere interaction.

Water balance methods aim to estimate the water needs of a crop by monitoring its surrounding conditions, such as temperature, air humidity, and light intensity, and

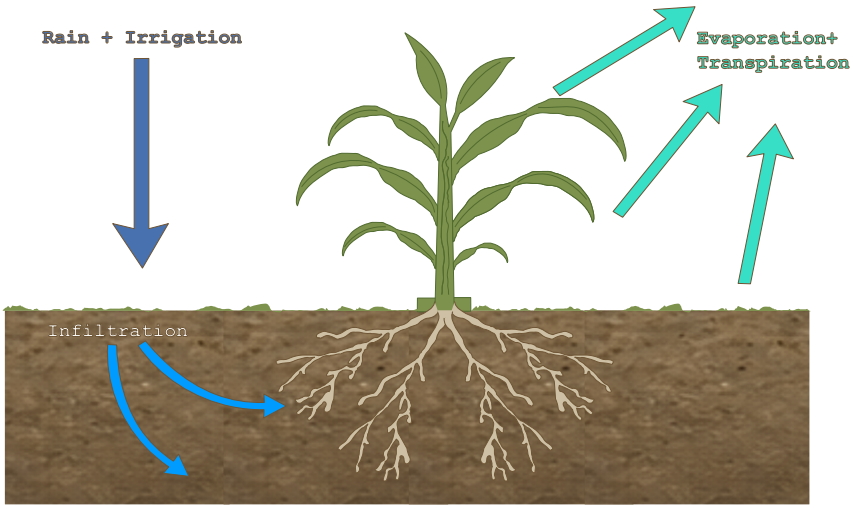


Fig. 2.2 Water balance example

by evaluating the daily water deficit. Based on these measurements, irrigation can be scheduled accordingly.

More specifically, environmental sensor readings are used to estimate the crop evapotranspiration (ET_c), which represents the total amount of water transferred from the soil–plant system to the atmosphere through evaporation and transpiration processes. This quantity is typically derived from the reference evapotranspiration (ET_0), which characterizes the evaporative demand of the atmosphere independently of crop type, crop development, and management practices.

According to the standard FAO-56 methodology [21], ET_0 is defined as the evapotranspiration rate from a hypothetical green grass reference crop with an assumed height of 0.12 m, a fixed surface resistance of $70\,\mathrm{s\,m^{-1}}$, and an albedo of 0.23. It is computed using the FAO Penman–Monteith equation:

$$ET_0 = \frac{0.408\Delta(R_n - G) + \gamma \frac{900}{T+273} u_2 (e_s - e_a)}{\Delta + \gamma(1 + 0.34u_2)} \tag{2.1}$$

where the individual terms are defined as follows:

- ET_0 is the reference evapotranspiration [$\mathrm{mm\,d^{-1}}$]
- R_n is the net radiation at the crop surface [$\mathrm{MJ\,m^{-2}\,d^{-1}}$]
- G is the soil heat flux density [$\mathrm{MJ\,m^{-2}\,d^{-1}}$]

- T is the mean daily air temperature at 2 m height [°C]
- u_2 is the wind speed measured at 2 m height [$\mathrm{m\,s^{-1}}$]
- e_s is the saturation vapour pressure [kPa]
- e_a is the actual vapour pressure [kPa], making $(e_s - e_a)$ the vapour pressure deficit (VPD) of the air
- Δ is the slope of the vapour pressure curve [$\mathrm{kPa\,°C^{-1}}$]
- γ is the psychrometric constant [$\mathrm{kPa\,°C^{-1}}$]
- 0.408 is the conversion coefficient from energy flux density to equivalent water depth [$\mathrm{m^2\,mm\,MJ^{-1}}$]

The Penman–Monteith formulation combines an energy balance term (driven by net radiation R_n and soil heat flux G) with an aerodynamic term (driven by wind speed u_2 and vapour pressure deficit $e_s - e_a$). Once ET_0 is calculated, the actual crop evapotranspiration ET_c is obtained by applying crop-specific coefficients (K_c) that account for the specific physiological characteristics, growth stage, and canopy architecture of the plant ($ET_c = K_c \cdot ET_0$). Based on ET_c, several irrigation scheduling approaches can be employed [22].

2.4 Direct Methods

Direct methods differ from indirect approaches in that they do not rely on monitoring the surrounding environmental conditions to infer plant health. Instead, they aim to extract parameters that are more closely related to the internal physiological state of the plant, thus providing a more direct representation of the processes occurring within it. This category includes all sensing techniques capable of measuring biological or physical parameters directly from the plant. In this section, the focus is placed on in vivo monitoring approaches, rather than laboratory-based methods, which often require the extraction of plant samples and may be partially or fully destructive.

2.4.1 Plant Imaging

One of the most rapidly developing approaches for plant health assessment is based on imaging and computer vision techniques, particularly with the recent advancements in machine learning. Imaging is considered here as a direct method because it captures the plant's response to incident radiation, which varies depending on its physiological condition. A well-known example is the progressive yellowing of leaves under water stress conditions. The green coloration of leaves is primarily due to chlorophyll, a key component of photosynthesis. When water availability is limited, photosynthetic activity is reduced, leading to a degradation of chlorophyll. As a result, the underlying pigments, such as carotenoids, become more visible, causing the leaf to appear yellow. Another observable effect is the loss of turgor. Plant tissues maintain their rigidity primarily due to water pressure within the xylem. In conditions of water deficit, this pressure decreases, leading to a visible wilting of the plant structure. Among imaging-based indicators, the Normalized Difference Vegetation Index (NDVI) is one of the most widely used. It is defined as:

$$NDVI = \frac{NIR - VIS}{NIR + VIS} \tag{2.2}$$

where NIR and VIS represent the reflectance in the near-infrared and visible spectral regions, respectively [23]. This index provides a quantitative measure of vegetation health and is highly sensitive to changes in chlorophyll content and plant vigor. Furthermore, these types of responses can be captured with high accuracy using machine learning and deep learning techniques applied to image data [24]. Imaging techniques, in general, offer significant potential due to their scalability. They can be applied across different spatial scales, ranging from individual plants to entire agricultural fields. For instance, cameras mounted on unmanned aerial vehicles (UAVs) enable automated monitoring of large cultivated areas. However, several challenges remain. High-quality imaging systems can be costly, and the reliability of the measurements is strongly influenced by environmental variability, such as changing atmospheric conditions, illumination, and viewing geometry. These factors can introduce significant noise and variability in the acquired data, complicating the effectiveness of such techniques.

2.4.2 Sap Flow Measurements

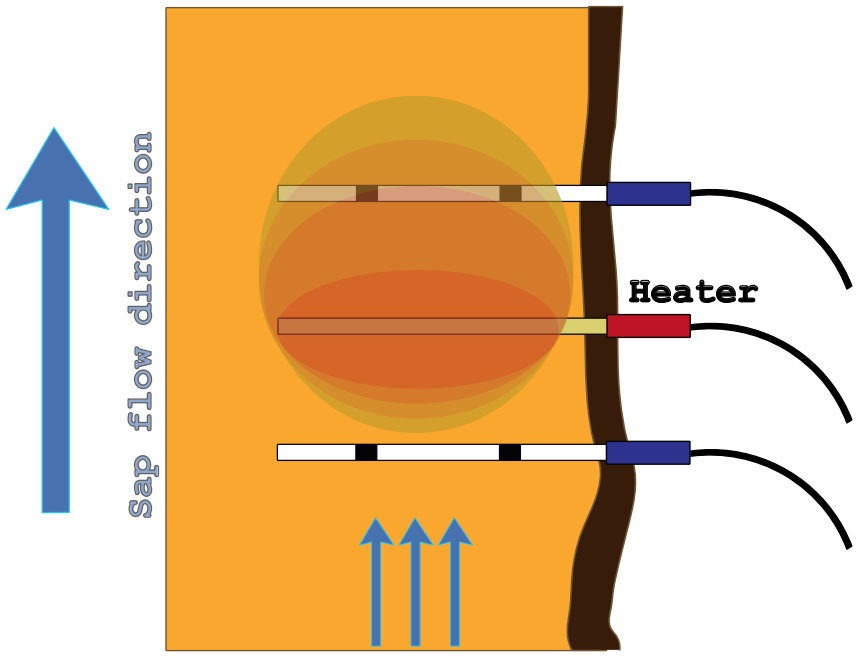
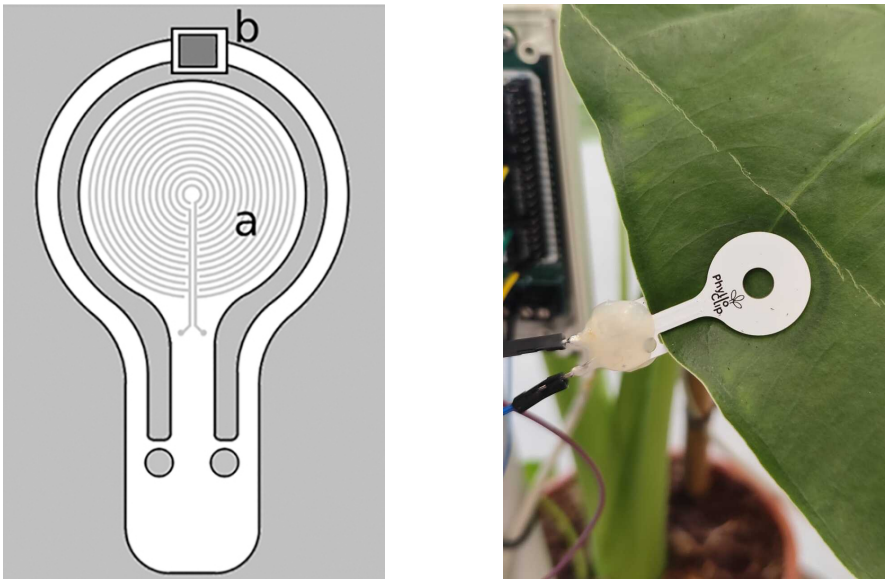


Fig. 2.3 Sap flow measurement principle. Courtesy of [1]

Sap flow measurement represents another direct monitoring approach, aimed at quantifying the velocity of sap flow within the plant vascular system. A typical sap flow sensor consists of three elements: two temperature probes (thermocouples usually) and a heater positioned between them. This configuration allows the measurement of the temperature difference between the two probes, which depends on the direction and velocity of the sap flow (see Figure 2.3). During operation, the heater generates a heat pulse that propagates through the plant tissue. At the same time, the sap flow contributes to advecting the thermal signal along the stem. As a result, one of the temperature probes will register a higher temperature depending on the direction of the flow. By analyzing the time required for the heat pulse to travel between the probes, it is possible to estimate the sap flow velocity. This information is strongly related to the plant transpiration rate and can therefore be used to assess the plant water balance. Additionally, sap flow is closely linked to stomatal activity and, more generally, to the circadian rhythms of the plant. An example of a commercial sap flow sensor is reported in [25]. Despite its relevance, this method presents several limitations. In particular, the cost of the instrumentation can be significant, and its application may be challenging for plants with non-woody stems or small diameters,

such as tomato plants. In such cases, the insertion of relatively large probes may cause mechanical damage to plant tissues, limiting the applicability of the technique. Moreover the energy required to power such devices high and a bulky power sources (battery or solar panel) may be needed for continuous monitoring.

2.4.3 Fylloclip



(a) Courtesy of [26] (b) FylloClip operating on a leaf

Fig. 2.4 FylloClip sensor

Another important parameter, particularly for assessing the plant water status and the potential onset of fungal diseases caused by excessive leaf wetness, is leaf wetness. A notable sensor for measuring this parameter is the FylloClip device, whose operating principle is described in [26]. An example of the sensor mounted on a leaf is shown in Figure 2.4. The device is attached directly to the leaf using a clip-based mechanism. It operates as a capacitive sensor, capable of detecting the presence of water or water vapor on the leaf surface. This is achieved through variations in its dielectric properties, which result in measurable changes in capacitance.

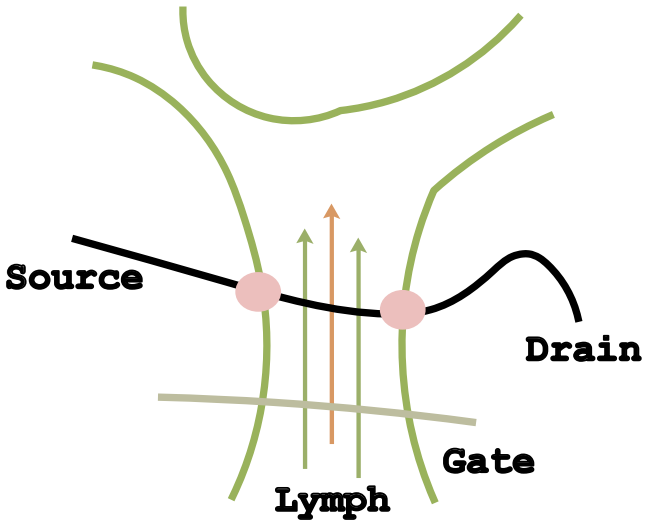


Fig. 2.5 Image from [2]

2.4.4 Organic Electrochemical Transistors (OECT)

Another interesting measurement approach, conceptually very close to the focus of this thesis, is the organic electrochemical transistor (OECT) [2]. This technology has shown strong potential for continuous in vivo plant monitoring, particularly for the assessment of ion concentration and water stress [27], as well as for the detection of sugars such as sucrose and glucose within the stem xylem [28]. The working principle is schematically illustrated in Figure 2.5. The device consists of a textile-based fiber functionalized with a conductive polymer, which is directly integrated into the plant stem. A thin silver wire is placed in close proximity and acts as the gate electrode. In general, the device operates in a manner analogous to a transistor immersed in an ionic conductive medium. When the gate voltage V_g is increased, the drain-source current I_{ds} decreases due to the dedoping of the conductive polymer. This technology has shown promising results for continuous in vivo plant monitoring and for the rapid detection of water stress conditions [2]. A possible limitation, compared to the stem frequency approach described later in this work, is the need for an analog-to-digital conversion stage within the measurement setup. It remains an open question whether this increased system complexity is justified by a favorable trade-off in terms of cost and performance, especially when compared to simpler but potentially less accurate methods. This comparison between measurement approaches is still an active research question.

2.4.5 Impedance Monitoring and stem/trunk frequency

The final method in this brief overview (which is intended to be introductory and is by no means exhaustive of all existing approaches) for assessing plant condition is the measurement of electrical impedance in plants. This method gained popularity in the last years and several studies have demonstrated promising results [29–34]. For this reason, the eLions research group at Politecnico di Torino has undertaken this research direction to enable efficient plant monitoring in the context of *climate-smart agriculture*. The work has primarily focused on the early detection of abiotic stress, particularly water stress, aiming to optimize water usage, as well as on the identification of biotic stress associated with fungal diseases, which can significantly reduce crop yield. In [33], *Garlando et al.* presented the first experimental results of the research group concerning the effectiveness of impedance measurements for the detection of water stress. In particular, an *Agilent 4294A* impedance analyzer was employed for continuous impedance monitoring on tobacco plants subjected to different irrigation cycles. The study highlighted a strong correlation between Soil Water Potential measurements [33, 32] and impedance measurements (modulus and phase) acquired at different excitation frequencies. Moreover, [35] showed that stem impedance is affected not only by abiotic water stress but also by environmental factors such as air humidity and temperature, suggesting its potential use as a proxy for plant health status. Different experiments conducted using bench impedance analyzer by Stefano Calvo of eLions research group can be found here in his doctoral thesis dissertation [29].

Although the studies presented in [33, 35] reported promising results, they were preliminary and relied on benchtop instrumentation. This introduced two main limitations that the research group aimed to address:

1. In vivo impedance measurements performed using benchtop instruments are not scalable for real-world applications. Due to their size and operational constraints, such instruments are unsuitable for repeated or continuous field measurement campaigns.

2. Moreover, the average size of agricultural holdings in Europe is approximately 16 hectares [36], decreasing to about 11 hectares in Italy [37]. This structural fragmentation implies that farms would greatly benefit from reductions in operational costs and resource consumption (e.g., water and energy). How-

ever, the adoption of advanced technologies commonly associated with smart agriculture, including impedance measurements, is often limited by the reduced capacity of these farms to amortize high capital and operational costs. While lower-cost alternatives to benchtop impedance analyzers exist, they still represent a significant investment. For this reason, the research group decided to focus on the measurement of a quantity proportional to impedance, specifically its magnitude, enabling an indirect estimation of impedance while substantially reducing system cost.

For these reasons, the eLions research group at Politecnico di Torino has focused its efforts on the development of a simplified and indirect method for electrical impedance measurement, leading to the introduction of the so-called *stem frequency* (or trunk frequency) technique. This approach enables the measurement of an oscillation frequency generated by an electronic circuit in which a portion of the plant is directly involved. As a result, the electrical properties of the plant influence the oscillation behavior of the system, allowing impedance-related information to be indirectly captured through frequency measurements.

In this doctoral thesis, this parameter is extensively investigated, and a series of experimental studies are conducted to evaluate its potential as an indicator supporting the assessment of plant health status.

Chapter 3

Materials and Methods

3.1 Experimental Environments

Throughout this research activity, multiple experimental campaigns were conducted to evaluate the effectiveness of stem electrical conductivity measurements for assessing plant health status. In particular, a progressive approach was adopted to approximate real deployment conditions. The experimental work initially focused on highly controlled environments, namely climate chambers, allowing precise regulation of environmental variables. Subsequently, experiments were carried out in greenhouse conditions, characterized by a lower level of control and increased variability. Finally, the methodology was tested in open-field scenarios.

3.1.1 Climate Chamber

The experiments in controlled environment were conducted at the Mondovì (CN) campus of the Politecnico di Torino. For this initial experimental phase, it was decided to work in an easily controllable environment before transitioning to plant monitoring in more complex settings, such as greenhouses or open fields. The study utilized climate chambers manufactured by Aralab [38] which allowed full control over the environmental growth parameters of the test plants. These climate chambers can be configured with various sensor combinations. For the experiments described in this dissertation, the following parameters were monitored:

- **Air Temperature** (°C)
- **Air Relative Humidity** (%)
- **Light Intensity** ($\mu mol\, m^{-2}\, s^{-1}$)

Further technical details about the onboard sensors can be found in the product datasheet [38] but a snapshot for convenience of the reader is reported in figure 3.1.

TECHNICAL SPECIFICATIONS

TECHNICAL DATA FOR STABILCLIMA 600 & 1200 STABILITY CHAMBERS

TEMPERATURE RANGE [1]	-5°C to 60°C
EXTENDEND TEMPERATURE RANGE (OPTIONAL)	-20°C to 60°C (only for StabilClima 1.200 model)
TEMPERATURE FLUCTUATION IN TIME	±0.1°C to ±0.2°C
TEMPERATURE UNIFORMITY IN SPACE	± 0,15°C to ± 1,0°C
At 25°C / 60%rH	± 0,24°C
At 30°C / 65%rH	± 0,24°C
At 40°C / 75%rH	± 0,35°C
HUMIDITY RANGE	20% to 95% rH
HUMIDITY FLUCTUATION IN TIME	± 1%rH
HUMIDITY UNIFORMITY IN SPACE	± 2%rH
At 25°C / 60%rH	± 0,83%rH
At 30°C / 65%rH	± 0,69%rH
At 40°C / 75%rH	± 1,20%rH
SHELVES (STANDARD CONFIGURATION) [2]	StabilClima 600: 4 stainless steel wire shelves StabilClima 1 200: 8 stainless steel wire shelves
STANDARD WIRE SHELF SIZE	645mm x 515mm
STORAGE [2]	0.33 m² and 18 Kg weight load (per shelf)
STORAGE (STANDARD CONFIGURATION) [2]	StabilClima 600: 1,33 m² StabilClima 1 200: 2,67 m²
AIRFLOW	0.2 m/s uniform across the shelves
INTERNAL VOLUMES	StabilClima 600: 543 liters StabilClima 1 200: 1.194 liters

Fig. 3.1 Main characteristics of employed climatic chambers

Regarding light intensity measurement, a manual characterization was performed using a spectroradiometer, as the chamber setup did not include a radiance sensor. Consequently, it was necessary to post-process the light setpoints (provided as percentages) and convert them into Photosynthetic Photon Flux Density (PPFD for short) values through direct measurements.

Climatic chamber light characterization

The climate chamber allowed the light intensity to be adjusted on a relative scale from 0 to 100%. However, to ensure a more rigorous and quantitative analysis, a manual characterization was performed. Experimentally, the light intensity was varied from 0 to 100%, and the corresponding PPFD was measured using a quantum sensor.

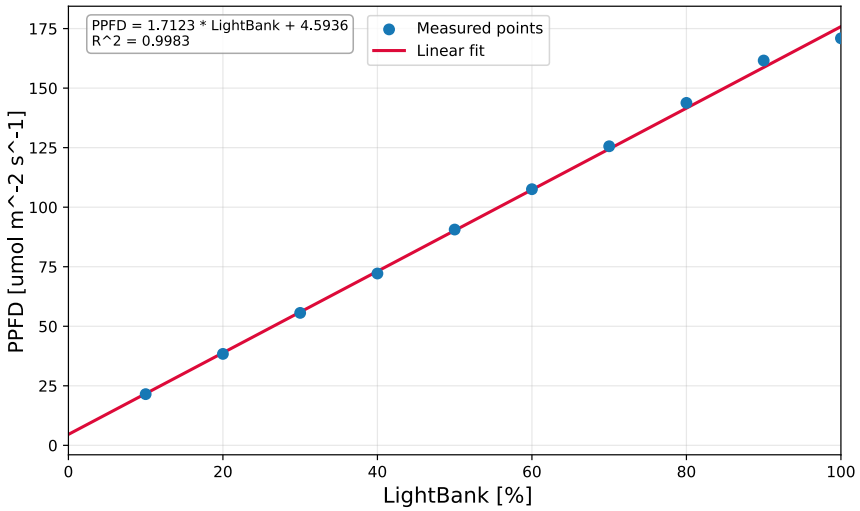


Fig. 3.2 Manual characterization of climate chamber light intensity

PPFD quantifies the number of photons within the 400–700 nm range that are available for photosynthesis, thus representing the actual amount of usable light reaching the plant. In contrast, the percentage scale provided by the climate chamber does not represent a physical measurement and does not account for factors such as the distance between the light source and the plant canopy. Therefore, PPFD measurements enable a more reliable quantitative analysis.

The results of this characterization are reported in Fig. 3.2. A strong linear relationship between the chamber light setting and PPFD can be observed. For simplicity, the relative light percentage will be used as the reference unit in the following analyses, while keeping this calibration in mind. The corresponding PPFD values can be estimated using the experimental relationship:

$$PPFD = 1.7123 \cdot Lightbank + 4.5936 \tag{3.1}$$

It should be noted that direct PPFD measurements during data acquisition would be preferable. However, since this was not possible within the current experimental setup, this calibration procedure was adopted.

3.1.2 Greenhouse

In the following chapters, several experiments conducted in a greenhouse will be described. This facility, located in Grugliasco (Turin), was kindly made available by colleagues from the University of Turin, in particular by the Department of Agricultural, Forest and Food Sciences (DISAFA). The facility is made of a steel structure with tempered glass panels, which do not include specific optical filters or polymer coatings. The greenhouse is equipped with a passive ventilation system consisting of:

- Side walls with vertically sliding openings
- A roof opening at the ridge to allow natural air exchange

Both ventilation mechanisms are controlled by an automated control unit that monitors temperature and actuates openings to maintain target environmental conditions. Heating is provided by gas powered heat pumps, which are automatically activated when the temperature drops below a predefined threshold.

During summer months, temperature control is additionally supported by a shading system consisting of a mesh screen placed over the roof, partially reducing incoming solar radiation, including ultraviolet components.

3.1.3 Open Field

The last chapter of this dissertation is dedicated to open-field measurements in apple orchards. In particular, the selected location is the same used in a previous monitoring experiment conducted by Mattia Barezzi within the framework of the WAPPFRUIT project funded by the Piedmont Region [17].

In that study, several monitoring units were deployed to measure soil water potential at different depths and manage an automatic irrigation scheduling strategy. The

WAPPFRUIT project has been further extended in this dissertation by integrating additional analyses based on a novel sensing technology developed by the eLions research group, aimed at directly and *in vivo* monitoring the electrical conductivity of the plant stem. Specifically, the experimental site consists of two commercial apple orchards located in Lagnasco (CN), Italy, referred to in the original study as Farmer 2 (F2). Within this site, two rows were selected: an experimental row (EX), where the irrigation strategy proposed in [17] was applied, and a conventional row (CV), where irrigation was managed according to standard farming practices.

Each row includes three measurement locations, namely CV1, CV2, and CV3 for the conventional row, and EX1, EX2, and EX3 for the experimental row. At two of these locations (CV2 and EX2), two *trunk (or stem) frequency* sensors were installed. This variable represents the electrical conductivity of a section of the plant and will be discussed in detail in the following sections. These two measurement points are used in the final chapter for the analysis of a monitoring campaign lasting more than one year, focusing on two apple trees.

3.2 Sensor System and Data Acquisition

The main focus of this dissertation is the direct monitoring of plants for the assessment of their health status, with particular emphasis on electrical conductivity measurements of the stem/trunk. In recent years, this approach has emerged as a promising technique within the field of smart agriculture. In addition to the direct monitoring performed through electrical impedance measurements of the stem, a range of complementary sensors was employed. These included both direct and indirect measurement techniques, used for validation purposes as well as for comparative analysis. With specific regard to impedance measurements, the inherent complexity and impracticality of using laboratory grade instrumentation in field conditions led to the adoption of a simplified approach, namely the so-called *stem (or trunk) frequency*. This method represents a low-cost and more easily deployable solution for estimating the electrical conductivity of a portion of the plant, albeit with expected trade-offs in terms of measurement accuracy.

Among them, particular importance is given to stem (or trunk) frequency measurements, which provide an accessible alternative to more complex and bulky instrumentation.

3.2.1 Stem Frequency: a simplified impedance reading method

This parameter constitutes the primary focus of this doctoral dissertation, which examines its behavior across various plant species and conditions. The concept of a simplified indirect impedance evaluation was introduced in [39], where the authors designed a simple relaxation oscillator based on a *555* timer [40] from Texas Instruments.

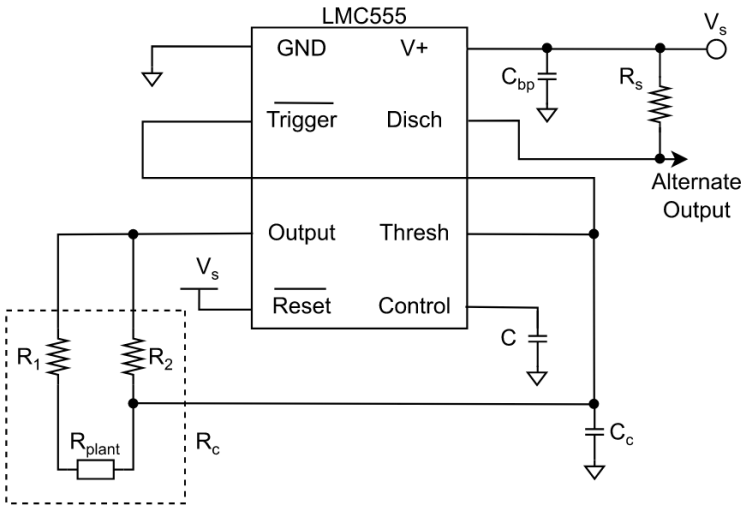


Fig. 3.3 Courtesy of [3]. Schematic of a *LMC555* based 50% oscillator with plant in the loop.

The circuit is extremely simple, and its schematic is shown in Figure 3.3. The *LMC555* is operated in the *50% duty cycle* configuration described in the datasheet [40], with a key modification: the feedback loop that determines the oscillation frequency includes the portion of the plant whose impedance is being measured. Two resistors, R_1 and R_2, respectively connected in series and in parallel with the plant segment under investigation, define the minimum and maximum oscillation frequencies of the circuit. The output of the circuit ("Alternate output" in Figure 3.3) is a square wave whose frequency depends on the overall impedance of the plant portion under measurement. Frequency acquisition is straightforward and can be readily performed using the input capture functionality available on every commercial microcontroller. A simplified conceptual representation of this measurement principle is shown in Figure 3.4. Using this system, it is therefore possible to acquire a new measurable quantity, hereafter referred to as *stem frequency*, by means of a microcontroller only. The value of this frequency can be approximated using the

expression reported in the 555 timer datasheet:

$$f = \frac{1}{1.4 \cdot R_c \cdot C_c} \tag{3.2}$$

The equivalent resistance R_c directly depends on the impedance of the stem portion under measurement, while the resistors R_1 and R_2 define the minimum and maximum achievable frequencies during the design phase.

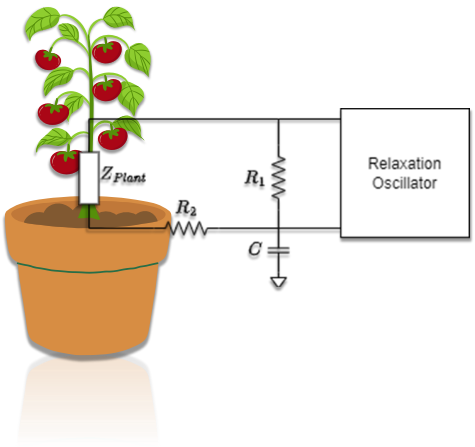


Fig. 3.4 Experimental setup for relaxation oscillator applied to plant's stem

3.2.2 Soil Water Potential measurement

Although one of the main objectives of this research is to develop plant health assessment methods based exclusively on a plant-derived signal (stem frequency), it remains necessary, especially in the early stages, to benchmark these approaches against established state-of-the-art sensing technologies. To this end, the Watermark Soil Moisture Sensor [4] was selected for measuring soil water potential. This sensor, manufactured by Irrometer Company, is a resistive device designed to estimate soil water potential. For reasons of cost and simplicity, a custom readout system based on a 555 oscillator was implemented. This approach enables indirect measurement

of the sensor response, avoiding the use of proprietary acquisition systems provided by the manufacturer. In addition, it ensures seamless integration with the custom sensing platform developed within the research group [29, 17, 39, 41, 34, 20]. A simplified schematic of the readout circuit is shown in Figure 3.5, while further details can be found in the doctoral dissertation by Stefano Calvo [29].

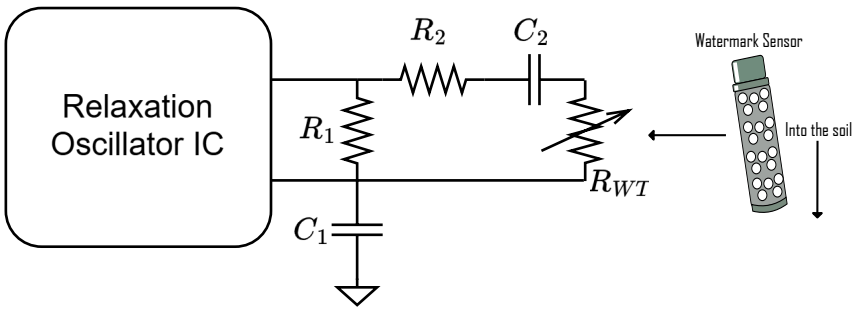


Fig. 3.5 Readout circuit for the Watermark sensor [4]

Briefly, the resistance of the Watermark sensor varies as a function of soil moisture. This variation affects the frequency of the square wave generated by the oscillator circuit, which therefore becomes dependent on soil water content. The oscillation frequency is measured by a microcontroller and subsequently converted into soil water potential. As previously mentioned in Section 3.1.3, in the final chapter the *stem/trunk frequency* sensing approach will be integrated with the system described in [18, 17]. Within that study, TEROS21 sensors [42] were employed. Therefore, the same sensors will be used just in the last chapter analyses for monitoring soil water potential instead of the just proposed technique.

3.2.3 Camera System

Besides environmental monitoring it was also essential to obtain an automated and as objective as possible visual feedback of the monitored plants. One relevant parameter for assessing plant health is the evaluation of leaf area, and more specifically the effective green leaf area. Moreover, performing this assessment manually would have been impractical for continuous monitoring. For this reason, some of the experiments presented in this chapter were equipped with simple cameras installed inside the climate chambers, enabling a fully automated visual evaluation of the plants. The experimental setup is illustrated in Figure 3.6. The camera is positioned above the

plant, with an optical axis perpendicular to the canopy. This configuration allows simultaneous observation of multiple plants from a top-down perspective, facilitating the estimation of leaf area.

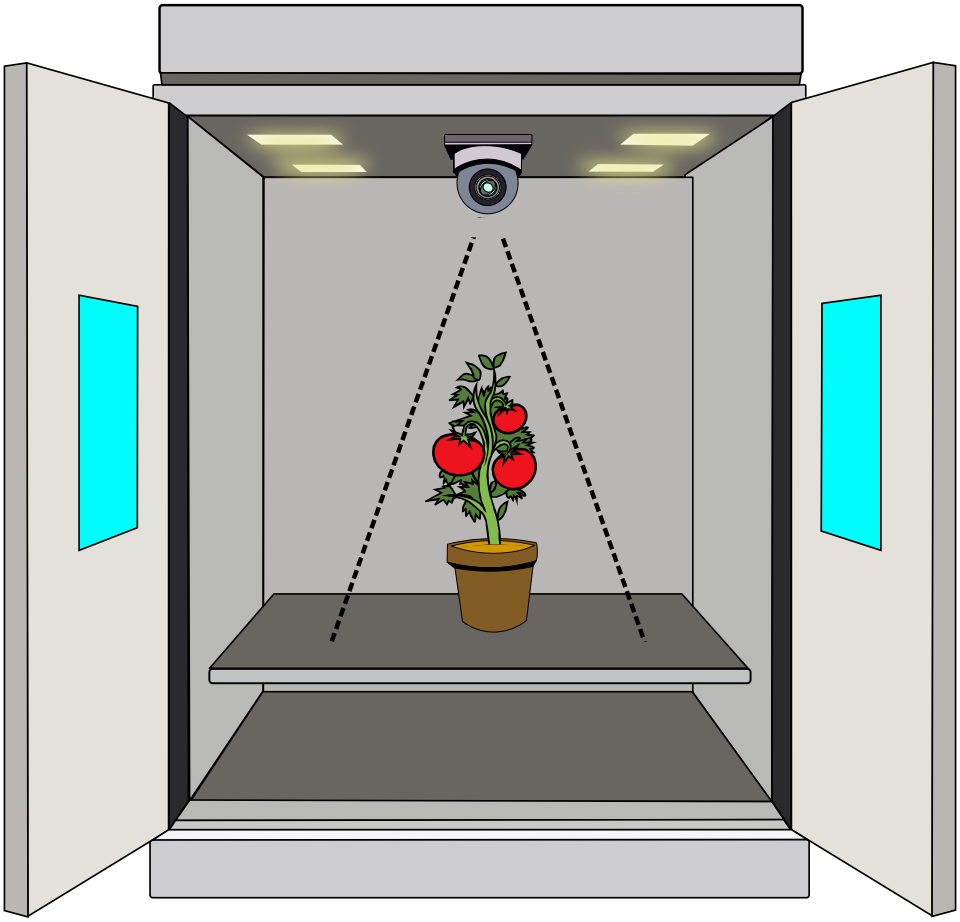


Fig. 3.6 Camera-based monitoring setup inside the climate chamber. Up to 4 plants can be monitored simultaneously.

The adopted device is a low-cost commercial surveillance camera. Image acquisition was performed at regular intervals of 3 hours. The image processing pipeline employed will be discussed in later sections.

In summary, the experimental setups and analyses presented in this dissertation can be described in terms of environments and measured variables as follows. It should be noted that not all measurements are available in every experiment.

- **Climatic Chamber (Tomato)**
  - Stem/trunk frequency

  - Air temperature
  - Air relative humidity
  - Ambient light
  - Soil water potential (Watermark sensor)

- **Greenhouse (Tomato)**
  - Stem/trunk frequency
  - Air temperature
  - Air relative humidity
  - Soil water potential (Watermark sensor)
  - Images

- **Open Field (Apple Trees)**
  - Stem/trunk frequency
  - Air temperature
  - Air relative humidity
  - Soil water potential (TEROS21 sensors)

Chapter 4

Climatic Chamber Experiments

4.1 Introduction

In this section, several climate chamber experiments conducted on tomato and tobacco plants are presented. The aim of these experiments was to investigate how environmental conditions influence stem frequency measurements. Since the relationships between these environmental parameters and plant physiology are well documented in the literature, this approach provides a useful starting point for evaluating whether or not stem frequency can be a useful proxy for plant health.

I was responsible for the design of the different experiments, the data analysis, and the general monitoring on site of the plants throughout the experimental period.

Although different proof-of-concept experiments and shorter experimental trials were conducted by our research group over the years, this section focuses on the most extended experiments and on a wider range of simulated environmental scenarios. Nevertheless, the results presented in this chapter should be regarded as preliminary and as deserving further investigation in future work. Despite the different environmental conditions tested and the considerable amount of data collected, the biological sample remains limited, particularly since only two tomato plants were monitored. Therefore, the results do not provide a sufficiently large biological sample to support definitive conclusions regarding the observed relationships.

The inclusion of this section in the dissertation is motivated by its role in establishing what can be measured using the proposed stem frequency sensor and what type of

response can be expected under controlled environmental conditions. In this sense, the experiments provided an important basis for the subsequent development of the sensing approach and for the interpretation of measurements obtained in less controlled environments. Accordingly, the observations and conclusions presented in this chapter should be considered primarily as hypothesis-generating rather than as definitive evidence of the underlying physiological mechanisms.

As mentioned above, additional experiments involving shorter and less continuous measurement periods were also conducted during the development and testing of the system. Some of these experiments were affected by sensor or system malfunctions, which are a natural part of the initial testing and development phase. Furthermore, these trials were originally conceived primarily as system-testing experiments rather than as measurement campaigns designed to provide statistically significant biological evidence. For these reasons, and given the limited continuity and reliability of some of the resulting datasets, these additional measurement campaigns have not been included in the dissertation.

This chapter presents the first, more conceptually structured experiments that laid the foundation for subsequent trials in less controlled environments, which will be presented later in Chapters 5 and 6, respectively.

4.2 Response to Environmental Variables of Tomato Plants

Building upon the experimental setup described in the previous section, the climate chamber trials were conducted on 2 tomato plants (*Solanum lycopersicum*). Tomato was selected due to its widespread use in both research and agriculture (estimated more than 180 millions of tons production worldwide), as well as the extensive literature available on its physiological responses to environmental conditions [43]. This makes it a suitable model species for evaluating the reliability of stem frequency as an indicator of plant status.

One of the key advantages of climate chamber experiments is the ability to precisely control atmospheric conditions, however some precautions must be taken for its cultivation in controlled environments [44].

In this chapter, a series of controlled trials was designed to investigate how variations in environmental parameters influence stem frequency measurements. The objective was to assess whether the observed responses are consistent with the physiological mechanisms reported in the literature for this type of plant. To this end, different climatic regimes were applied in a cyclic manner and a graphical representation of the climatic conditions imposed is depicted in figure 4.1.

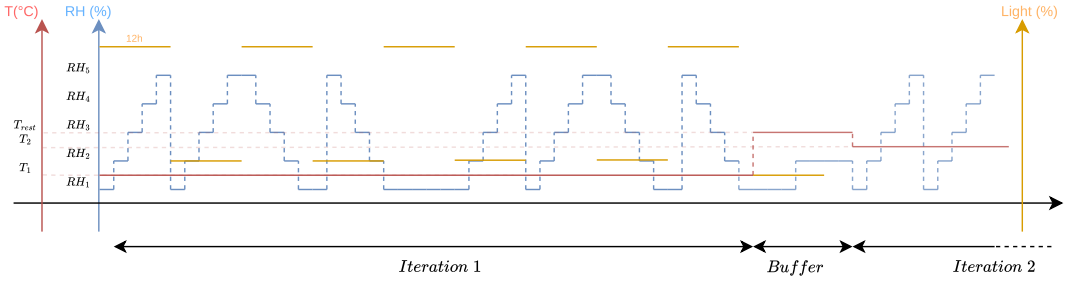


Fig. 4.1 Climatic chamber conditions

- Constant photoperiod (12 hours light / 12 hours dark)
- Multiple iterations with constant temperature and relative humidity varying dynamically between 40% and 80%, following ramp-up and ramp-down profiles
- Each relative humidity step duration is 2 hours,

These conditions are inherently artificial and do not reflect open-field environments. Moreover, by varying only a single variable at a time, it is not possible to fully account for the complex interactions that may still influence stem frequency measurements. Nevertheless, starting from a simplified and controlled context is a necessary step before extending the analysis to more realistic open-field conditions. For the sake of completeness and the reader's convenience, a detailed summary of the experimental protocol is presented in table 4.1.

In Figure 4.2, an overview of the data collected during the experimental period is shown. The only preprocessing applied here is the a simple baseline normalization. The samples reported in figure 4.2 are evaluated as:

$$StemFreq_{norm} = \frac{StemFreq_{raw} - baseline}{baseline} \tag{4.1}$$

Table 4.1 Detailed experimental protocol used to investigate the effect of temperature and relative humidity on plant stem frequency.

Temp.($^{\circ}C$)	**Iteration**	**Step**	**RH(%)**
16	1	1	$40 \rightarrow 50 \rightarrow 60 \rightarrow 70 \rightarrow 80$
16	1	2	$40 \rightarrow 50 \rightarrow 60 \rightarrow 70 \rightarrow 80 \rightarrow 70 \rightarrow 60 \rightarrow 50 \rightarrow 40$
16	1	3	$40 \rightarrow 80 \rightarrow 70 \rightarrow 60 \rightarrow 50 \rightarrow 40$
16	1	1	$40 \rightarrow 50 \rightarrow 60 \rightarrow 70 \rightarrow 80$
16	1	2	$40 \rightarrow 50 \rightarrow 60 \rightarrow 70 \rightarrow 80 \rightarrow 70 \rightarrow 60 \rightarrow 50 \rightarrow 40$
16	1	3	$40 \rightarrow 80 \rightarrow 70 \rightarrow 60 \rightarrow 50 \rightarrow 40$
			Buffer: 25 °C, 60% RH
18	2	1	$40 \rightarrow 50 \rightarrow 60 \rightarrow 70 \rightarrow 80$
18	2	2	$40 \rightarrow 50 \rightarrow 60 \rightarrow 70 \rightarrow 80 \rightarrow 70 \rightarrow 60 \rightarrow 50 \rightarrow 40$
18	2	3	$40 \rightarrow 80 \rightarrow 70 \rightarrow 60 \rightarrow 50 \rightarrow 40$
18	2	1	$40 \rightarrow 50 \rightarrow 60 \rightarrow 70 \rightarrow 80$
18	2	2	$40 \rightarrow 50 \rightarrow 60 \rightarrow 70 \rightarrow 80 \rightarrow 70 \rightarrow 60 \rightarrow 50 \rightarrow 40$
18	2	3	$40 \rightarrow 80 \rightarrow 70 \rightarrow 60 \rightarrow 50 \rightarrow 40$
			Buffer: 25 °C, 60% RH
20	3	1	$40 \rightarrow 50 \rightarrow 60 \rightarrow 70 \rightarrow 80$
20	3	2	$40 \rightarrow 50 \rightarrow 60 \rightarrow 70 \rightarrow 80 \rightarrow 70 \rightarrow 60 \rightarrow 50 \rightarrow 40$
20	3	3	$40 \rightarrow 80 \rightarrow 70 \rightarrow 60 \rightarrow 50 \rightarrow 40$
20	3	1	$40 \rightarrow 50 \rightarrow 60 \rightarrow 70 \rightarrow 80$
20	3	2	$40 \rightarrow 50 \rightarrow 60 \rightarrow 70 \rightarrow 80 \rightarrow 70 \rightarrow 60 \rightarrow 50 \rightarrow 40$
20	3	3	$40 \rightarrow 80 \rightarrow 70 \rightarrow 60 \rightarrow 50 \rightarrow 40$
			Buffer: 25 °C, 60% RH
22	4	1	$40 \rightarrow 50 \rightarrow 60 \rightarrow 70 \rightarrow 80$
22	4	2	$40 \rightarrow 50 \rightarrow 60 \rightarrow 70 \rightarrow 80 \rightarrow 70 \rightarrow 60 \rightarrow 50 \rightarrow 40$
22	4	3	$40 \rightarrow 80 \rightarrow 70 \rightarrow 60 \rightarrow 50 \rightarrow 40$
22	4	1	$40 \rightarrow 50 \rightarrow 60 \rightarrow 70 \rightarrow 80$
22	4	2	$40 \rightarrow 50 \rightarrow 60 \rightarrow 70 \rightarrow 80 \rightarrow 70 \rightarrow 60 \rightarrow 50 \rightarrow 40$
22	4	3	$40 \rightarrow 80 \rightarrow 70 \rightarrow 60 \rightarrow 50 \rightarrow 40$
			Buffer: 25 °C, 60% RH
24	5	1	$40 \rightarrow 50 \rightarrow 60 \rightarrow 70 \rightarrow 80$
24	5	2	$40 \rightarrow 50 \rightarrow 60 \rightarrow 70 \rightarrow 80 \rightarrow 70 \rightarrow 60 \rightarrow 50 \rightarrow 40$
24	5	3	$40 \rightarrow 80 \rightarrow 70 \rightarrow 60 \rightarrow 50 \rightarrow 40$
24	5	1	$40 \rightarrow 50 \rightarrow 60 \rightarrow 70 \rightarrow 80$
24	5	2	$40 \rightarrow 50 \rightarrow 60 \rightarrow 70 \rightarrow 80 \rightarrow 70 \rightarrow 60 \rightarrow 50 \rightarrow 40$
24	5	3	$40 \rightarrow 80 \rightarrow 70 \rightarrow 60 \rightarrow 50 \rightarrow 40$

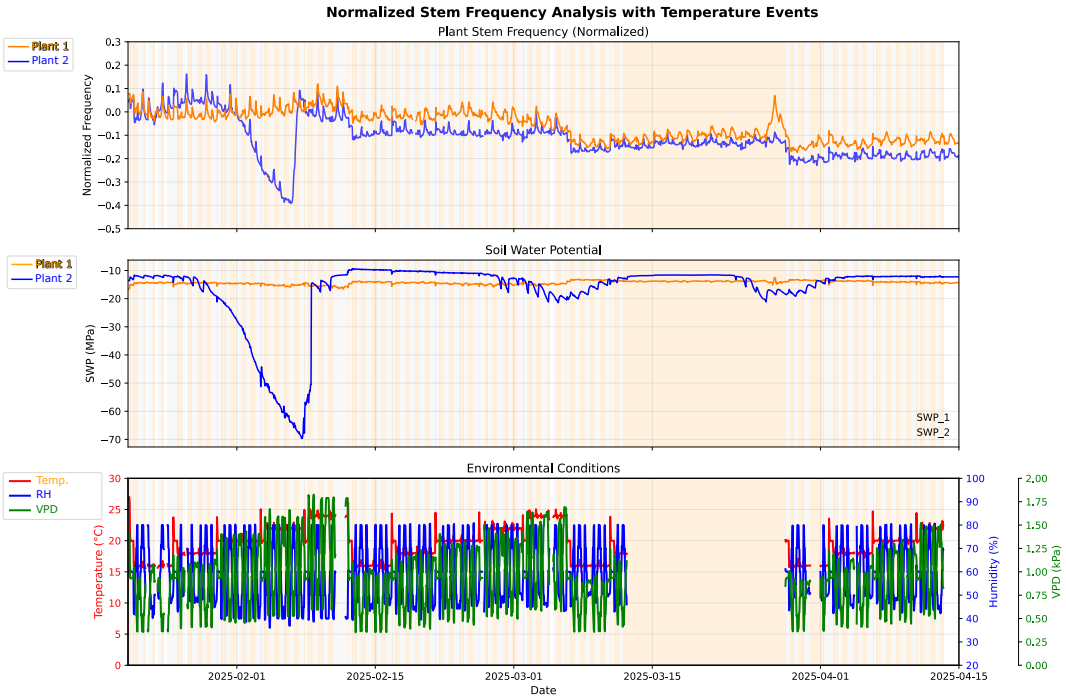


Fig. 4.2 Overall view if the data collected over the experimental period. The top panel shows the measured stem frequency. The middle panel presents the corresponding soil water potential. The bottom panel illustrates the applied environmental conditions, temperature and relative humidity, alongside the calculated VPD. Areas with a light orange background indicate periods when the light source was active. Note that the period approximately from *2025-03-15* to *2025-04-01* presents missing data from climatic chamber. This period will not be considered during the following analysis but it is still included in the visualization for completeness.

where $baseline$ is the average of all the samples collected during the week immediately before the beginning of the experiment.

Equation 4.1 basically calculates the relative difference compared to the initial plant baseline. As an example: supposing 10 kHz as a baseline frequency, and a reading of 10.2 kHz, $freq_{norm}$ will be evaluated as 0.02 i.e. the 2% increase compared to the initial baseline value.

The normalization was necessary due to the interplant differences that makes measurements have different starting value, this way it is easier to compare and visualize two different plants. As can be observed in the lower panel, the environmental "staircase" climate conditions imposed by the climate chamber programming are clearly visible. The middle panel illustrates the soil water potential, which was monitored throughout the study, with plants subjected to two distinct water regimes:

the first plant was maintained under constant irrigation, as evidenced by values close to 0 kPa (almost saturated soil). The second plant, however, underwent a period of moderate water stress followed by a subsequent phase of constant irrigation, allowing for an assessment of the effects of water stress on plant behavior in terms of stem water status. Furthermore, it was decided not only to analyze separately the variations in stem frequency in relation to temperature and humidity, but also to consider the air water VPD in the data analysis, which is more closely related to plant water uptake in controlled and environments such as climatic chambers, and it also important for correct plant growth [43]. VPD was calculated based on measurements of temperature and relative humidity recorded within the growth chamber. Ideally, integrating the canopy temperature reading would have improved the accuracy of the measurement; however, since this data is not available in the current experimental setup, the VPD was calculated from chamber temperature and relative humidity using a simplified, equation. VPD is defined as the difference between the amount of moisture actually present in the air and the amount of moisture the air can hold when saturated at a given temperature. For a greenhouse environment, it is possible to obtain a simplified formulation to estimate this parameter. Mathematically:

$$VPD = es(T_m) - e_a \text{ [kPa]} \tag{4.2}$$

where e_s is saturation vapour pressure at measured temperature T_m and e_a is the actual vapour pressure. To evaluate e_s at a certain temperature it is possible to employ the empirical Tetens' formula:

$$e_s(T) = 0.6108 \cdot \exp\left(\frac{17.27\,T}{T + 237.3}\right) \text{ [kPa]} \tag{4.3}$$

At this point, it is possible to apply the definition of relative humidity:

$$RH = 100 \cdot \frac{e_a}{e_s} \rightarrow e_a = \frac{RH}{100} \cdot e_s \tag{4.4}$$

and finally we obtain the employed simplified equation for calculating the vapour pressure deficit.

$$VPD = 0.6108 \cdot e^{\frac{(17.27 \cdot T)}{(T+273.3)}} \cdot \left(1 - \frac{RH}{100}\right) \text{ [kPa]} \tag{4.5}$$

Briefly, and with some simplification, higher VPD values indicate lower moisture in vegetation and therefore drier conditions, whereas lower VPD values indicate wetter conditions. Intuitively, VPD is like the "drying power" of the air: when VPD is high, the air can pull more water from leaves (like a dry sponge), so plants lose water faster; when VPD is low, the air is closer to saturation and plants lose water more slowly. Figure 4.3 shows a visualization for the VPD in function of temperature and relative humidity.

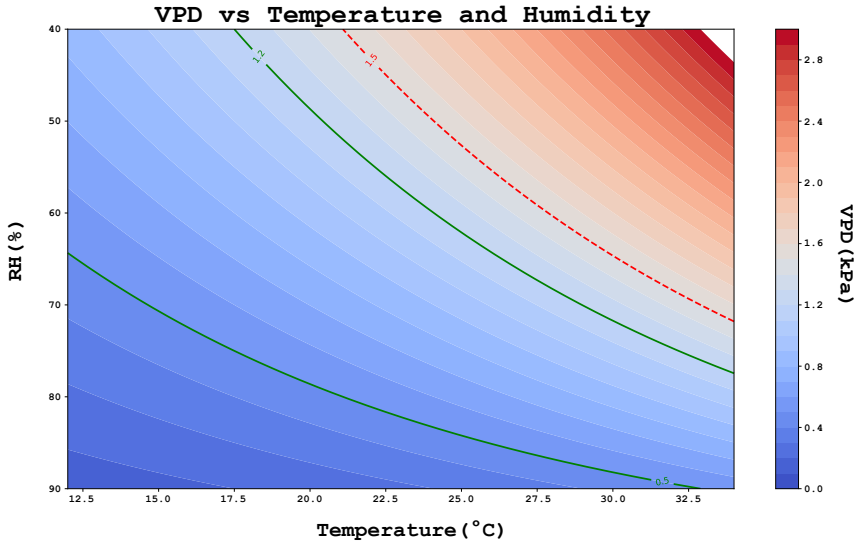


Fig. 4.3 Visualization of the behaviour of VPD against the imposed temperature and RH.

It should be also noted, however, that there are different studies that specifies different optimal values for the VPD for the growth of tomato plants, some of them are shown in this review paper [43].

4.2.1 Temperature Analysis

The main objective of this section is to numerically analyze the correlation (and potential causality) between stem frequency and environmental variables. Temperature plays a key role in plant physiological processes, directly influencing metabolic activity, transpiration rates, water transport within the xylem and fruit production [43, 45, 46]. Different studies specifies different ideals temperatures for tomatoes depending also on the growing stage of the plant [43]. Variations in temperature can therefore induce measurable changes in stem dynamics, which are expected to be

reflected in the stem frequency signal. In this section we will deal with tomato plants kept under regular watering conditions as opposed to next sections.

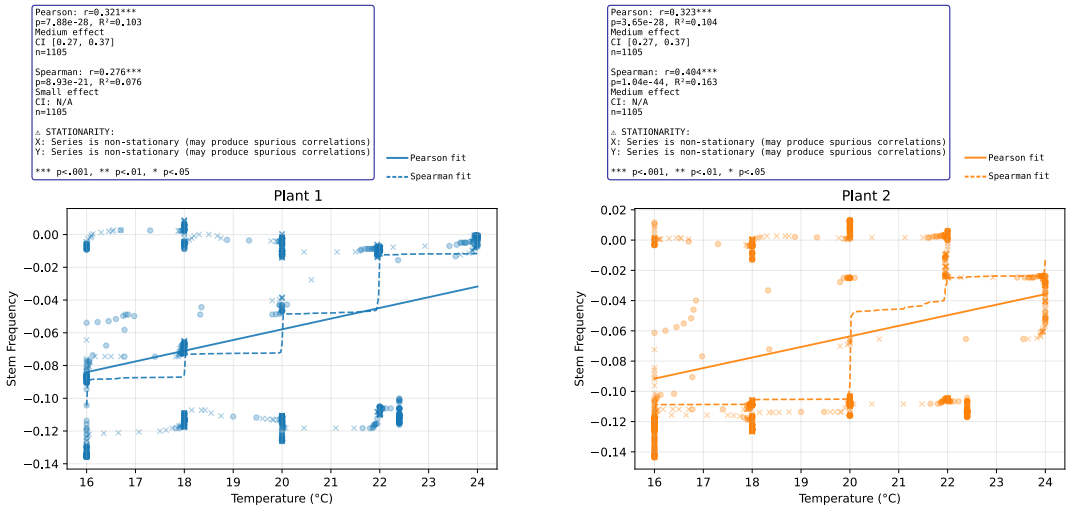


Fig. 4.4 Scatter plot representing chamber air temperature (°C) against normalized stem frequency with equation 4.5 for each of the plants under test. "X" markers in the plots indicate that the sample was with light turned off.

As a first step, the statistical correlation between stem frequency and ambient temperature is analyzed. Figure 4.4 shows a scatter plot used to evaluate the relationship between temperature and stem frequency. For each plant, both Pearson and Spearman correlation coefficients were computed. From the figure, a quantized pattern can be observed. This behavior is a direct consequence of the control program applied in the climate chamber, schematically shown in Figure 4.1. Such environmental quantization appears to be reflected in the plant measurements as well. The figure also reports correlation values along with the corresponding fits (linear for Pearson and rank-based for Spearman).

It can be noted, however, that both time series exhibit non-stationarity, moreover the repeated measurements on the same plant of stem frequency can't be considered completely independent. For this reason, a detrending procedure was applied to the stem frequency measurements in order to avoid spurious correlations and, consequently, misleading interpretations of the results, however particular care should be given when interpreting these results. Here, the focus is on analyzing the immediate effects that environmental variations exert on the plant, and therefore on the stem frequency signal. Other processes, such as stem growth or stress responses, may introduce slower dynamics in the form of long-term drifts, which appear as trends in

the data. This trend is estimated using the *polyfit* method from NumPy [47], which implements a least squares approach to fit a regression line to the data. The result of this processing is shown in figure 4.5 where long term changes in stem frequency are removed.

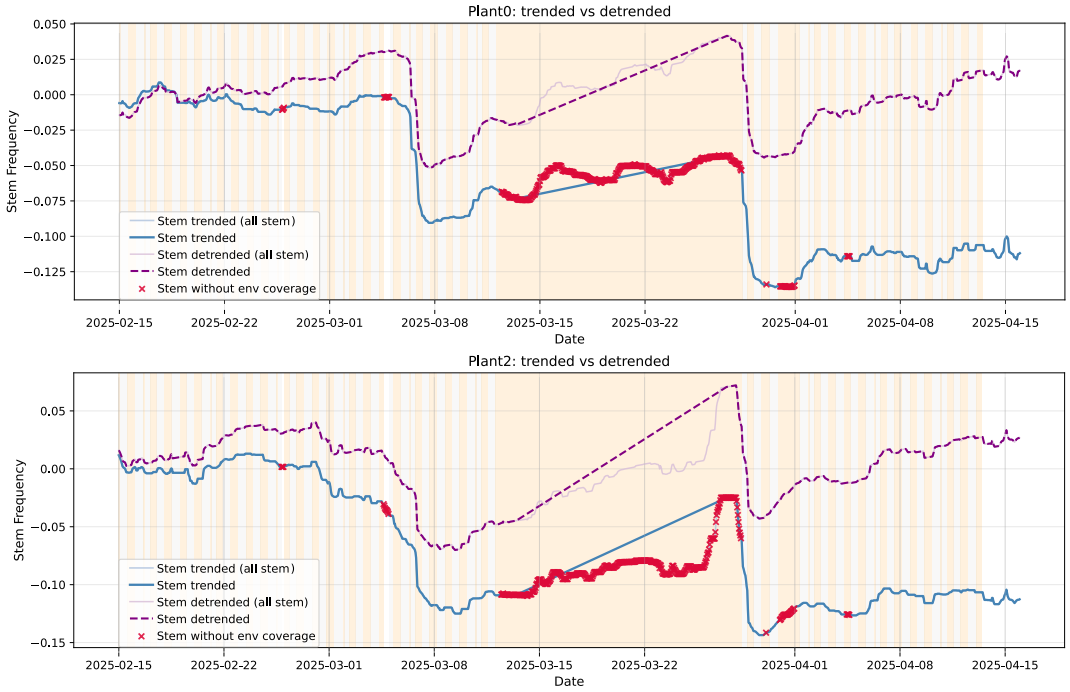


Fig. 4.5 Stem frequency data for both plants under test and corresponding detrending results. Image also shows data that has no corresponding environmental measurements. This data is excluded from the following analysis.

As shown in Figure 4.5, no climate chamber data are available for the period between *14-03-2025* and *28-03-2025* due to a failure in the climatic chamber logging platform. This data was excluded from the analysis; however, stem frequency sensor readings are still reported in the figure for completeness. Furthermore, the same figure highlights the effect of removing the long-term trend from the raw data. A detrending procedure was not applied to the temperature signal. This choice is justified by the fact that the climate chamber follows a predefined control program, designed to return to its initial conditions at the end of each cycle. Therefore, the temperature signal does not exhibit an intrinsic long-term drift. Minor deviations due to control imperfections or sensor noise cannot be completely excluded, but these effects can be considered negligible compared to the imposed cyclic variation and should not induce any spurious correlation. At this point, correlation analysis between temperature

and detrended stem frequency is again performed. Figure 4.6 reports the scatterplot applying detrending on stem frequency measurements.

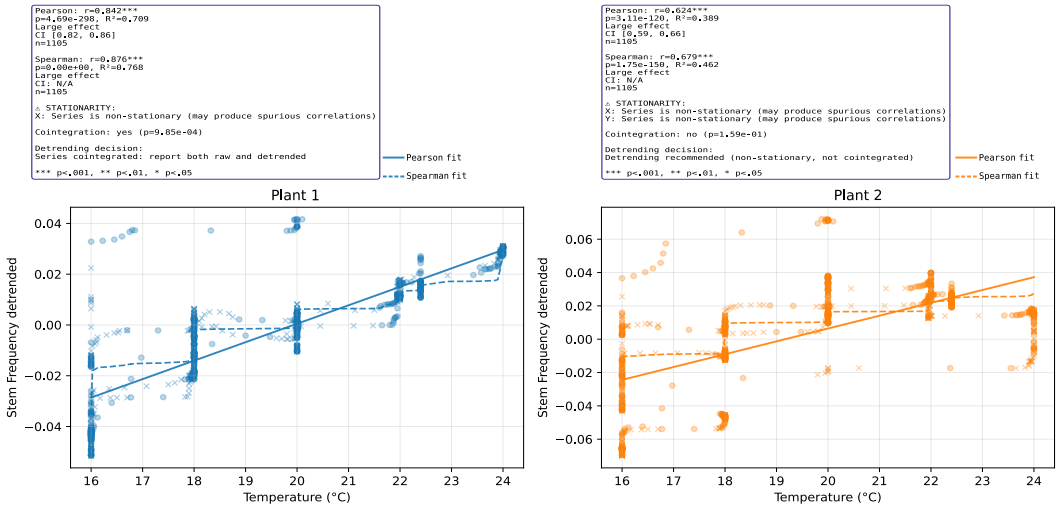


Fig. 4.6 Scatter plot representing chamber air temperature (°C) against normalized stem frequency with equation 4.5 , as well as detrending, for each of the plants under test. "X" markers in the plots indicate that the sample was with light turned off

It can be observed that, for both plants, the relationship with temperature variations is more pronounced. A large portion of the variance in stem frequency measurements can be explained by the temperature changes imposed by the climatic chamber. This is further supported by the Pearson and Spearman correlation coefficients, which are close to 1, indicating a strong dependence.

A first intuitive explanation is that plant tissues are largely composed of water, whose electrical conductivity increases with temperature. A second and more physiologically grounded explanation would be that higher temperatures are generally associated with increased stomatal conductance [16, 15], and consequently with higher evapotranspiration rates. Stomatal opening leads to increased transpiration, which in turn enhances the transport of sap within the stem. This modifies the internal ionic flow and overall conductivity of the tissue, thereby affecting the measured stem frequency. However, if a plant is exposed to high evaporative demand (i.e., higher temperatures at constant RH) for an extended period, it may close its stomata to limit excessive water loss. In the experimental scenario described above, however, this response is unlikely to have occurred, since each temperature level was maintained for only two hours. Moreover, the highest temperature considered (24 °C) was within a range suitable for tomato growth. These observations are broadly consistent with

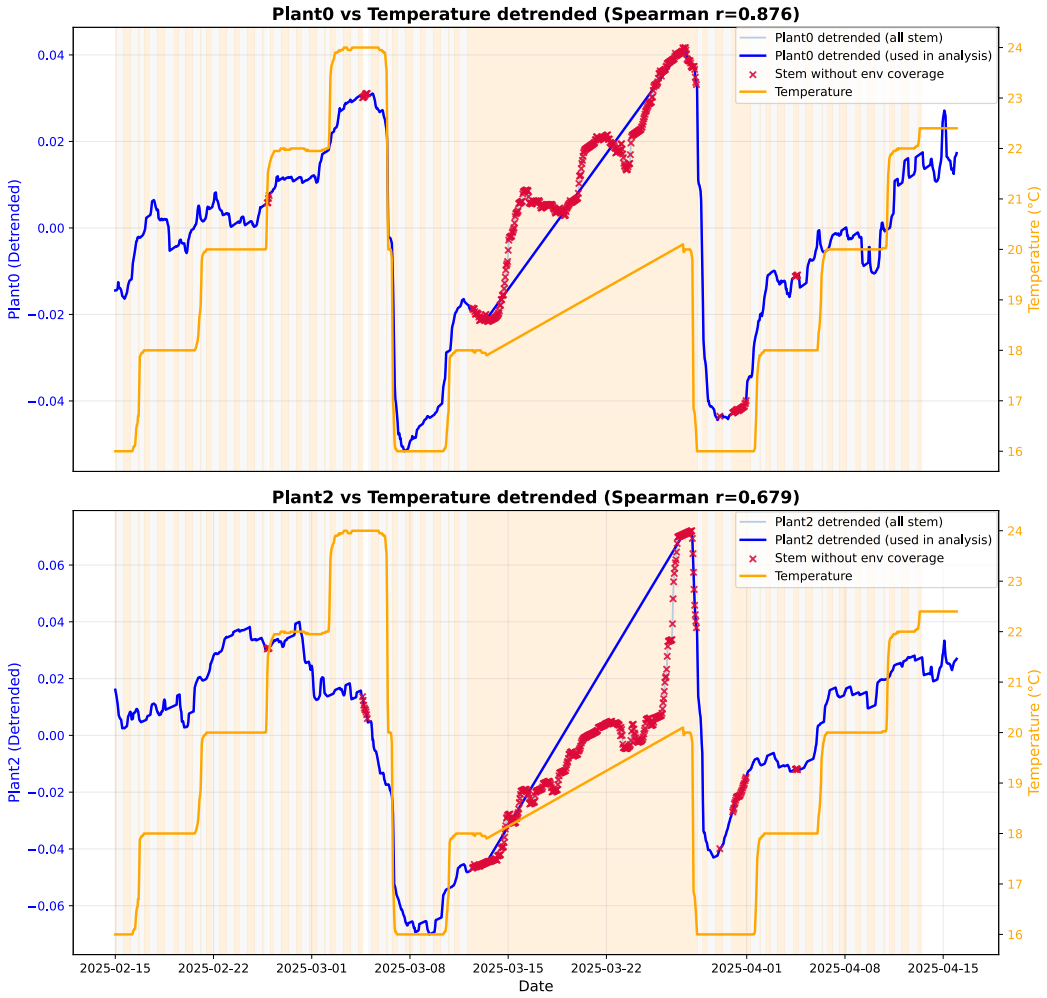


Fig. 4.7 Detail of measured stem frequency against the imposed temperature for both plants under test.

the existing literature; however, they should not be considered definitive, as further validation on a larger sample of plants is required to confirm these relationships.

4.2.2 Relative Humidity Analysis

The same analysis procedure was applied, this time focusing on the relative humidity imposed within the climate chamber. The experimental programs were designed to span multiple relative humidity levels, ranging from 40% to 80%, for each fixed temperature condition.

Figure 4.8 shows the relationship between detrended stem frequency and relative humidity. Compared to the temperature case, the observed trends appear to be less strongly related. This is reflected in the relatively low correlation values, with Spearman coefficients of 0.344 and 0.194, and Pearson coefficients of 0.371 and 0.231 for plants 1 and 2, respectively.

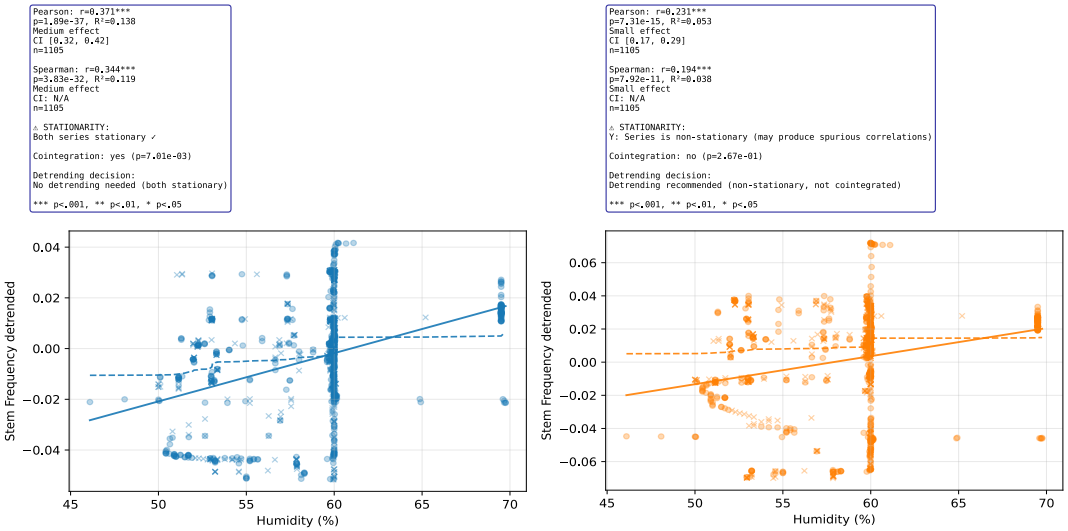


Fig. 4.8 Scatter plot representing chamber relative humidity (%) against normalized stem frequency with equation 4.2 , as well as detrending, for each of the plants under test. "X" markers in the plots indicate that the sample was with light turned off

In figure 4.9 it is reported the time behaviour of the two quantitities during the period under analysis.

However, this result should be interpreted with caution. From visual inspection and preliminary analyses, relative humidity appears to have a limited influence on stem frequency. However, when considering the entire measurement period, it is important to note that multiple relative humidity levels (40–50%, 60%, 70%, and 80%) are observed within the same temperature ranges. As a consequence, the effect of relative humidity may be masked by the stronger influence of temperature. For this reason, a stratified analysis based on both temperature and relative humidity was performed.

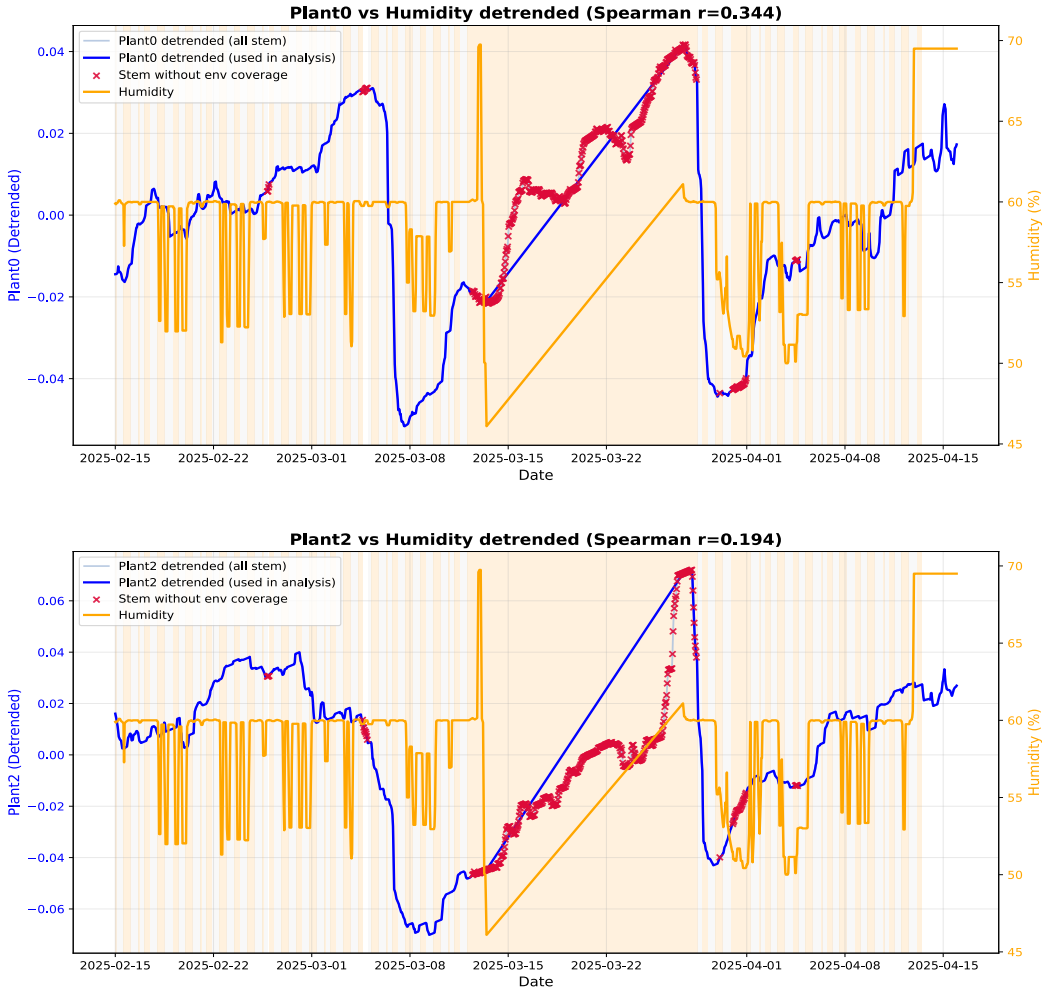


Fig. 4.9 Detail of measured stem frequency against the imposed relatve humidity for both plants under test. Red points represent stem frequency samples that don't have corresponding climatic chamber measurements.

4.2.3 Stratified Analysis

For each temperature step, the correlation between relative humidity and stem frequency was computed. This stratified approach allows assessing the consistency of the observed effects under controlled temperature conditions. From the analysis, it clearly emerges that temperature has a stronger and more direct influence on stem frequency compared to relative humidity, in agreement with the findings presented in the previous sections. In particular, after detrending, the relationship between temperature and stem frequency becomes significantly more pronounced, with the average correlation increasing from 0.24 (when long-term trends are included) to

0.90 when focusing on short-term dynamics. Moreover, the correlation values remain relatively consistent across different temperature steps, suggesting a robust and reproducible effect. In contrast, the behavior associated with relative humidity is markedly different. For both plants, the correlation with stem frequency tends to decrease as temperature increases, indicating a possible interaction between the two environmental variables. Additionally, the effect of detrending is less pronounced in this case, suggesting that relative humidity primarily influences the signal at shorter time scales or with a weaker overall impact. Some variability across humidity steps can be observed, particularly for Plant 1 at 22°C, where a deviation from the general trend is evident and may represent an outlier or a transient response.

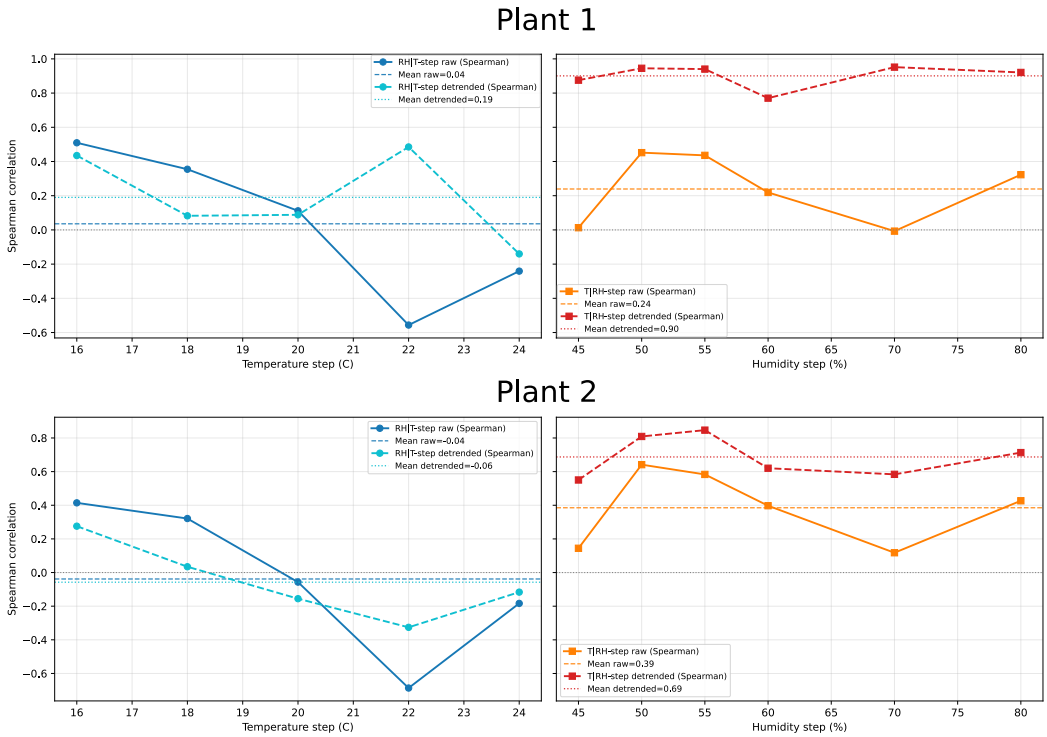


Fig. 4.10 Stratified temperature and humidity analysis vs Stem frequency

4.2.4 Vapour Pressure Deficit

Although temperature and relative humidity are independently controlled within the climate chamber, their combined effect on plant physiology is better described through the VPD, which integrates both variables [43, 48], moreover this variable has been reported as more closely related to plant evapotranspiration and stomatal

conditions . The dependency of the observed correlations on temperature levels suggests the presence of interaction effects, further supporting the need to analyze the relationship between stem frequency and VPD. For this reason, the behavior of stem frequency was further analyzed as a function of vapor pressure deficit.

From the scatter plots and statistical tests reported in Fig. 4.11, it can be observed that stem frequency is also significantly related to VPD. In this case, the relationship appears to be direct, i.e., an increase in the evaporative demand of the air corresponds to an increase in stem frequency measurements.

However, as shown in Fig. 4.11, this relationship tends to saturate at higher VPD levels, exhibiting an x–y trend that resembles a sigmoidal function.

The observation that higher vapor pressure deficit values correspond to higher stem frequency (i.e., increased stem conductivity and reduced electrical impedance) may indicate that, under hotter and drier conditions, the plant increases its transpiration rate. However, this mechanism appears to reach a limit, as the plant progressively restricts transpiration under more extreme VPD conditions, leading to a saturation effect in the observed relationship.

This behavior is observed under controlled and non-stress conditions. As will be shown in the following section, this relationship weakens or disappears when additional stress factors are introduced, which may further affect water and nutrient transport within the plant.

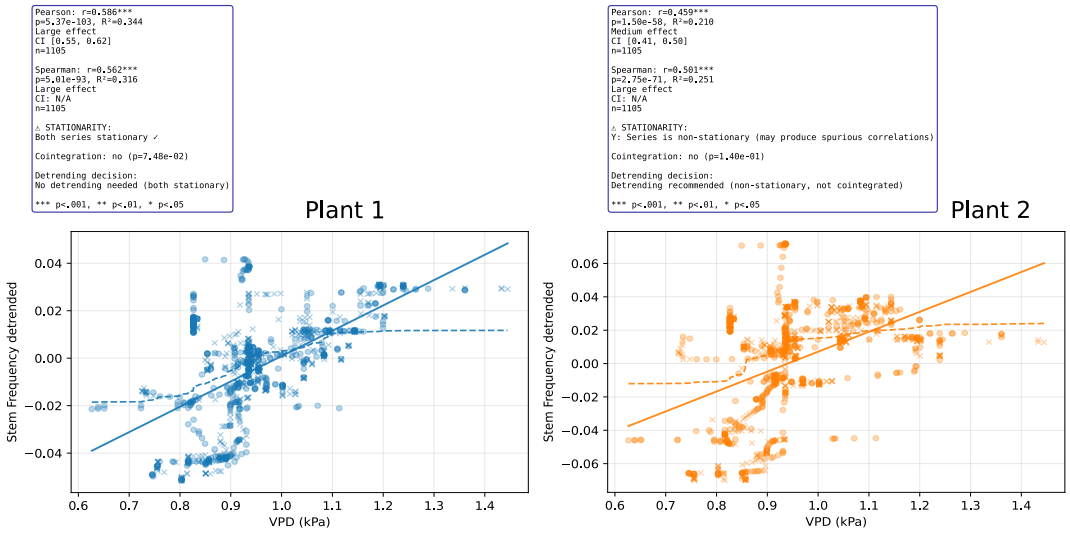


Fig. 4.11 Detail of measured stem frequency against the vapour pressure deficit for both plants under test.

Furthermore, Fig. 4.12 shows the temporal evolution of stem frequency and vapor pressure deficit for both plants. Despite some acceptable differences, the trends of the two variables follow a very similar pattern. This observation is consistent with the results reported in Fig. 4.11, where the Spearman correlation coefficients are greater than 0.5 for both plants (specifically 0.562 and 0.501).

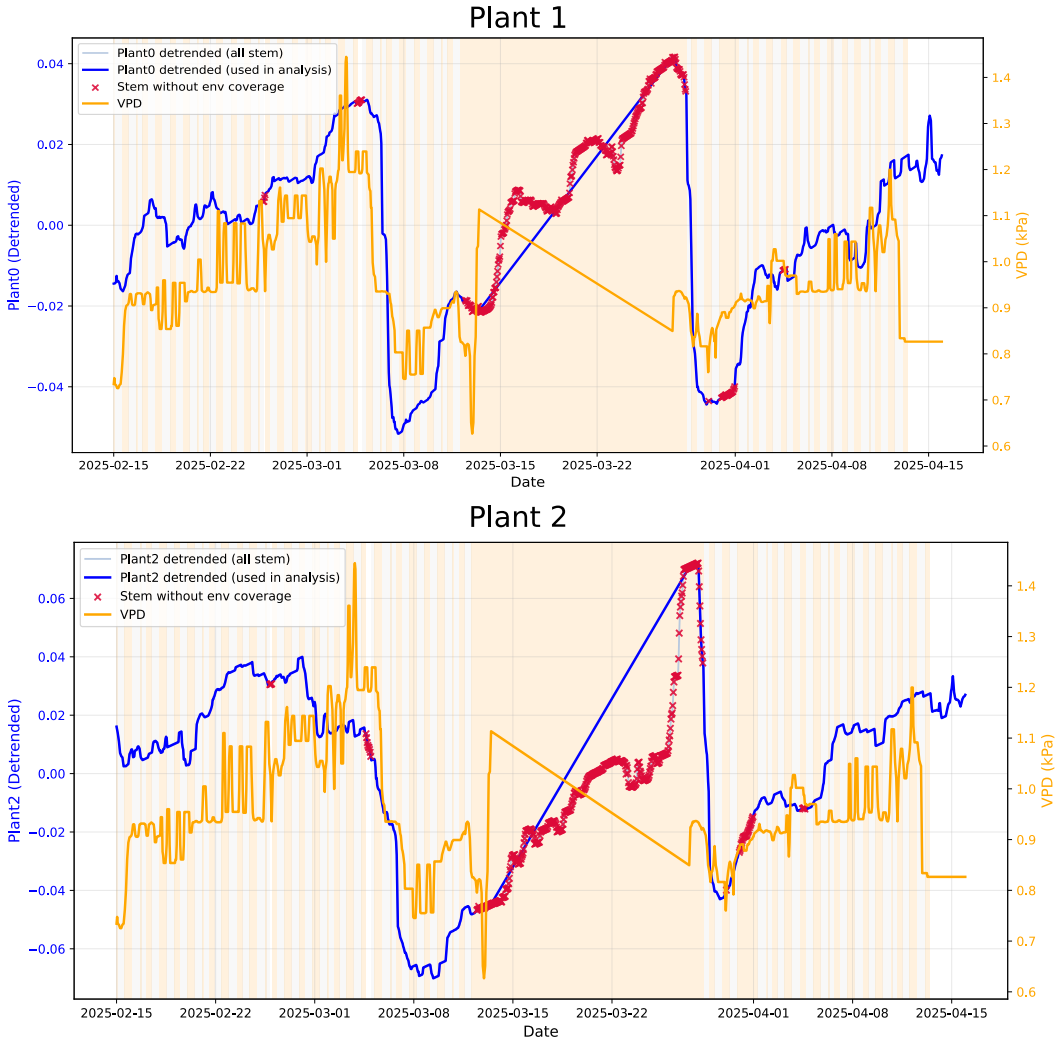


Fig. 4.12 Detail of measured stem frequency against the imposed VPD for both plants under test. Red points represents stem frequency samples that don't have corresponding climatic chamber measurements.

This preliminary result is particularly interesting, as several studies in the literature highlight the importance of vapor pressure deficit in the assessment of drought stress conditions. The observed relationship suggests that electrical impedance measurements obtained through the stem frequency method may also be effectively

employed for this purpose. However, it is important to note that, in these initial climate chamber experiments, the explored VPD range was relatively limited. The VPD levels achievable in open-field conditions, especially during hot and dry summer days, are significantly higher than those reached in this first series of measurements. Moreover, as clearly explained in the FAO guidelines [21], plant evapotranspiration depends on several factors, including VPD, radiation, and wind. It is worth noting that, although ventilation is present in the climate chamber, it was not considered in this study and can be tackled as a future work.

4.2.5 Causality Analysis

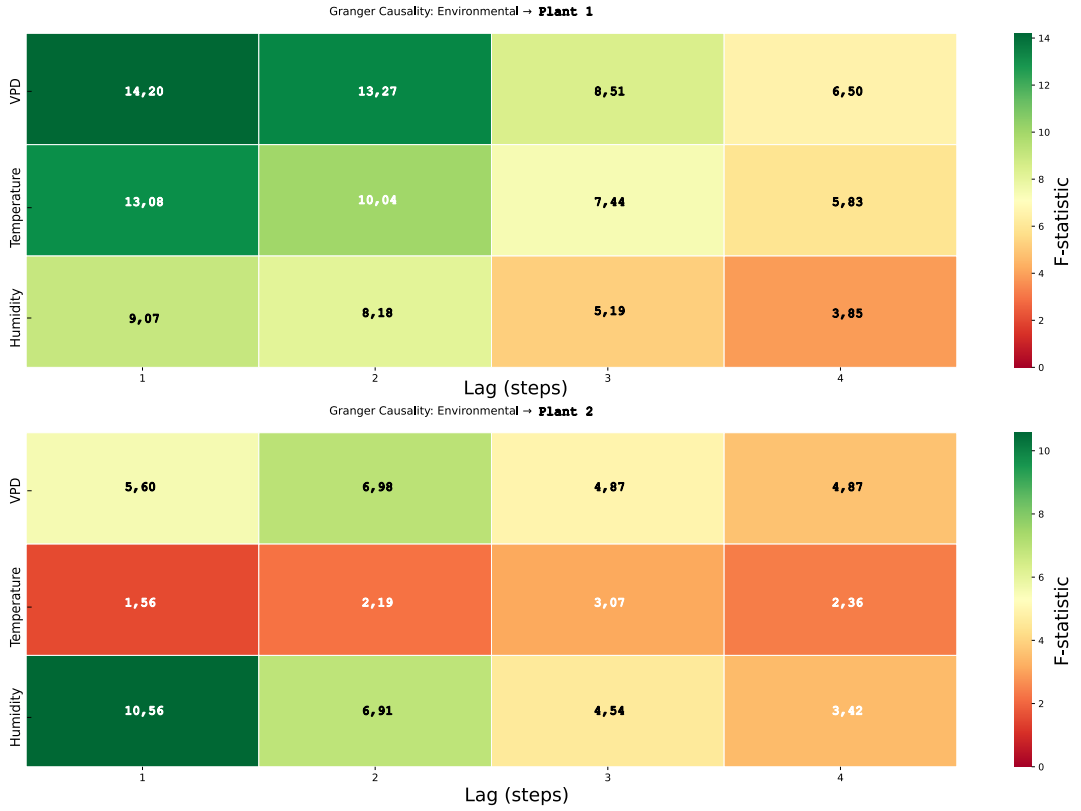


Fig. 4.13 Granger causality matrix. Each environmental variable is used to predict stem frequency.

As a final step before analyzing plant behavior under water stress conditions, a causality analysis was performed. It is well known that correlation does not imply causation; therefore, a Granger causality test was applied between stem frequency and the environmental variables measured in the climate chamber.

This statistical test evaluates whether a time series provides useful information for predicting another. In particular, a variable X is said to *Granger-cause* a variable Y if including past values of X in an autoregressive model of Y improves its prediction.

The results of this analysis are shown in Figure 4.13, where the F-statistic is reported for each lag. Higher values indicate a stronger contribution of the corresponding variable in predicting changes in stem frequency. The x-axis represents the number of autoregressive lags considered in the model. Overall, Figure 4.13 confirms what was qualitatively observed in the temporal trends discussed in previous sections, namely that changes in environmental variables are followed by variations in stem frequency. It can also be observed that lower lags generally correspond to higher F-statistics, suggesting a relatively fast response of the plant system. Moreover, different behaviors can be identified between the two plants. For a fixed lag, the Granger coefficients vary significantly, highlighting the role of physiological variability between individuals. In particular, the relationship between Plant 1 and VPD appears especially strong. VPD shows consistently high F-statistics, indicating a significant influence on stem frequency. This is particularly interesting since VPD is directly related to plant transpiration, suggesting that stem frequency may be closely linked to evapotranspiration processes within the plant.

4.3 Response under water stress

The analysis presented in the previous section was done under proper irrigation conditions. It is of interest to extend the analysis to conditions of reduced substrate irrigation, considering the period from *2025-01-21* to *2025-02-13*, during which plant 1 did not receive any irrigation.

Figure 4.14 highlights the differences between the two plants as a function of the imposed temperature in the climate chamber, with Plant 1 subjected to a progressive reduction in soil water potential, and therefore to an increased risk of water stress.

Under these conditions, a more pronounced divergence in behavior between the two plants can be observed, likely driven by the different water availability in the soil. Plant 2, maintained under optimal irrigation conditions, exhibits a response that is consistent with the temperature profile: an initial decrease corresponding to

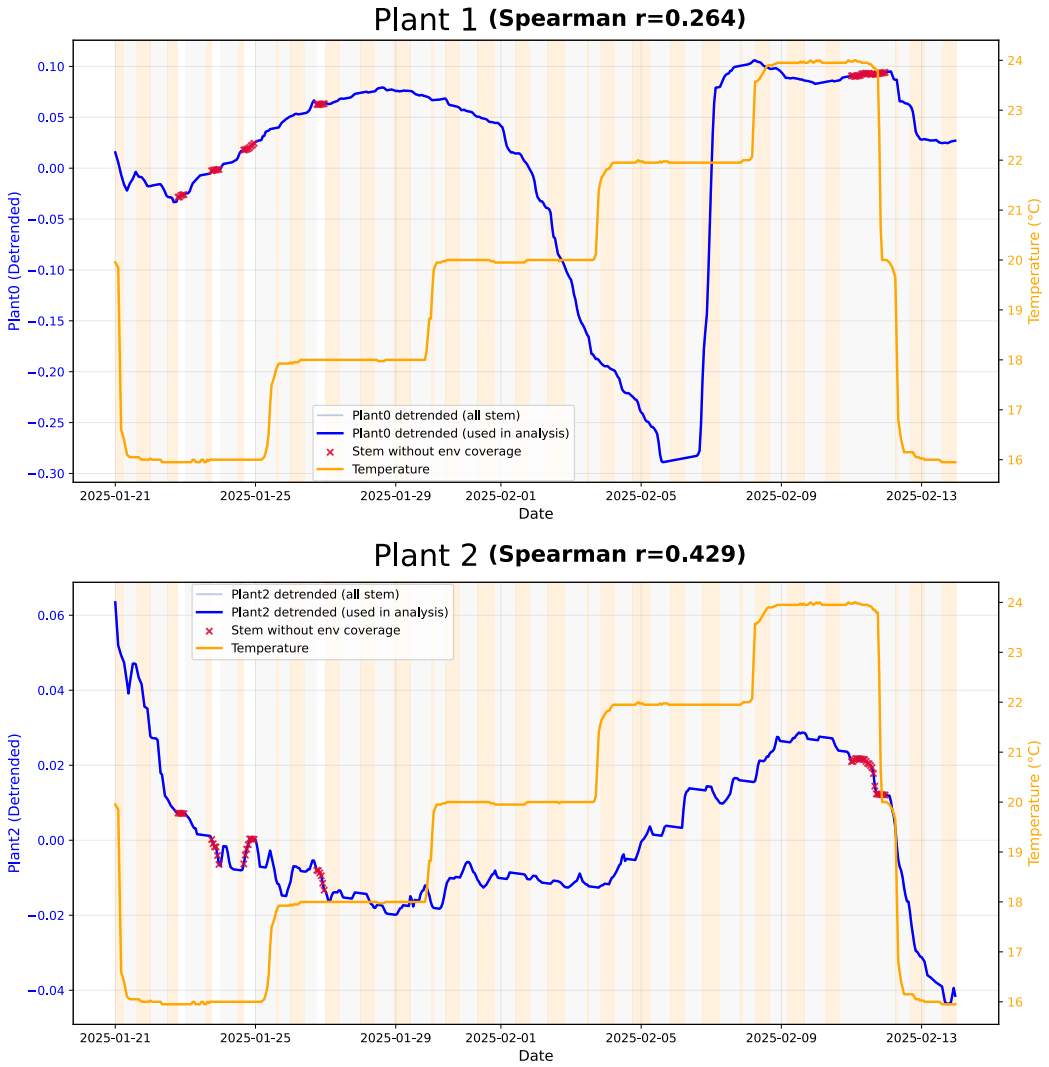


Fig. 4.14 Detail of measured stem frequency against the imposed temperature for both plants under test. Plant 1 is subjected to water stress.

the temperature drop, followed by a monotonic trend aligned with the programmed temperature steps in the climate chamber.

In contrast, Plant 1 does not consistently follow this pattern. Before the decrease in soil water potential, its behavior is comparable to that of Plant 2. However, as soil water potential progressively declines, deviations in stem frequency become evident, indicating a disruption of the previously observed relationship. This behavior is clearly visible in Figure 4.14.

To avoid overcomplicating the discussion, and given the relatively minor influence of relative humidity observed in previous analyses, the corresponding plots are omitted here and reported in the Appendix for completeness.

A similar analysis can be performed using the VPD, as shown in Figure 4.15, where the full experimental period is reported to provide a comprehensive overview. The stem frequency generally follows the VPD trend, except in the case of Plant 1 under water stress conditions. This suggests that stem frequency is influenced by environmental conditions through their effect on plant water transport and tissue properties. For instance, higher temperatures and VPD levels may increase transpiration and stomatal opening, enhancing water and nutrient flow within the stem and consequently affecting its electrical properties. However, this mechanism appears to break down under water-limited conditions. When soil water availability decreases, two main effects are expected: first, a reduced amount of water available for uptake; second, the activation of plant protective responses. In such conditions, the plant may reduce transpiration to prevent further water loss, effectively limiting internal water flow and altering the stem's electrical behavior.

Experiment summary

In the previous sections, the results of a continuous in vivo monitoring experiment of two tomato plants using stem frequency measurements were analyzed. It was observed that each environmental variable plays a role in the dynamics of stem frequency. This is likely due to the strong dependence of the plant system on these parameters for proper growth. The stem, being responsible for the transport of water and nutrients, is also affected, which is reflected in the measured stem frequency. Furthermore, it was observed that the vapor pressure deficit (VPD) has a significant impact on the signal dynamics, and that temperature generally induces larger variations in the signal compared to humidity. The water status of the soil also emerged as a key factor. In particular, stem frequency shows a strong dependence on soil water potential. Overall, the signal dynamics are regulated by environmental variations such as VPD and light. However, this regulation weakens when soil water availability decreases and the plant enters water stress conditions. This is particularly relevant, as it suggests that water stress symptoms can be detected through direct and relatively simple plant-based monitoring.

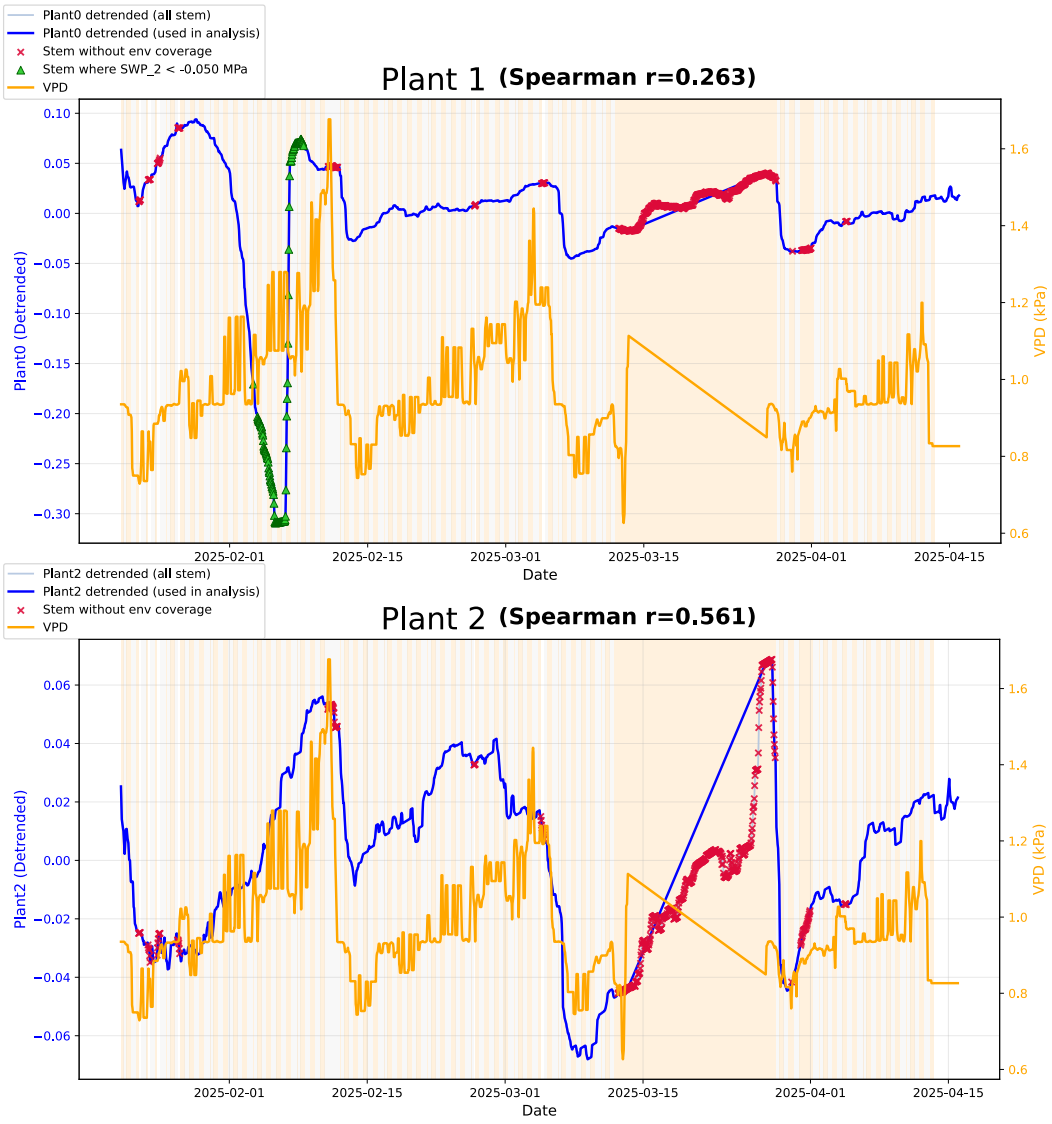


Fig. 4.15 Detail of measured stem frequency against the imposed temperature for both plants. Overview of all the experimental periods.

4.4 Photoperiod Analysis

An aspect that has been only marginally addressed so far, yet plays a fundamental role in plant physiology, is the exposure to light radiation, more generally referred to as the photoperiod. Light is essential for plant functioning, as it provides the energy required to sustain photosynthetic activity.

For this reason, an additional experimental campaign was designed to investigate the response of stem frequency under controlled photoperiod conditions, following an approach analogous to that presented in the previous sections.

4.4.1 Experimental profile

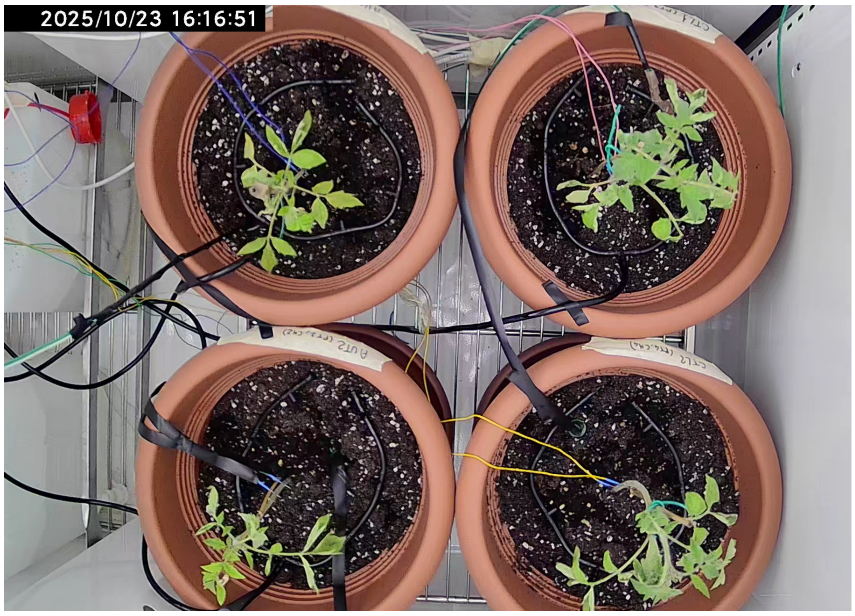


Fig. 4.16 Climatic chamber setup setup, few days before the beginning of the experiment

A dedicated experiment was therefore designed to investigate changes in stem frequency measurements by subjecting four tomato plants to different environmental conditions within a climate chamber. This approach enables the evaluation of both the overall trends and the average daily behavior under these conditions, as well as a comparison between different experimental periods. The experiment was conducted in the climate chamber from October 27, 2025, to December 12, 2025 and the camera system of figure 4.16 is employed to estimate and monitor leaf area of plants under measurements. An example of sampled images is presented in figure. As in the previous experiments, the analysis primarily focuses on stem frequency measurements. Soil water potential was also monitored; however, since all plants were maintained under well-irrigated conditions throughout the experiment, with values close to 0 kPa, it is not explicitly discussed in this section as it does not introduce significant variability.

1. **October 27, 2025 – November 10, 2025.** A 24-hour cycle was implemented with 12 hours of full light, followed by 2 hours of transition from light to darkness (dusk simulation), 8 hours of darkness, and 2 hours of transition from darkness to light (dawn simulation). Temperature was maintained at 26 °C during the light period and gradually reduced to 20 °C during the dark period, reflecting optimal growth conditions for tomato plants. Relative humidity was kept constant at 70%. Light intensity was set to 85% of the chamber maximum power during the light phase and 0% during darkness (refer to section 3.1.1 for more details about PPFD light characteristics.).

2. **November 11, 2025 – November 17, 2025.** The same photoperiod and temperature profile as in Period 1 were maintained. However, light intensity during the day was reduced to 50% of the chamber maximum light intensity, while remaining at 0% during the night.

3. **November 18, 2025 – November 27, 2025.** A shortened cycle was introduced, consisting of 6 hours of full light, 1 hour of transition to darkness, 4 hours of darkness, and 1 hour of transition back to light. Temperature followed the same day/night pattern (26 °C to 20 °C), and relative humidity was kept at 70%. Light intensity was maintained at 50% of the chamber maximum power during the light phase.

4. **November 28, 2025 – December 12, 2025.** A long photoperiod of 16 hours is introduced. However, temperature was kept constant at 20 °C throughout the entire cycle. Relative humidity remained at 70%, and light intensity was set at 50% of the chamber maximum power during the light phase.

A summary of the designed experimental periods is presented in table 4.2.

For each experimental period, the daily behavior was analyzed by plotting the measurements for each plant on a day-by-day basis. Each curve in the plot represents a different day of observation. As shown in Figure 4.17, the different plants exhibit distinct baseline values of stem frequency. To facilitate a clearer comparison of the temporal dynamics and to better highlight the changes induced by the climate chamber program, these baseline offsets were removed.

The resulting plots are shown in figures analogous to Figure 4.18, which will be presented in the following sections for each experimental period (Table 4.2). Given

Table 4.2 Summary of experimental conditions across the five periods.

Period	**Dates**	**Photoperiod**	**T** (°C)	**RH** (%)	**Light Intensity** (%)
1	Oct 27 – Nov 10	12h L / 2h dusk / 8h D / 2h dawn	26 → 20 (day → night)	70	85 (day), 0 (night)
2	Nov 11 – Nov 17	12h L / 2h dusk / 8h D / 2h dawn	26 → 20 (day → night)	70	50 (day), 0(night)
3	Nov 18 – Nov 27	6h L / 1h dusk / 4h D / 1h dawn	26 → 20 (day → night)	70	50 (day), 0 (night)
4	Nov 28 – Dec 12	16h L / 1h dusk / 6h D / 1h dawn	Constant 20	70	50 (day), 0 (night)

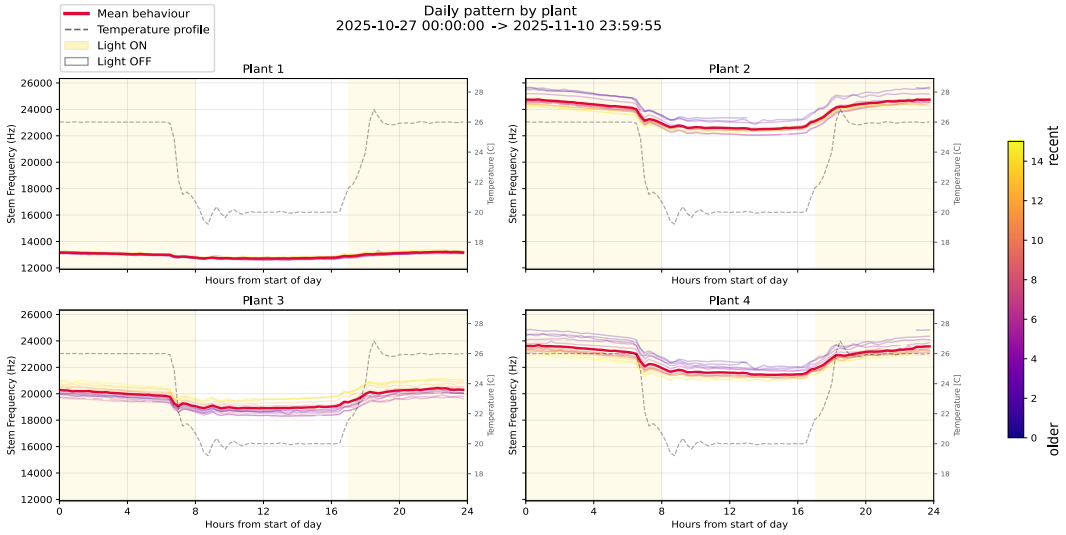


Fig. 4.17 Data from 1st experimental period. Offset included. Yellow background indicates light on, white background indicates light off. Different color curves distinguish older and recent days. Dashed line indicates the temperature profile

the availability of multiple days of observations for each plant, the average daily behavior was also evaluated. To this end, a mean daily profile was computed for each plant within each experimental period. Mathematically, for a given plant x, the average daily profile is defined as:

$$\bar{x}(h) = \frac{1}{N_h} \sum_{d=1}^{N_h} x_d(h) \tag{4.6}$$

where:

- h represents the hour of the day,
- $x_d(h)$ is the stem frequency measured at hour h on day d,
- N_h is the number of days with available measurements at hour h

In all the presented figures, each curve represents the daily evolution of stem frequency for a specific day within the considered experimental period. A colorbar is included to provide temporal information, allowing the curves to be distinguished based on their relative position within the experimental window. In particular, the color gradient encodes the progression of time, enabling a visual assessment of possible temporal drifts or adaptation effects occurring across consecutive days. A detailed analysis of the experimental protocols can be carried out starting from Period 1.

Period 1

Figure 4.18 shows that stem frequency closely follows the imposed light and temperature profiles. A similar behavior is observed for the vapor pressure deficit: since relative humidity was maintained constant at 70%, variations in evaporative demand were driven exclusively by temperature shifts.

The stem frequency appears to reflect the general physiological activity of the plant. Under higher temperatures and illumination, the observed signal is consistent with an increased conductivity of the stem, likely associated with enhanced transpiration, stomatal activity, and a greater flux of water and nutrients. This aspect is interesting and as future work should be explored more, for example by comparing stem frequency measurements with sap flow sensor

A detailed quantitative evaluation of the daily mean profiles (evaluated using Equation 4.6) is summarized in Table 4.3. Inter-plant variability in daily amplitude is clearly evident. Plant 1 exhibits the lowest response, recording a daily amplitude of 509 Hz (3.9% relative variation) and a variance of 181. Conversely, Plants 2 and 4

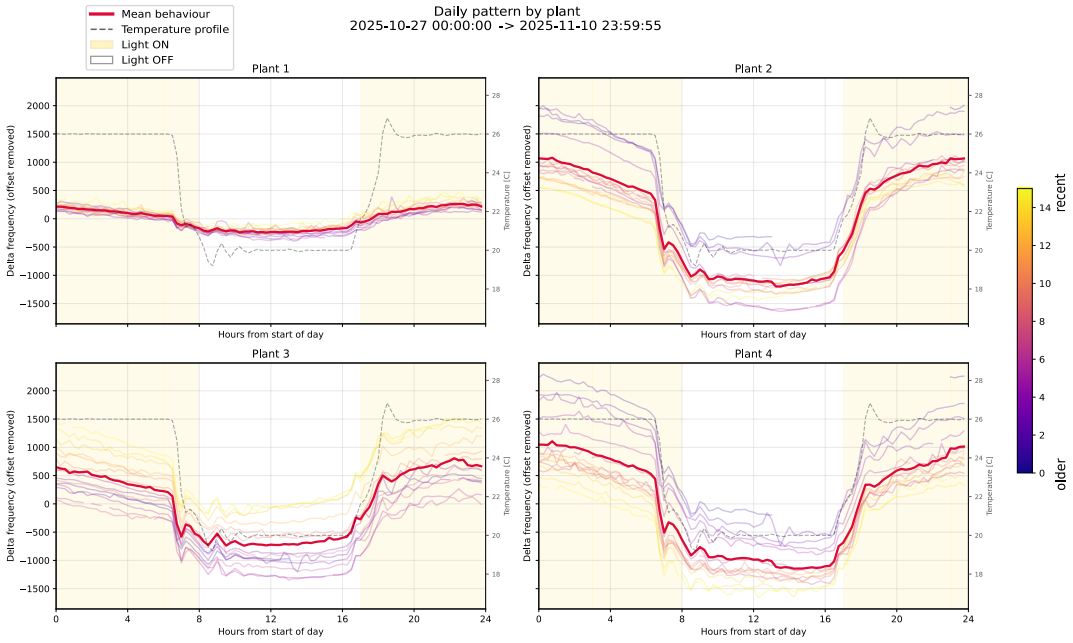


Fig. 4.18 Data from 1st experimental period. Offset removed. Yellow background indicates light on, white background indicates light off. Different color curves distinguish older and recent days. Dashed line indicates the temperature profile

display significantly higher daily excursions, reaching amplitudes of 2278 Hz (9.6% relative variation, variance 897) and 2252 Hz (10.0% relative variation, variance 850), respectively, while Plant 3 shows an intermediate amplitude of 1548 Hz (7.9% relative variation, variance 581). Lower baseline stem frequency values thus tend to associate with less pronounced daily variations.

Regarding peak timing, the daily maxima are aligned across specimens, occurring between 22:15 (Plant 3) and 00:45 (Plants 2 and 4), consistent with the forced climate chamber cycle times. Statistical correlations further quantify this strong coupling: temperature correlations (T_{corr}) reach 0.95 for Plant 1, 0.98 for Plant 2, 0.96 for Plant 3, and 0.97 for Plant 4. Identical correlation coefficients are observed for light intensity (L_{corr}) because temperature and light were varied synchronously during this period, making it impossible to decouple their individual contributions.

With regard to the correlation results, they are consistent with those previously discussed, showing a strong dependence on temperature. Conversely, the correlation with light is less informative: during this first experimental period, temperature and light vary synchronously within the climate chamber protocol, making it difficult to

decouple their effects and therefore reducing the interpretability of the correlation with light.

Period 2

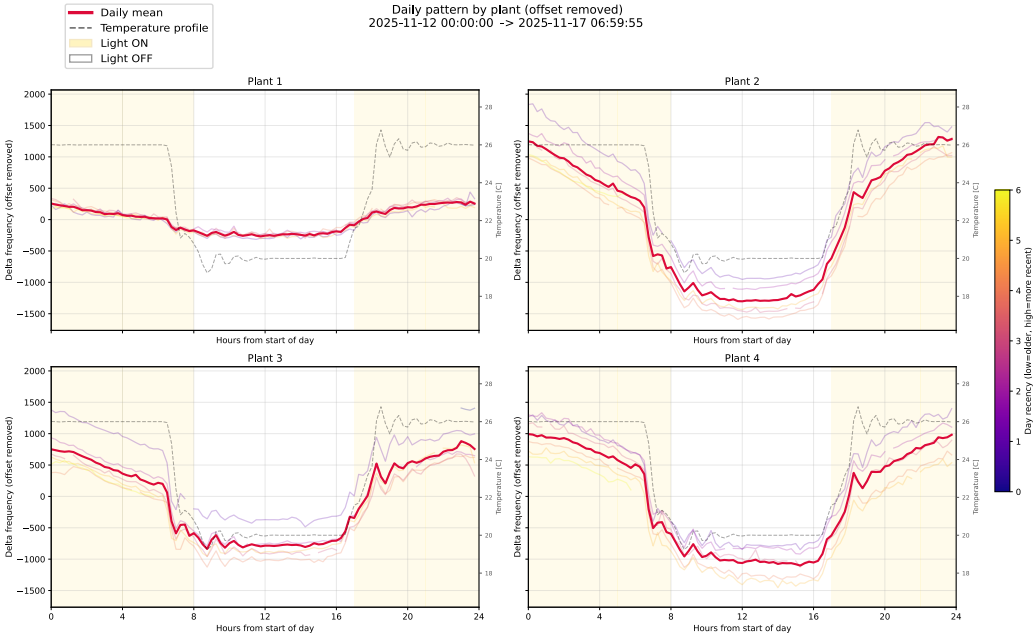


Fig. 4.19 Data from 2nd experimental period. Offset removed. Yellow background indicates light on, white background indicates light off. Different color curves distinguish older and recent days. Dashed line indicates the temperature profile

During the second experimental period, light intensity was reduced to 50% of the maximum output, while the photoperiod and temperature profile remained unchanged. The objective of this phase was to evaluate whether a reduction in incident light intensity would result in measurable changes in stem frequency.

As shown in Figure 4.19 and quantified in Table 4.3, the overall coupling between environmental forcing and stem frequency remains strong. Peak timings exhibit only minor shifts, occurring between 23:00 (Plants 2 and 3) and 00:00 (Plant 4). High correlation coefficients persist for both temperature ($T_{\text{corr}} \in [0.93, 0.97]$) and light ($L_{\text{corr}} \in [0.92, 0.95]$).

Reducing daytime light intensity induced a slight increase in daily excursion for most specimens. Plant 1's amplitude rose from 509 Hz (3.9%) to 553 Hz (4.3%), Plant 2 increased from 2278 Hz (9.6%) to 2620 Hz (11.6%, with variance rising to 979),

and Plant 3 increased from 1548 Hz (7.9%) to 1718 Hz (8.8%). Plant 4 was the sole exception, exhibiting a mild drop from 2252 Hz (10.0%) to 2095 Hz (9.4%).

Period 3

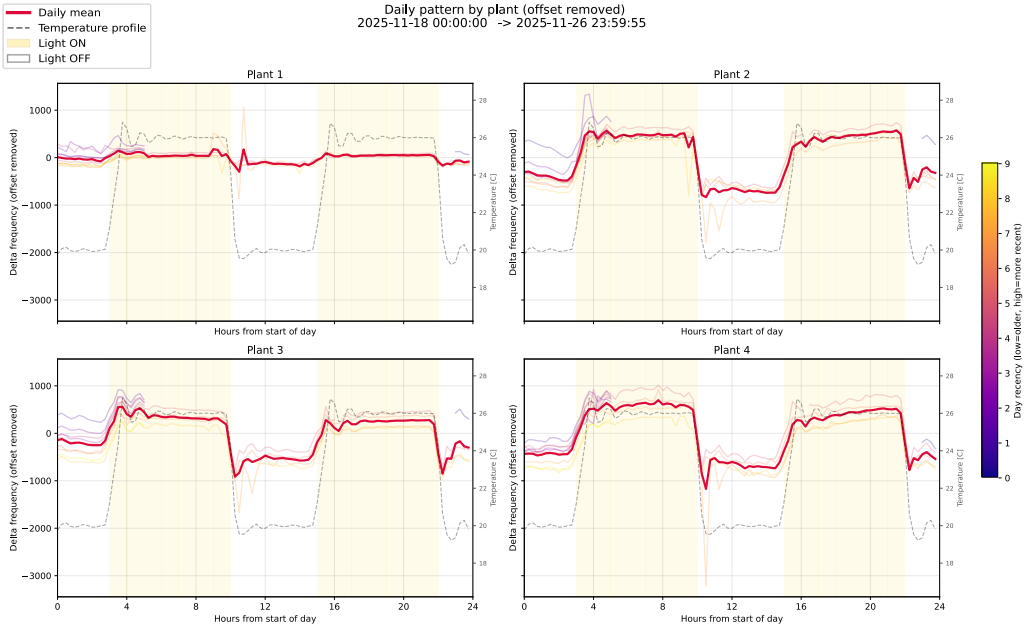


Fig. 4.20 Data from 3rd experimental period. Offset removed. Yellow background indicates light on, white background indicates light off. Different color curves distinguish older and recent days. Dashed line indicates the temperature profile.

In Period 3, the photoperiod was modified while maintaining the same daytime light intensity (50%) and temperature oscillation as in the previous periods. The corresponding measurements are reported in Figure 4.20.

Metrics in Table 4.3 reveal a generalized drop in signal amplitude and variance across all plants under this compressed photoperiod. Compared to Period 2, Plant 1's daily amplitude decreased to 478 Hz (3.7% relative variation, variance 92), Plant 2 dropped to 1409 Hz (6.4%, variance 501), Plant 3 fell to 1475 Hz (7.8%, variance 385), and Plant 4 decreased to 1871 Hz (8.7%, variance 532).

Peak timings shifted markedly to accommodate the faster cycle, occurring at 09:00 for Plant 1, 21:30 for Plant 2, 03:45 for Plant 3, and 07:45 for Plant 4. Temperature and light correlations remained high for Plants 2 and 4 ($T_{\text{corr}} = 0.96$, $L_{\text{corr}} = 0.92$), whereas Plants 1 and 3 exhibited a moderate decline (T_{corr} of 0.76 and 0.88; L_{corr} of

0.73 and 0.84). Combined with a visible decreasing long-term trend (Figure 4.20), these quantitative changes point toward progressive plant adaptation or the initial onset of physiological stress.

Period 4

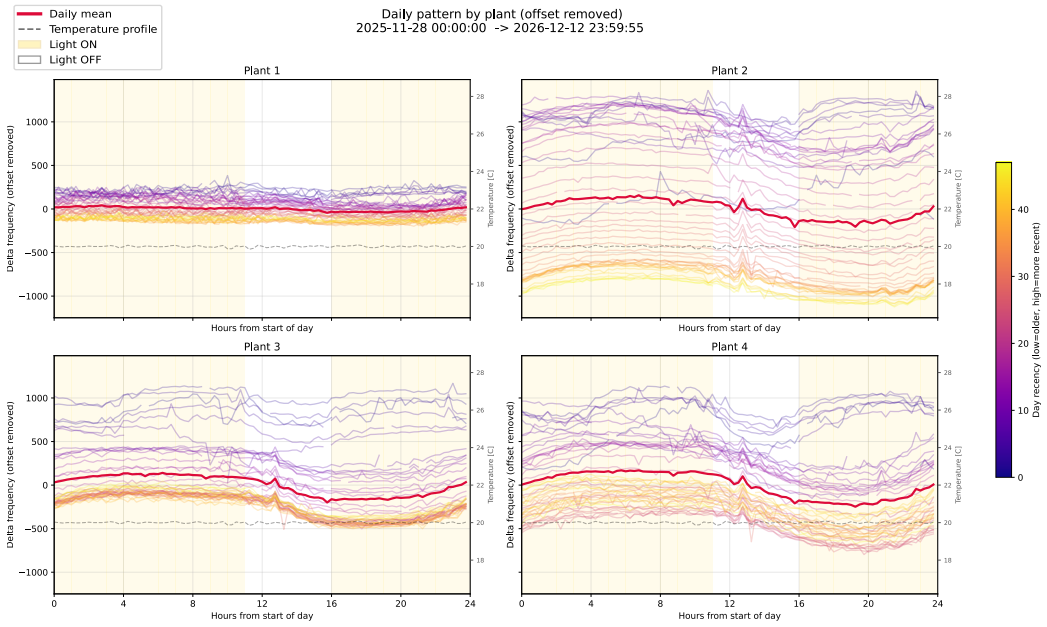


Fig. 4.21 Data from 4th experimental period. Offset removed. Yellow background indicates light on, white background indicates light off. Different color curves distinguish older and recent days. Dashed line indicates the temperature profile.

During Period 4, the objective was to isolate the effect of light variation by maintaining a constant temperature of 20 °C throughout the entire cycle.

As shown in Figure 4.21 and by the metrics reported in Table 4.3, the daily behavior differs significantly from the previous periods. Eliminating daily temperature oscillations leads to a marked reduction in the stem frequency response across all monitored specimens. In Period 1, daily amplitudes reached up to 2278 Hz (10.0% relative variation for Plant 4 and 9.6% for Plant 2), whereas in Period 4 the maximum observed amplitude drops to 418 Hz (2.0% relative variation for Plant 4).

This attenuation is also clear in the signal variance, which ranges from 181–897 in Period 1 down to 23–148 in Period 4. Furthermore, while stem frequency showed a strong correlation with light during Periods 1 and 2 ($L_{\text{corr}} \geq 0.92$), holding tempera-

ture constant weakens this correlation significantly in Period 4, yielding values of 0.16 for Plant 1, 0.30 for Plant 2, 0.35 for Plant 3, and 0.29 for Plant 4.

A subtle residual daily pattern remains visible in Plants 2, 3, and 4, which maintain modest daily amplitudes of 366 Hz, 340 Hz, and 418 Hz respectively, assuming a smoother, more sinusoidal shape. In contrast, Plant 1 exhibits almost no detectable daily variation, recording a minimal daily amplitude of 85 Hz (0.7% relative variation) and a variance of 23.

Summary

The analysis conducted across the four experimental periods highlights a clear and consistent relationship between stem frequency dynamics and the environmental conditions imposed within the climate chamber. In particular, temperature emerges as the dominant driver of the observed variations. In Periods 1 and 2, where temperature and light vary synchronously, stem frequency closely follows the imposed profiles, showing strong correlations and consistent peak timing across plants. The reduction of light intensity in Period 2 does not significantly alter the overall behavior, although a slight increase in daily amplitude suggests a possible compensatory physiological response.

When the photoperiod is modified in Period 3, the coupling with temperature remains evident, but a general reduction in signal amplitude and the appearance of a decreasing trend indicate potential adaptation or the onset of stress conditions. This behavior becomes more pronounced in Period 4, where temperature is held constant. In this case, the stem frequency response is strongly attenuated, confirming that light alone induces only a limited physiological response compared to temperature-driven effects.

Additionally, inter-plant variability plays a significant role. Plants with lower baseline stem frequency tend to exhibit reduced daily amplitudes, suggesting a link between baseline physiological state and responsiveness to environmental forcing. Toward the final stages of the experiment, a general decline in stem frequency is observed across all plants, consistent with the visual appearance of stress symptoms.

To support these observations, a set of quantitative metrics was extracted from the mean daily profiles, including daily amplitude, relative variation, peak timing, variance, and correlation with environmental variables. These results are summarized

in Table 4.3 provides a compact overview of plant-specific behavior across the different experimental periods. A substantial dependence of stem frequency on both temperature and light can be observed during Periods 1 and 2. These two periods differ primarily in terms of the light intensity applied during the daytime phase, while the temperature profile and relative humidity were kept unchanged. Despite the combined effect of temperature and light variations, the correlation coefficients remain relatively stable between the two periods. This suggests that, within the tested experimental conditions, stem frequency may be more strongly associated with temperature than with light intensity.

Considering again Periods 1 and 2, but focusing on the daily amplitude of stem frequency variations, the behavior of all plants appears to be relatively consistent across the two periods, apart from minor differences. A different behavior is observed in Period 3, in which the duration of the day night cycle was reduced to 12 hours, with 6 hours of light and 6 hours of darkness. Under these conditions, the amplitude of the stem frequency oscillations decreased for all plants. The correlations with temperature and light, however, remained relatively stable for Plants 2 and 4, while they decreased more noticeably for Plants 1 and 3, although they remained significant.

In Period 4, the experimental conditions were further modified by maintaining temperature at a constant level. The resulting behavior was markedly different: stem frequency variations were substantially reduced, while the correlation with changes in light intensity was also very weak. Taken together, these observations suggest that, under the investigated conditions, air temperature represents the main environmental driver of stem frequency variations, whereas changes in light intensity alone appear to have a comparatively limited effect.

Overall, these preliminary experiments indicate that stem frequency measurements can capture meaningful physiological dynamics and are strongly influenced by environmental conditions, particularly air temperature. This suggests that stem electrical properties may represent a promising proxy for monitoring plant activity and stress. However, further investigation is required, particularly given the limited number of plants considered in these experiments, which restricts the statistical significance and generalizability of the observed results. Moreover, additional experiments are needed to disentangle the overlapping effects of environmental variables and to validate the observed relationships using independent physiological measurements.

Table 4.3 Summary of daily metrics for each plant across experimental periods (offset removed data).

Period	Plant	Day Ampl.	Day Rel (%)	Peak Hour	Variance	T corr	L corr
P1	1	509	3.9	22:45	181	0.95	0.95
P1	2	2278	9.6	00:45	897	0.98	0.98
P1	3	1548	7.9	22:15	581	0.96	0.96
P1	4	2252	10.0	00:45	850	0.97	0.97
P2	1	553	4.3	23:30	196	0.93	0.92
P2	2	2620	11.6	23:00	979	0.96	0.94
P2	3	1718	8.8	23:00	624	0.96	0.94
P2	4	2095	9.4	00:00	811	0.97	0.95
P3	1	478	3.7	09:00	92	0.76	0.73
P3	2	1409	6.4	21:30	501	0.96	0.92
P3	3	1475	7.8	03:45	385	0.88	0.84
P3	4	1871	8.7	07:45	532	0.96	0.92
P4	1	85	0.7	02:45	23	–	0.16
P4	2	366	1.7	06:45	113	–	0.30
P4	3	340	1.9	06:15	115	–	0.35
P4	4	418	2.0	06:45	148	–	0.29

4.4.2 Relationship between Stem Frequency and Leaf Area

During the experiment, as briefly mentioned in the experimental setup, it was possible to automatically acquire a series of images to monitor and analyze the condition of the plants. For this reason, these images were used to estimate the leaf area of the tomato plants inside the climate chamber and to compare this information with the stem frequency measurements.

Automatic Plant Segmentation and Leaf Area Calculation

In order to estimate leaf area throughout the experimental period without requiring manual intervention for each measurement, an automated approach was adopted. The camera setup shown in Figure 3.6 enabled periodic image acquisition. A sampling interval of 3 hours was selected as a trade-off between storage requirements and the expected rate of change in plant appearance.

The monitored environment was not sufficiently static to allow reliable segmentation based solely on geometric assumptions, such as fixed pot positions within the

frame. Additionally, the presence of several interfering elements, such as cables (including green ones) and artificial lighting components, made simple color based thresholding approaches ineffective. Furthermore, since plants were monitored throughout their growth, predefined geometric constraints could become invalid over time, compromising the segmentation process.

For these reasons, a pre-trained YOLO model was employed, combined with a simple tracking strategy to consistently identify the same plant across consecutive images. Specifically, YOLO [49, 50] was used to detect and localize the regions containing each plant. The corresponding image regions were then cropped and processed individually.

For each cropped image, a color-based filtering step was applied to isolate green regions corresponding to healthy plant tissue. Unhealthy areas were excluded through thresholding and therefore not included in the final estimation of leaf area.

Image Labeling and Dataset Creation

The first step consisted of labeling images acquired from the experimental setup in order to fine-tune the model. To this end, an online computer vision tool, Roboflow [51], was used due to its convenient interface for image annotation and its capability to export labeled datasets in YOLO format.

A set of images was collected under different conditions, including variations in viewing angles and the presence or absence of plants, to ensure sufficient variability for the network fine tuning process. Roboflow provides a graphical interface that allows objects to be annotated directly within each image. It also supports exporting the dataset in the required YOLO format and performing data augmentation operations such as rotations, blurring, scaling, and flipping.

In the presented work, data augmentation was applied to increase the variability of the dataset by generating three additional versions of each source image. The applied transformations included:

- Random cropping between 0% and 20% of the image area,
- Random rotation within the range of $[-15^\circ, +15^\circ]$,

- Random Gaussian blur [52] with a kernel corresponding to a standard deviation between 0 and 2.5 pixels.

An example of a labeled image is shown in Figure 4.22, where the annotated plant contours used for training the model are highlighted. In total, 36 images were collected prior to data augmentation, including some images without plants to improve the model's ability to detect their absence. The dataset was then split into training, validation, and test sets (19 training, 7 validation, and 10 test images).

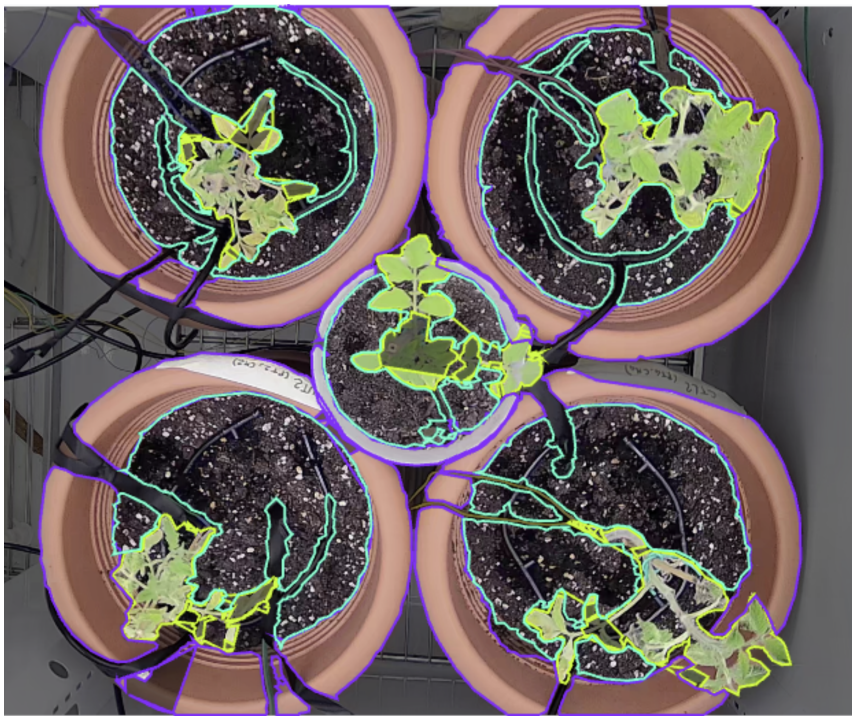


Fig. 4.22 Example of a climatic chamber labeled image during experiment. The plant in the center was put only for testing purposes, no stem frequency was acquired from it.

Fine Tuning-Training

Once the dataset was prepared, the model training phase was carried out by fine-tuning a pre-trained YOLO network on the collected data. The training process was executed using the Ultralytics YOLO framework [50] based on PyTorch [53]. The training was performed on the GPU of a notebook equipped with the following hardware:

- *Intel Core i9-13900H* CPU (13th generation, 2.60 GHz)

- *32 GB* of RAM
- Graphic card NVIDIA *GeForce RTX4060*

The model was initialized with pre-trained weights and adapted to the specific experimental setup through fine tuning with the hyperparameters presented in table 4.4.

Table 4.4 Training hyperparameters used for the YOLO model.

Hyperparameter	**Value**
Image size	1024 pixels
Epochs	100
Batch size	8
Early stopping patience	20 epochs
Learning rate	0.01
Optimizer	AdamW [54]
LR schedule	Cosine decay
Other parameters	Default YOLO

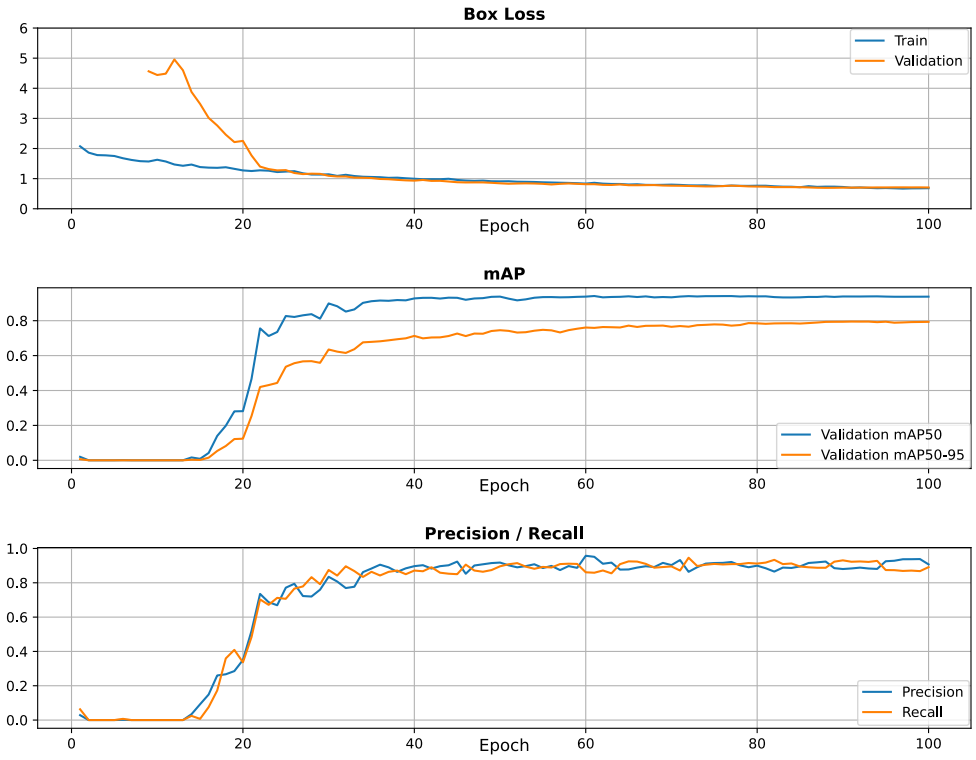


Fig. 4.23 Overview of training metrics

Figure 4.23 summarizes the results of the fine tuning process reporting the loss of the bounding boxs, the mean Average Precision (mAP) and precision and recall. As shown in the figure, the model accurately detects the presence and location of the tomato plants.

Leaf Tracking and Area Estimation Algorithm

After the fine-tuning phase, the model was used to process all images acquired during the experiment. Specifically, the trained model was employed to identify and localize the regions of the image where plants were present. The detected bounding boxes were then used to crop the corresponding image regions. An example of this process is shown in Figure 4.24, where one of the detected plants is highlighted.



Fig. 4.24 Example of plant detection and bounding box extraction.

As can be observed in Figure 4.24, the green portion of the plant is correctly identified. However, the cropped region still includes background elements that do not belong to the plant, leading to an overestimation of the leaf area.

To address this issue, the cropped images were transformed from the standard RGB color space to the CIELAB (L*a*b*) color space. In the RGB representation, each pixel is described as a combination of red, green, and blue components. However, the same perceived color can correspond to significantly different RGB values depending on illumination conditions, making this representation less accurate.

The CIELAB color space provides a perceptually uniform representation of color, where:

- L^* represents *lightness*,
- a^* represents the *green–red* component,
- b^* represents the *blue–yellow* component.

A schematic representation of this color space is shown in Figure 4.25.

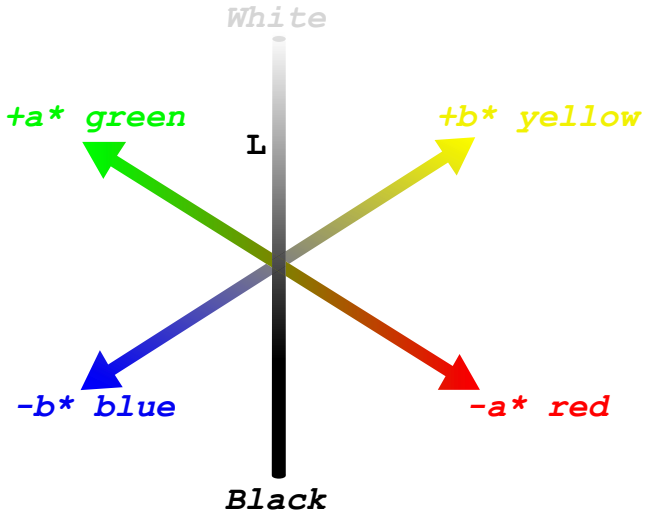


Fig. 4.25 CIELAB color space representation.

Selecting a specific channel of the color space, makes it possible to isolate particular color characteristics. In this case, the analysis focuses on the a^* channel, which allows the identification of green regions of the plant. At this point, by applying a threshold to the a^* values of each pixel, it is possible to distinguish pixels corresponding to a plant from the background.

This transformation was performed using existing Python libraries. In this work, the *PlantCV* [55] library was used, specifically the `rgb2gray_lab` function. This function converts an RGB image and extracts a selected LAB channel (in this case a^*) as a grayscale image, which can then be used for a simple threshold based segmentation of the plant. The result of this processing is shown in figure 4.26.

As can be observed in the left image, the cropped region still contains elements that do not belong to the plant, such as portions of soil and the pot. After transforming



Fig. 4.26 RGB segmented plant (left) and corresponding image after color thresholding

the image into the CIELAB color space and applying thresholding, the segmentation becomes significantly more accurate, isolating only the green regions of the plant, which are associated with photosynthetically active areas.

Once the segmented image is obtained, it becomes possible to estimate the plant area in terms of pixels. Specifically, the number of white pixels resulting from the thresholding operation is computed and normalized with respect to the total image size.

Therefore, for each plant and for each timestamp at which an image is acquired, the relative leaf area is estimated as:

$$Area_{rel} = \frac{\#\text{ white pixels}}{img_{height} \cdot img_{width}} \tag{4.7}$$

During image processing, each detected plant instance must be consistently tracked across successive images. To achieve this, a spatial ID consistent with the one presented in previous section (plants 1,2,3 and 4) is assigned to each detected plant, which is then matched across frames based on its spatial proximity to previously assigned positions.

A complete overview of the algorithm used for leaf area estimation is provided in Algorithm 1.

Algorithm 1 Leaf Area Estimation from Image Segmentation

Require: Image set $\mathscr{I}$, trained YOLO model

Ensure: Leaf area per plant and timestamp

for each image $I \in \mathscr{I}$ **do**
    Extract timestamp t from filename
    Run YOLO model to obtain bounding boxes, confidences, and masks
    Filter detections with confidence $< \tau_{conf}$
    if multiple overlapping boxes exist **then**
        Merge boxes using Intersection over Union (IoU) threshold τ_{iou}
    end if
    Assign spatial IDs to detected plants
    for each detected plant p **do**
        Extract bounding box and corresponding mask
        Resize mask to image resolution
        Crop image and mask to bounding box region
        Apply mask to isolate plant region
        Convert masked image to grayscale (LAB space, channel a)
        Apply binary threshold to segment plant pixels
        Compute plant area:

$$A_p = \frac{\text{number of foreground pixels}}{\text{total image pixels}}$$

        Store (t, p, A_p) in output dataset
        Save visualization (masked image + thresholded image)
    end for
end for
Export results

The resulting estimation of the leaf area is reported in the top panel of Figure 4.27.

The middle and bottom panels show the normalized and raw stem frequency measurements, respectively.

It can be observed that, during the experimental period analyzed in this chapter, the plants progressively entered a stress condition. This is clearly reflected by the reduction in the estimated leaf area over time.

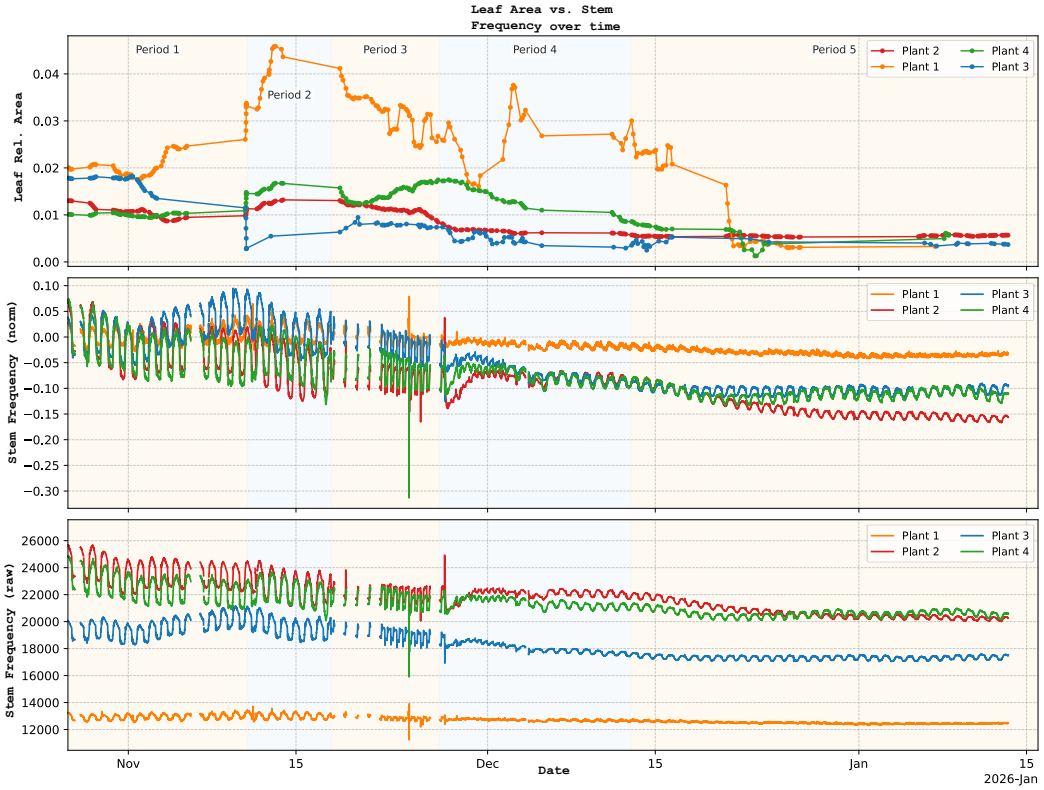


Fig. 4.27 Leaf area estimation (top), normalized stem frequency (middle), and raw stem frequency (bottom) over the experimental period.

Short-term variations in stem frequency have already been discussed in the previous section. However, when considering the long-term trend, a gradual decrease can be observed, suggesting a reduction in stem conductivity. This behavior appears to be related to the leaf area dynamics in tomato plants and, more generally, to their physiological state. All plants exhibited a negative response to the imposed experimental conditions. This is also qualitatively visible in Figure 4.28, where the plants, compared to their initial state, show progressive yellowing and a reduction in leaf biomass.

In the initial phase of the experiment, the leaf area remained approximately constant or showed a slight increase (e.g., Plant 1 around mid-November). This was followed by a phase of stabilization or mild reduction from mid-November to early December, with the exception of Plant 1, which exhibited a more pronounced decrease. A more critical phase began around mid-December, after which all plants showed a consistent decline in leaf area. By the end of the experiment, the green leaf area

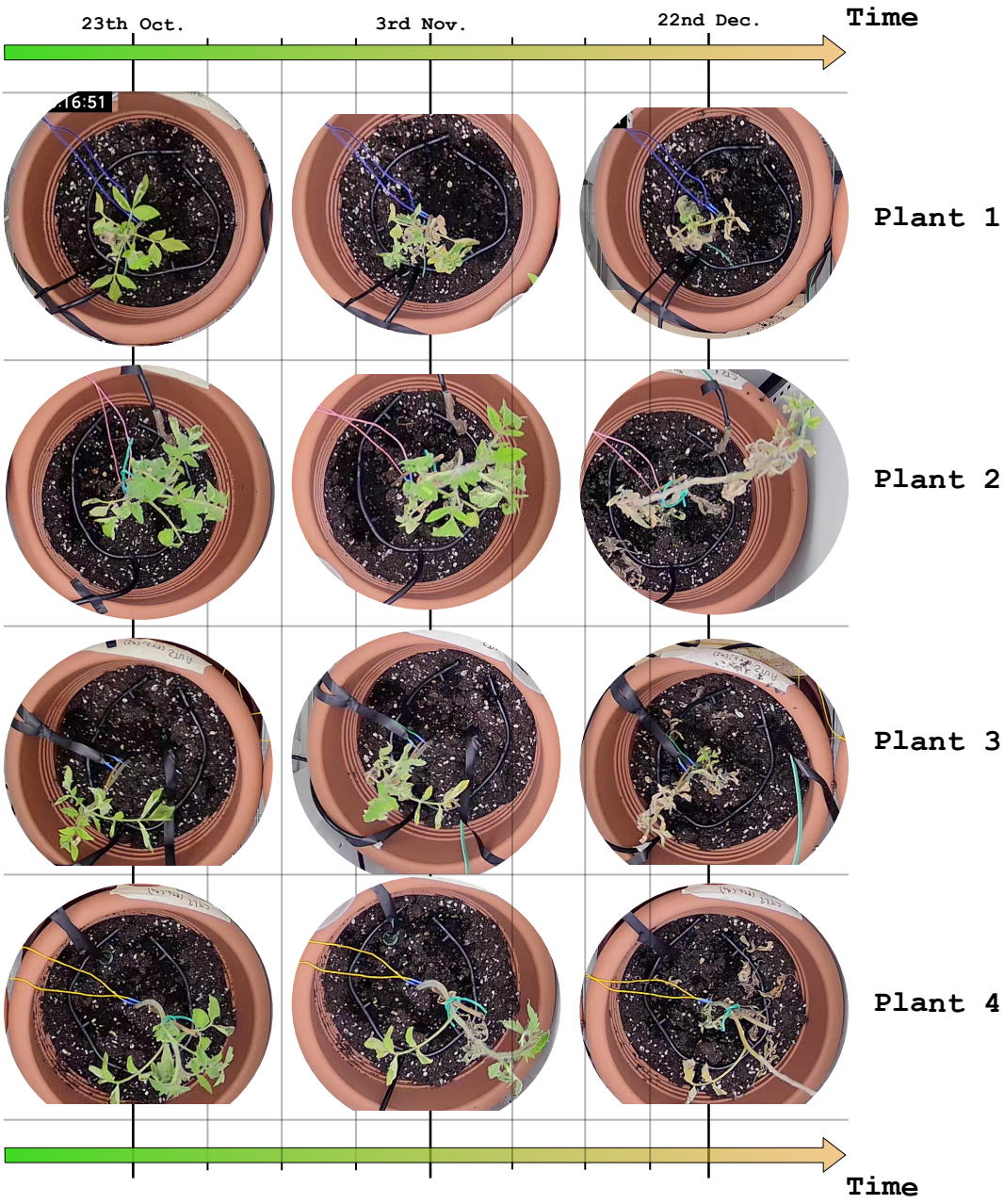


Fig. 4.28 Visual evolution of plant conditions during the experiment.

was almost completely depleted, indicating severe stress conditions and likely plant death.

The raw stem frequency measurements (bottom panel) highlight the presence of different baseline levels across plants, which are not directly comparable in terms of plant health. Each plant exhibits its own characteristic baseline around which

the signal fluctuates. For this reason, the normalized stem frequency (middle panel) provides a more meaningful representation. Before the onset of stress, the normalized signal remains relatively stable or shows a slight increase. As stress becomes more pronounced, consistently with the observed reduction in leaf area, the stem frequency exhibits a decreasing trend. This behavior suggests a reduction in stem hydration and transport activity, despite the fact that soil water conditions were maintained at optimal levels throughout the experiment.

Summary

The analysis presented in this section integrated image based monitoring with stem frequency measurements to gain insight into plant physiological dynamics over time. An automated pipeline was developed to estimate leaf area from images acquired during the experiment. The combination of a fine-tuned YOLO model for plant detection and a color-based segmentation approach in the CIELAB space enabled the identification of plant regions. This approach allowed the extraction of a consistent proxy of green leaf area without manual intervention. The estimated leaf area time series reveal a clear long-term trend across all plants. After an initial phase characterized by stability or slight growth, a progressive decline in leaf area is observed, ultimately leading to a near-complete loss of green biomass. This behavior is consistent with the visual assessment of plant conditions and indicates the onset and progression of severe stress. When compared with stem frequency measurements, a coherent relationship emerges. While short-term dynamics are primarily driven by environmental forcing, the long-term evolution of the normalized stem frequency shows a decreasing trend that closely follows the reduction in leaf area. This suggests that stem frequency is sensitive not only to external environmental conditions but also to the internal physiological state of the plant. Importantly, the normalization of stem frequency proves essential to enable meaningful comparisons across plants, as raw signals are characterized by plant-specific baselines. Once normalized, the signal reveals a consistent behavior across all specimens, highlighting a gradual reduction in stem conductivity likely associated with decreased hydration and transport activity.

Chapter 5

Greenhouse Experiments

5.1 Introduction

This chapter presents a series of experiments conducted in collaboration with the University of Turin, Department of Agricultural and Forest Sciences, under the supervision of Professor Massimo Pugliese and in cooperation with the agronomist Luca Alfarano.

In the previous section, preliminary analyses were presented to investigate the behavior of electrical impedance measurements of the plant stem, primarily in tomato plants, using the stem frequency technique.

Overall, it was observed that this variable responds to plant stress, particularly water-related stress. Up to this point, the stress conditions affecting the plants can be categorized as abiotic, i.e., caused by non-living factors such as heat stress or water deficit.

In this chapter, several experiments on tomato plants are presented with the objective of detecting the onset of stress in a timely manner and, additionally, distinguishing between abiotic and biotic stress conditions.

This chapter also marks the beginning of a new experimental phase. The analysis moves from a fully controlled environment, such as climate chambers, to a still controlled but less constrained setting, namely a greenhouse. This transition represents a more realistic scenario, bringing the experimental conditions closer to those encountered in practical agricultural applications.

The content presented in this chapter has been adapted for this thesis from previously published work [30, 56], with the permission of all the authors involved, and has been further extended.

5.2 Tomato stress analysis

This section summarizes two years of experiments and data collected during the PhD research presented in this dissertation. The hardware setup is the same as described in the previous chapters, where the primary variable of interest is the *stem frequency*. However, as in earlier experiments, environmental conditions were also continuously monitored. In particular:

- *Air Temperature* (°C) and *Relative Humidity* (%) were measured using an HDC2080 sensor manufactured by Texas Instruments [57]
- *Soil Water Potential* (kPa) was measured using the *Watermark* sensor [4], with the setup described in Section 3.2.2
- Differently from previous experiments, light intensity was not measured in this experimental campaign

All experiments were conducted in a greenhouse facility of Department of Agricultural Forest and Food Sciences (*DISAFA*), University of Turin. The experimental structure remained consistent across all iterations. Plants were divided into three distinct experimental groups (see Figure 5.1):

1. *Control group*: regular irrigation, no fungal infection
2. *Drought group*: water stress, no fungal infection
3. *Fusarium group*: regular irrigation, artificial infection with *Fusarium* fungus

The control and Fusarium groups were maintained under the same irrigation conditions, namely optimal water availability. Irrigation was performed by filling the saucer beneath each pot and ensuring that it never remained empty, thus maintaining a consistent and sufficient water supply.

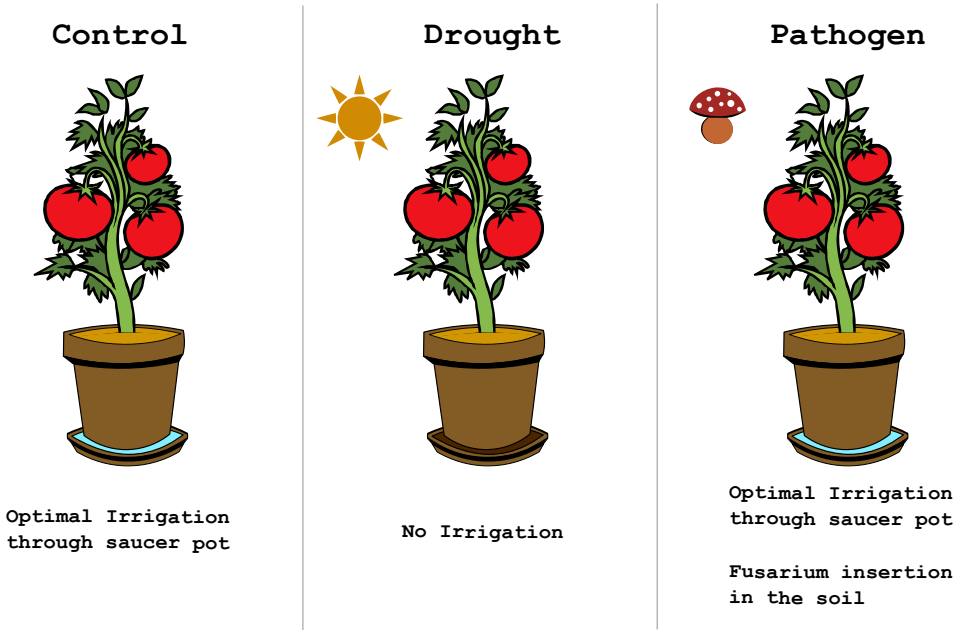


Fig. 5.1 Experimental setup with the three plant groups

In contrast, plants in the drought group received only a small amount of water directly into the soil at the time of transplanting from the seedling tray. After this initial irrigation, the saucer was not refilled, allowing the plants to gradually experience water deprivation over time. Table 5.1 illustrates the distribution of the plants across the different experimental blocks and treatment groups.

Table 5.1 Distribution of tomato plants across experimental blocks and treatment groups.

Experimental Block	Control	Drought	Fusarium	Total
Block 0	4	4	3	11
Block 1	5	3	4	14
Block 2	5	1	2	7
Block 3	5	4	4	13
Block 4	5	4	5	14
Block 5	5	3	5	13
Total	**29**	**18**	**23**	**73**

The plants were grown in pots with approximate dimensions of 14 cm in height, 12 cm in width, and 12 cm in depth, corresponding to a substrate volume of approximately 1.1–1.2 L.

At the time of every sensor installation, the tomato plants were approximately two weeks old, making them sufficiently developed to allow electrode insertion into the

stem. The electrodes were placed at a distance of 2 cm from each other. Further details on the relationship between stem frequency and electrode spacing can be found in [3].



Fig. 5.2 Example of needle insertion for stem frequency measurement.

As previously mentioned, multiple experimental iterations were conducted, and different data collection were performed across these iterations. During each of them every plant was monitored visually daily and the date onset of symptoms was annotated. Considering all experiments, a total of *73 plants* were monitored. The approaches presented in this section are derived from works published by the author of this dissertation, with the consent of the other authors [30, 56].

5.2.1 Different baseline measurements

As discussed in previous chapters, multiple factors influence stem frequency measurements, and therefore the electrical conductivity of the stem. Among these factors,

plant physiology plays a significant role. Since plants are living organisms, it is reasonable to expect substantial variability in stem frequency measurements even under similar environmental conditions when comparing different individuals.

One of the most immediate sources of variability is related to structural differences between plants, such as the initial stem diameter at the time of measurement. A larger stem cross-section can result in higher conductivity, similarly to how a thicker electrical wire exhibits lower resistance.

More generally, this variability can be interpreted as an intrinsic biological heterogeneity, comparable to differences observed in physiological signals in humans, such as heart rate or baseline cardiovascular activity, which vary naturally between individuals even under comparable conditions. For this reason, a preliminary boxplot of the baseline distributions across the experimental groups is reported in Figure 5.3, considering measurements collected during the first week of the experiment. As in the previous analyses, this baseline will be used for the normalization of subsequent measurements.

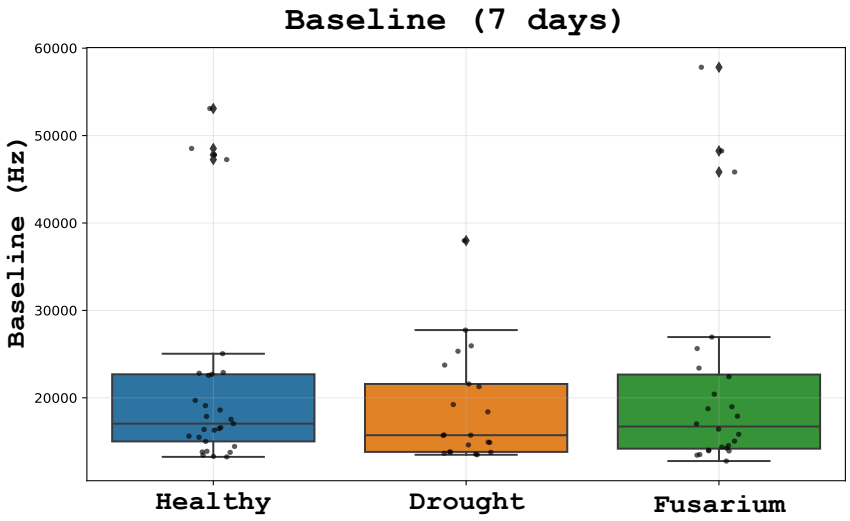


Fig. 5.3 Boxplot of stem frequency baseline distribution for each experimental group

As shown in Figure 5.3, no significant differences can be observed between the distributions of the experimental groups during the first week. In particular, no clear separation emerges as a function of group assignment. However, a non-negligible inter-plant variability is evident, with the main range of values approximately spanning from 15 kHz to 25 kHz.

5.2.2 Long Term Analysis

In the previous chapters, the relationship between stem frequency measurements and changes in environmental variables was discussed, with particular emphasis on short-term effects, such as sudden variations in temperature or relative humidity.

In the present experimental setup, all plants were exposed to the same environmental conditions, as they were located within the same greenhouse. Although some spatial gradients in environmental variables were present, it is reasonable to assume that their effects were, on average, comparable across all monitored plants.

The analysis initially focuses on longer-term effects on plant behavior. To this end, a daily stem frequency value was computed for each plant. The sensor sampling interval was set to one measurement every *10 minutes* (i.e., *144* measurements per day), and the daily value was defined as the average of these measurements.

Across all experimental iterations, a total of 73 plants were monitored. Considering the daily aggregation, this resulted in an overall dataset comprising 2429 daily observations across all plants.

In Figure 5.4, the temporal evolution of stem frequency measurements is summarized for each experimental group. The time axis is expressed in days from the beginning of the experiment, and both raw and normalized (scaled) measurements are reported for completeness. For each day, measurements from all plants within the same experimental group are aggregated by computing the daily mean stem frequency. The shaded regions represent the 95% confidence interval computed across plants within each group. The top panel reports the evolution of the raw stem frequency values, highlighting absolute changes in signal magnitude over time. The bottom panel shows the same trajectories after normalization, allowing for a clearer comparison of relative temporal dynamics across experimental conditions.

It can be observed that the most pronounced differences between experimental conditions appear in both representations, particularly for the drought stress group. Plants subjected to water limitation exhibit a clearly distinct temporal behavior in stem frequency compared to the other conditions. In particular, in the normalized representation (bottom panel), drought-stressed plants initially show an increase in stem frequency during the early stages of the experiment. However, as the experiment progresses and water stress intensifies, this group exhibits a marked decrease in stem frequency values relative to the control conditions.

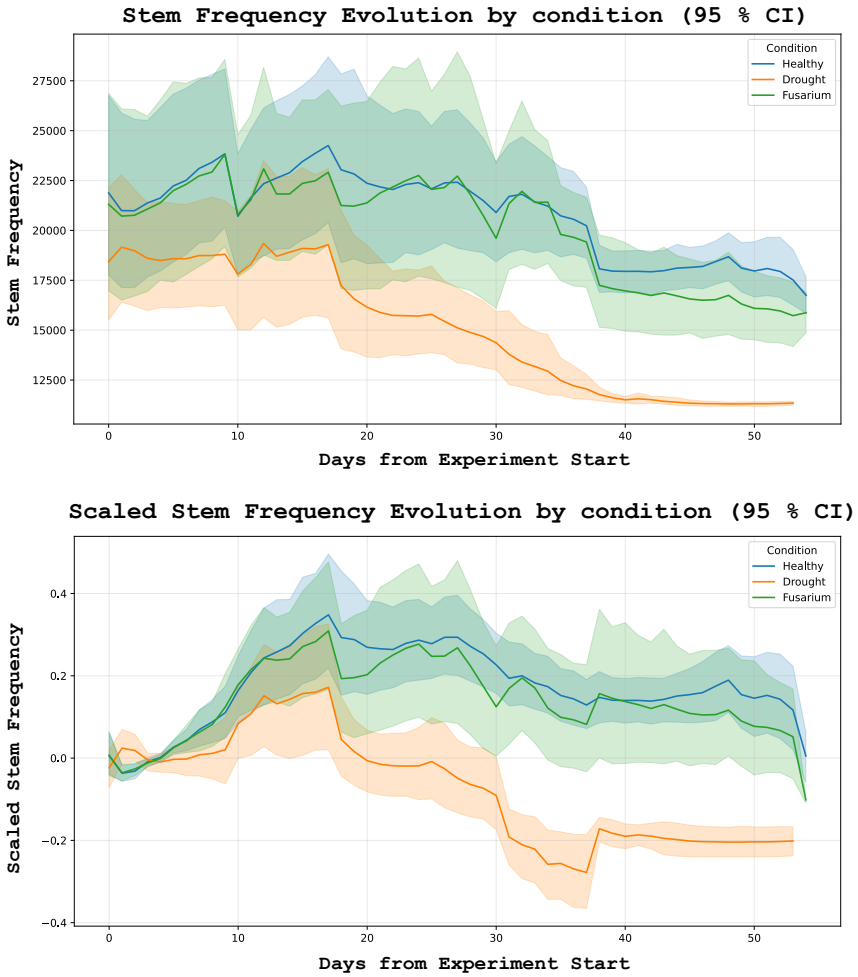


Fig. 5.4 Evolution of raw daily stem frequency (top panel) and normalized daily stem frequency (bottom panel) measurements for the 3 experimental groups

A lower stem frequency can be associated with reduced electrical conductivity of the stem, which is consistent with a lower water content in plant tissues due to limited water availability in the soil. It is also noteworthy that the initial positive variation observed in this group may be related to early stage plant growth; however, this growth appears to be progressively constrained by the intensification of water stress conditions.

Regarding the plants subjected to *Fusarium* infection, their behavior appears broadly similar to that of the control group, as can be observed in both plots. The main difference that can be inferred from Figure 5.4 is a higher variability in the measurements for the Fusarium group, as indicated by the wider 95% confidence intervals.

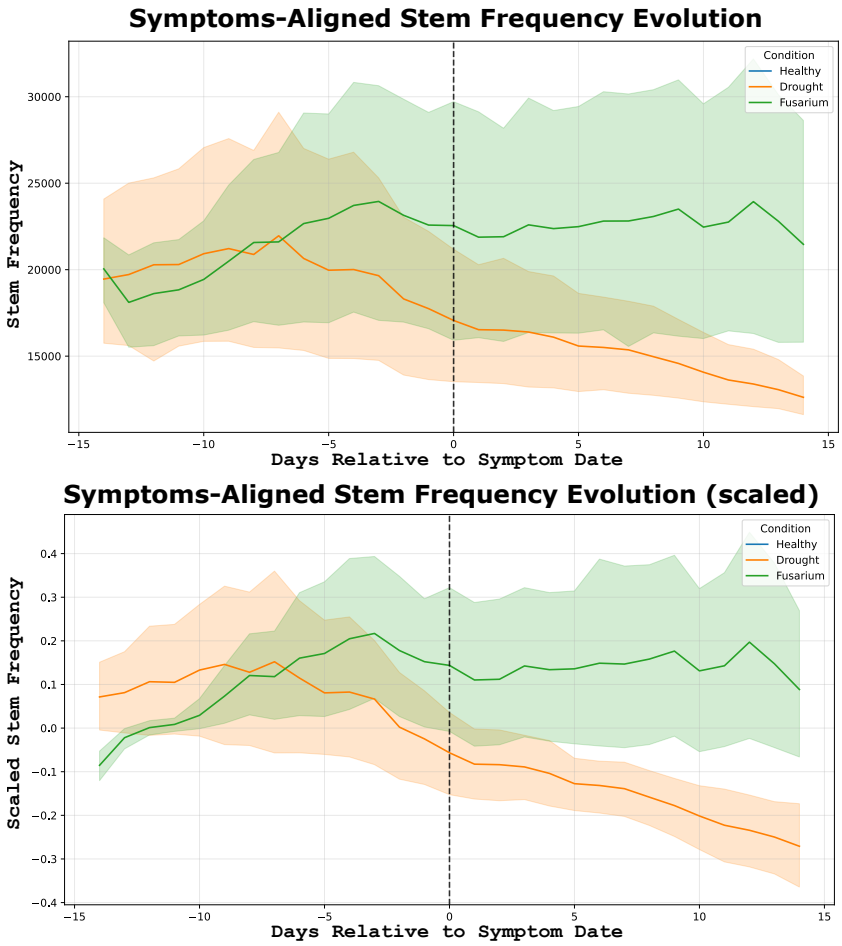


Fig. 5.5 Stem frequency evolution aligned to the onset of visible symptoms

It is also of interest to analyze the relationship between stem frequency measurements and the onset of visible symptoms. For each plant, the day corresponding to the first clear appearance of symptoms was annotated. The temporal evolution of stem frequency was then realigned using this reference point as a common origin for each plant. The resulting trends are reported in Figure 5.5 for plants belonging to the groups exhibiting symptoms.

Also in this case, a difference in behavior can be observed approximately one week before symptom appearance, particularly for drought- stressed plants, which show a substantial reduction in stem frequency. In contrast, plants affected by *Fusarium* do not exhibit similarly pronounced changes or reductions in the measured signal.

Mixed Effects Models Analysis and Autocorrelation Diagnostics

To better quantify the results presented in the figures, an analysis based on *Linear Mixed Effects Models* was adopted (a comprehensive review of this topic can be found in [58]). This choice was motivated by the fact that such models are particularly well suited for longitudinal studies, i.e., settings in which repeated measurements are collected from multiple experimental units (in this case, individual plants).

Using standard regression approaches would violate the assumption of independence between observations, as repeated measurements of the same variable (stem frequency, in this case) taken from the same plant at different time points cannot be considered independent. Mixed-effects models account for this hierarchical structure by combining fixed effects (such as experimental condition, time, and their interaction) with random effects associated with individual plants (e.g., differences in baseline stem frequency). Additionally, environmental variables shared across groups, such as temperature and relative humidity, can be included as covariates to control for potential confounding factors.

In general, the mathematical formulation of such models can be expressed as:

$$y = X\beta + Zb + \varepsilon \tag{5.1}$$

where:

1. y represents the observations
2. $X\beta$ represents the fixed effects
3. Zb represents the random effects
4. ε is the residual error term

with the following assumptions:

$$\mathbf{b} \sim \mathcal{N}(\mathbf{0}, \mathbf{G}), \qquad \varepsilon \sim \mathcal{N}(\mathbf{0}, \mathbf{R}), \qquad \mathbf{b} \perp \varepsilon. \tag{5.2}$$

Here, $\mathbf{G}$ is the covariance matrix describing the variability between experimental units (i.e., plants) and the potential interactions among random effects. $\mathbf{R}$ is the variance-covariance matrix of the residual errors, capturing the variability not explained by

the model. In particular, the assumptions require that the random effects have zero mean and covariance structure given by **G**, that the residuals have zero mean and covariance structure given by **R**, and that random effects and residual errors are mutually independent.

These concepts can also be expressed in scalar form as:

$$y_{ij} = \beta_0 + \sum_{p=1}^{P} \beta_p x_{p,ij} + b_{0i} + \sum_{q=1}^{Q} b_{q,i} z_{q,ij} + \varepsilon_{ij}. \tag{5.3}$$

where:

1. y_{ij} represents the stem frequency measurement for plant i at time j
2. $\beta_0 + \sum_{p=1}^{P} \beta_p x_{p,ij}$ corresponds to the fixed-effects component, i.e., the average behavior shared across all plants and explained by experimental conditions and covariates
3. b_{0i} is the plant-specific random intercept, accounting for differences in baseline stem frequency between plants
4. $\sum_{q=1}^{Q} b_{q,i} z_{q,ij}$ represents additional random effects that allow individual trajectories to vary over time (not considered in the present analysis)
5. ε_{ij} is the residual measurement noise

Summarizing, in the present analysis the stem frequency dynamics are modeled as:

$$\begin{aligned} \text{StemFreq}_{ij} = {} & \beta_0 + \beta_1 t_{ij} + \beta_2 \mathbf{1}(\text{Drought}_i) + \beta_3 \mathbf{1}(\text{Fusarium}_i) && (5.4) \\ & + \beta_4 t_{ij} \mathbf{1}(\text{Drought}_i) + \beta_5 t_{ij} \mathbf{1}(\text{Fusarium}_i) && (5.5) \\ & + \sum_{k=1}^{K} \gamma_k Z_{k,ij} + b_{0i} + \varepsilon_{ij}. && (5.6) \end{aligned}$$

where:

1. i denotes the plant and j the time index
2. t_{ij} represents the number of days from the beginning of the experiment

3. $\mathbf{1}(\text{Condition})$ is an indicator variable equal to 1 when the plant belongs to the specified experimental group

4. $Z_{k,ij}$ are environmental covariates (e.g., temperature and relative humidity)

Based on this formulation, both the slope and intercept of the regression model were estimated using mixed-effects models, thus explicitly accounting for the different sources of variability described above. The analysis was performed using the *statsmodels* library in Python, specifically the `mixedlm()` function [59]. The main results are summarized in the forest plots reported in Figure 5.6.

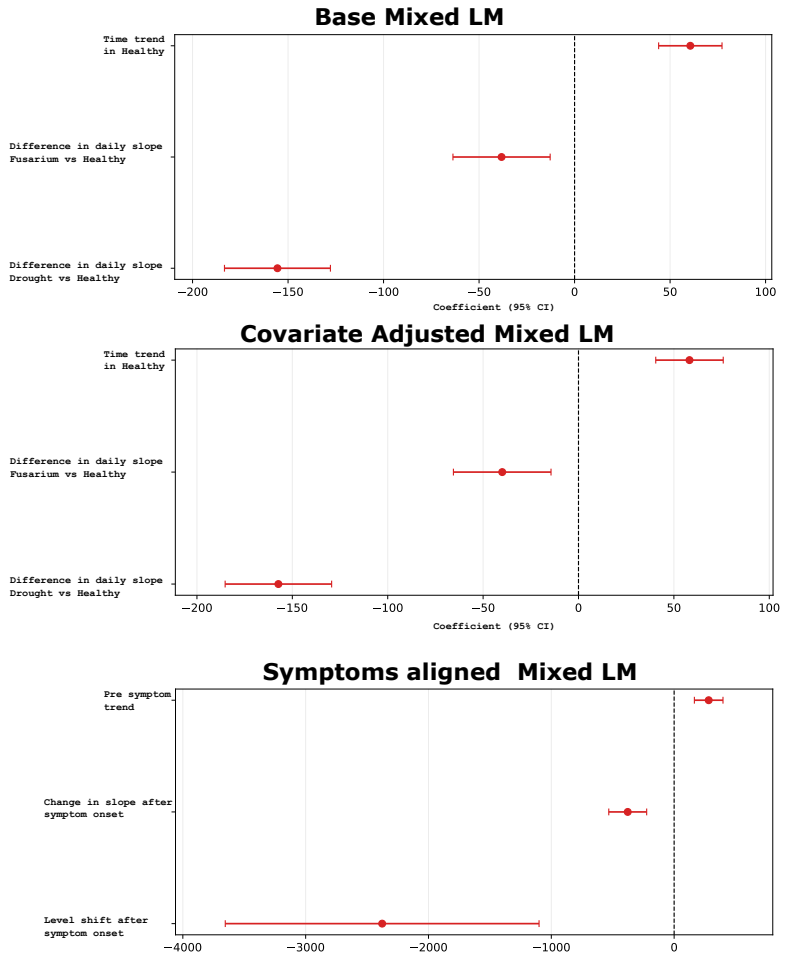


Fig. 5.6 Results of the mixed-effects linear models. Top panel: base model. Middle panel: covariate-adjusted model (RH, Temperature). Bottom panel: mixed model aligned pre- and post-symptom onset.

Figure 5.6 reports the estimated regression coefficients for the different experimental groups, providing insight into the temporal evolution of stem frequency during the experiment. In particular, the term *Time Trend in healthy* represents the slope of the long-term regression line for the reference group (control plants). This coefficient is positive (approximately 60), indicating that, under healthy conditions, stem frequency tends to increase over time relative to the beginning of the experiment.

The corresponding coefficients for the drought and *Fusarium* groups describe deviations from this baseline behavior. For the drought condition, the time trend is markedly negative, indicating a progressive decrease in stem frequency under water stress. This result is consistent with the expected physiological response of plants experiencing reduced water availability.

A similar, although less pronounced, negative trend is observed for the *Fusarium* group. While the magnitude of the effect is smaller compared to drought conditions, the overall behavior still suggests a gradual reduction in stem frequency over time.

Finally, particular attention should be given to the results shown in the bottom panel of Figure 5.6, where the analysis is aligned with respect to the onset of symptoms. It can be observed that the long-term trend, as estimated by the regression, changes significantly before and after symptom appearance, shifting from a moderately positive trend to a clearly negative one. This further supports the hypothesis that the onset of stress conditions, whether biotic or abiotic, leads to a reduction in stem frequency in tomato plants. A summary of all the statistics extracted from the mixed-effects model analysis is reported in Table 5.2. As a final remark, it is also possible to observe in Figure 5.6 how different plant health conditions systematically affect stem frequency measurements, resulting in an overall decreasing trend under stress conditions. This suggests that this relatively simple measurement technique, based on stem conductivity, is capable of discriminating between different plant health states.

Sensitivity Analysis: High-Resolution Autocorrelation and Residual Structure

The linear mixed-effects model presented in the previous section provides a baseline for understanding the average population level stem frequency behaviour across experimental conditions. However, the standard formulation relies on the assumption that the residual error terms are independent and identically distributed (IID). In this

Table 5.2 Summary of significant model results

Analysis	Term	Estimate	95% CI	p-value
Full-period MixedLM (base)	Baseline level (Healthy, day 0)	23662.202	[19859.090, 27465.315]	3.33e-34
Full-period MixedLM (base)	Difference in daily slope: Drought vs Healthy	-155.552	-183.287, -127.817]	4.16e-28
Full-period MixedLM (base)	Time trend in Healthy (per day)	60.601	[44.006, 77.196]	8.23e-3
Full-period MixedLM (base)	Difference in daily slope: Fusarium vs Healthy	-38.226	[-63.675, 12.777]	0.0032
Full-period MixedLM (covariate-adjusted)	Difference in daily slope: Drought vs Healthy	157.310	[-185.217, -129.403]	2.24e-28
Full-period MixedLM (covariate-adjusted)	Baseline level (Healthy, day 0)	25056.711	20592.805, 29520.617]	3.75e-28
Full-period MixedLM (covariate-adjusted)	Time trend in Healthy (per day)	58.182	[40.491, 5.873]	1.15e-10
Full-period MixedLM (covariate-adjusted)	Difference in daily slope: Fusarium vs Healthy	39.978	[-65.556, -14.400]	0.0022
Symptom-aligned MixedLM	Change in slope after symptom onset	-377.896	[-532.179, -223.614]	.58e-06
Symptom-aligned MixedLM	Pre-symptom daily trend	281.378	[164.965, 397.791]	2.17e-06 &
Symptom-aligned MixedLM	Level shift after symptom onset	-2377.115	[-3654.487, -1099.743]	.0003
Pre/Post delta Kruskal-Wallis	Post-pre delta (per plant)	4.923	–	0.0265

case, i.e. continuous physiological monitoring, this independence assumption can be violated since repeated measurements on the same biological entity may show persistence.

Ignoring such temporal dependence can lead to an underestimation of standard errors, artificially inflating sample size, compressing confidence intervals, and substantially increasing the risk of false positives.

To evaluate the validity of the inferences and test the robustness of the observed treatment contrasts, a sensitivity analysis was conducted. In the following paragraphs, we explicitly review the residual structure of the base model, evaluate within plant temporal autocorrelation, and compare alternative structures with autoregressive terms.

The previous model accounts for hierarchical structure by combining fixed effects (condition, time, and their interaction) with plant specific random intercepts:

$$\begin{aligned}\text{StemFreq}_{ij} = \beta_0 + \beta_1 t_{ij} + \beta_2 \mathbf{1}(\text{Drought}_i) + \beta_3 \mathbf{1}(\text{Fusarium}_i) \\ + \beta_4 t_{ij} \mathbf{1}(\text{Drought}_i) + \beta_5 t_{ij} \mathbf{1}(\text{Fusarium}_i) + b_{0i} + \varepsilon_{ij}\end{aligned} \tag{5.7}$$

where i indexes the individual plant, j indexes the time step, t_{ij} denotes elapsed days, $b_{0i} \sim \mathcal{N}(0, \sigma_b^2)$ is the random intercept, and ε_{ij} is the residual error.

Diagnostic Review of the Naive Residual Structure. Evaluating the naive model assuming independent and identically distributed residuals ($\varepsilon_{ij} \sim \mathcal{N}(0, \sigma_e^2)$, designated as $AR(0)$) reveals severe misspecification. As summarized in Table 5.3, the naive model exhibits an exceptionally high lag-1 residual autocorrelation (Autocorrelation Function(ACF) $ACF_{20m} = 0.987$) and strong 24-hour persistence ($ACF_{24h} = 0.874$). Furthermore, Ljung-Box tests reject residual independence in 100% of the monitored plants ($74/74$, $q_{\text{BH}} < 0.05$). Ignoring this autocorrelation severely understates standard errors, artificially inflating sample sizes and generating false positives and explaining the exceptionally low p-values found in table 5.2.

To address serial correlation without compressing missing data or interpolating missing bins, sensitivity analyses were executed on a 20 minute time step ($174,392$ samples across 74 plants). Candidate correlation structures were evaluated, spanning pure autoregressive processes $AR(p)$ ($p \in \{1,2,3,4,6\}$) and combined models featuring a damped stochastic daily oscillator with a 24-hour period (72 bins of 20 minutes):

Table 5.3 Model selection metrics across residual serial correlation structures on the 20-minute uniform grid.

Model	**AIC**	**ΔAIC**	**ACF_{20m}**	**ACF_{24h}**	**Ljung-Box Reject** ($q < 0.05$)
AR(0) (Naive)	2.6426×10^6	725,740.0	0.9872	0.8744	74 / 74 (100%)
AR(1)	1.9195×10^6	2,644.7	0.0792	0.2651	62 / 74 (83.8%)
AR(2)	1.9191×10^6	2,235.5	0.0264	0.2562	63 / 74 (85.1%)
AR(3)	1.9191×10^6	2,237.3	0.0264	0.2562	63 / 74 (85.1%)
AR(4)	1.9190×10^6	2,093.5	0.0238	0.2519	63 / 74 (85.1%)
AR(6)	1.9187×10^6	1,815.6	0.0232	0.2475	63 / 74 (85.1%)
AR(1)_daily_cycle	1.9170×10^6	110.8	0.0433	0.2295	62 / 74 (83.8%)
AR(2)_daily_cycle	$\mathbf{1.9169 \times 10^6}$	**0.0**	**0.0166**	**0.2266**	**62 / 74 (83.8%)**

As shown in Table 5.3, incorporating autoregressive components dramatically improves relative model fit, reducing AIC by over $725,000$ points. The `AR(2)_daily_cycle` model achieved the lowest overall AIC ($\Delta\text{AIC} = 0$), successfully reducing immediate 20-minute residual autocorrelation to 0.0166. In this model, the daily cycle component accounts for 0.78% of the stationary residual variance ($1 - w = 0.00782$), with an estimated half-life of 13.43 days ($\lambda_d = 0.9497$).

Within-Plant Autocorrelation Across Actual Time Lags. To visually inspect how serial correlation decays over physical time, Figure 5.7 evaluates the mean normalized innovation autocorrelation function (ACF) up to a 48-hour lag.

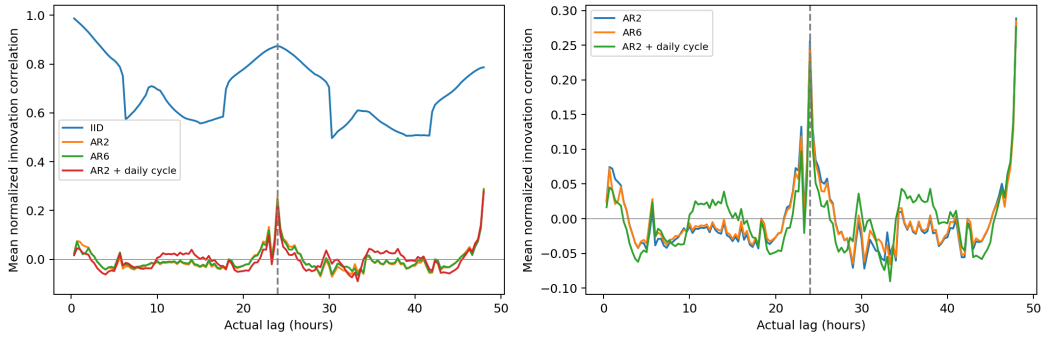


Fig. 5.7 Mean normalized innovation autocorrelation functions (ACF) against actual elapsed time in hours across candidate models. Left: Comparison including the naive IID baseline. Right: Zoomed detail comparing AR(2), AR(6), and AR(2) with a daily cycle. The dashed vertical line marks the 24-hour circadian lag.

The left panel of Figure 5.7 demonstrates the severe misspecification of the naive IID model (blue line), where residual autocorrelation remains extremely high across all lags and peaks sharply at 24 hours ($ACF_{24h} = 0.874$).

While autoregressive structures ($AR(2)$, $AR(6)$, and $AR(2)\_daily\_cycle$) successfully collapse the immediate short-term correlation near zero, the zoomed right panel highlights a critical diagnostic feature: a persistent residual harmonic remains at exactly 24 hours ($ACF_{24h} \approx 0.226$) and 48 hours across all formulations. This remaining daily recurrence provides empirical evidence of unmodeled daily microclimatic forcing or endogenous biological rhythms, confirming that remaining temporal structure must be explicitly acknowledged when interpreting nominal model-based p-values.

Predictive Contribution via Lag Ablation. To quantify the unique predictive value of individual temporal lags, an ablation study was conducted on an 80/20 temporal split per plant. Regression models were trained on the initial 80% of observed data and evaluated on one-step-ahead predictions across the final 20%. Figure 5.8 illustrates the percentage change in held-out Root Mean Squared Error (RMSE) when specific lags or lag blocks are removed conditional on the remaining terms.

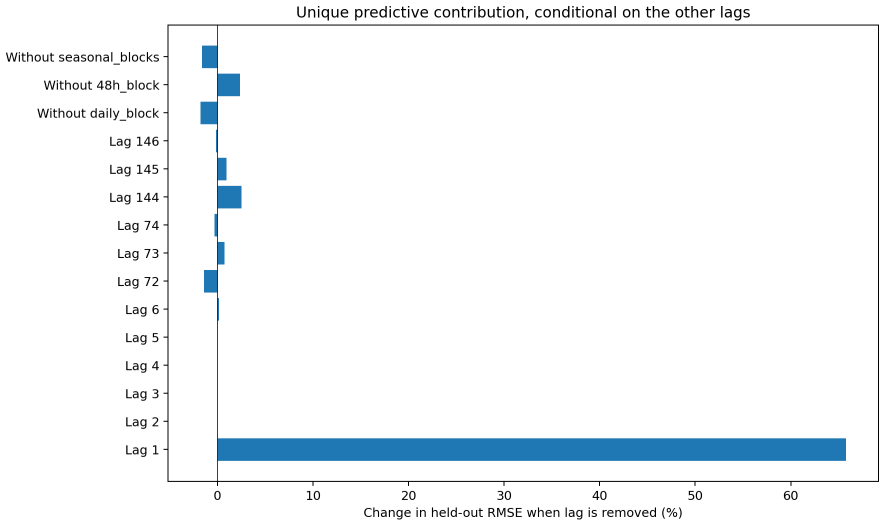


Fig. 5.8 Unique predictive contribution per lag, measured as percentage change in held-out RMSE upon lag removal conditional on other terms.

Impact on Fixed-Effect Inferences and Standard Error Adjustment. Accounting for temporal autocorrelation profoundly alters the statistical inferences regarding treatment trends. Table 5.4 compares the fixed-effect parameter estimates, plug-in Generalized Least Squares standard errors ($\mathrm{SE}_{\mathrm{GLS}}$), standard error inflation ratios relative to $AR(0)$, and plant-clustered robust standard errors ($\mathrm{SE}_{\mathrm{CR1}}$).

Table 5.4 Fixed-effect slope estimates, standard error changes, and nominal p-values across correlation models.

Model	Term	Estimate	$\mathrm{SE}_{\mathrm{GLS}}$	$\mathrm{SE}_{\mathrm{ratio\_vs\_IID}}$	$\mathrm{p}_{\mathrm{GLS}}$	$\mathrm{p}_{\mathrm{plant\_CR1}}$
AR(0)	t_{days}	55.16	1.16	1.00	< 0.001	0.0013
AR(0)	Drought $\times t_{days}$	-172.53	1.99	1.00	< 0.001	< 0.001
AR(0)	Fusarium $\times t_{days}$	-36.72	1.80	1.00	5.07×10^{-92}	0.1798
AR(1)	t_{days}	39.51	34.79	29.95	0.2560	0.0485
AR(1)	Drought $\times t_{days}$	-108.24	56.87	28.64	0.0570	0.0074
AR(1)	Fusarium $\times t_{days}$	-36.58	52.79	29.25	0.4883	0.2020
AR(2)	t_{days}	42.89	32.64	28.10	0.1888	0.0242
AR(2)	Drought $\times t_{days}$	-114.09	53.51	26.95	0.0330	0.0028
AR(2)	Fusarium $\times t_{days}$	-37.13	49.58	27.47	0.4539	0.1788
AR(2)_daily_cycle	t_{days}	**41.23**	**34.52**	**29.72**	**0.2323**	**0.0390**
AR(2)_daily_cycle	**Drought** $\times t_{days}$	**-119.44**	**56.47**	**28.44**	**0.0344**	**0.0038**
AR(2)_daily_cycle	**Fusarium** $\times t_{days}$	**-37.17**	**52.40**	**29.03**	**0.4781**	**0.1921**

Correcting for serial correlation expands the standard errors of slope estimates by approximately **28 to 30 times** ($\mathrm{SE}_{\mathrm{ratio\_vs\_IID}} \approx 28.4 - 29.7$). This correction alters key conclusions:

1. **Baseline Time Trend (t_{days}):** The baseline slope in healthy control plants is no longer statistically significant under GLS ($p = 0.2323$), although a weak effect persists under plant-clustered robust error estimates ($p_{\mathrm{CR1}} = 0.0390$).

2. **Drought Stress Interaction** (Drought $\times t_{days}$)**:** The negative trajectory associated with water restriction remains robust and statistically significant ($p_{\text{GLS}} = 0.0344$, $p_{\text{CR1}} = 0.0038$). Water deficit induces a pronounced, sustained decline in stem frequency.

3. **Fusarium Infection Interaction** (Fusarium $\times t_{days}$)**:** In the naive model, Fusarium infection appeared highly significant ($p = 5.07 \times 10^{-92}$). Once serial correlation is modeled, this effect loses statistical significance entirely ($p_{\text{GLS}} = 0.4781$, $p_{\text{CR1}} = 0.1921$). The apparent significance in the naive model was a false positive driven by unmodeled autocorrelation.

The ablation results confirm that Lag 1 (20 minutes) dominates short-term predictability: removing Lag 1 causes a 65.8% increase in held-out RMSE. Conversely, removing pure daily lag blocks (Lags 72 and 144) produces negligible or slightly negative changes in one-step-ahead prediction error (e.g., -1.77% for removing the daily block). This confirms that while 24-hour periodicity is essential for likelihood fit and structural covariance modeling, short-term physiological inertia (20–40 minutes) carries the vast majority of predictive power.

Residual Distributional Checks and Methodological Caveats. Figure 5.9 displays residual diagnostic plots for the recommended `AR(2)_daily_cycle` model.

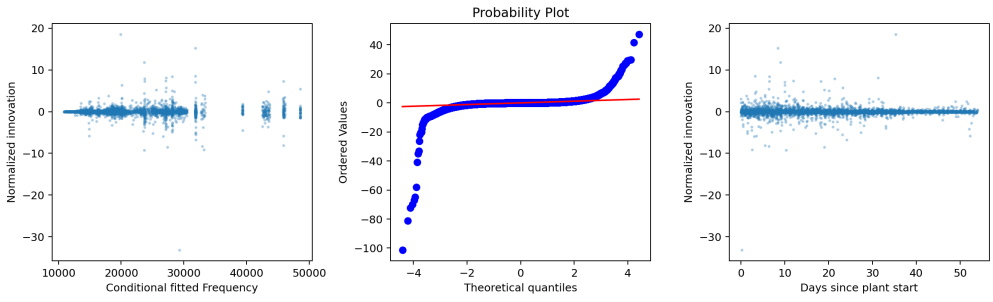


Fig. 5.9 Residual diagnostics for the `AR(2)_daily_cycle` model. Left: Normalized innovations vs fitted frequency. Center: Normal Q-Q probability plot. Right: Normalized innovations over time.

The diagnostic plots highlight persistent model assumptions violations:

- **Heavy Tails and Extreme Outliers:** The normal Q-Q plot (center panel) reveals extreme deviations from Gaussianity, with theoretical quantiles spanning

-100 to $+40$. Normalized innovations exhibit severe skewness (-19.87) and extreme excess kurtosis (1999.8).

- **Unresolved Long-Term Correlation:** Despite optimal AIC ranking, residual autocorrelation at 24 hours remains non-zero ($ACF_{24h} = 0.2266$), and Ljung-Box tests detect residual dependence in 83.8% of plants ($62/74$).

Methodological Caveat on Inference: The reported p-values are nominal and conditional on the fitted covariance model. Substantial residual daily dependence and strongly non-Gaussian innovations remain, including extreme synchronous changes affecting multiple plants simultaneously. Consequently, these p-values should be interpreted as exploratory indicators of average population trends.

5.2.3 Clustering

In the previous analysis, long-term trends in stem frequency revealed a clear response to abiotic stress (drought). Conversely, biotic stress induced by *Fusarium* infection showed no statistically significant divergence from control conditions once temporal autocorrelation was properly accounted for ($p \approx 0.48$).

However, population-average models inherently smooth out plant-specific behaviors and assume a rigid linear interaction over time. Experimental observations in the greenhouse highlighted substantial inter-plant variability in growth rates, baseline conductivity, and individual responses to environmental fluctuations. Furthermore, visual symptom identification by greenhouse operators is often delayed and subjective.

To explore whether unmodeled sub-structures, non linear behaviors, or distinct physiological signatures exist beyond population averages, a time-series clustering approach was adopted. Unlike mixed-effects models unsupervised clustering partitions the raw temporal profiles without imposing ground truth labels. This allows testing whether individual plant responses naturally separate into distinct health states or if high biological heterogeneity dominates the signal structure

In this framework, stem frequency measurements for each plant are treated as individual time series, formally defined as:

$$\{X_t\}_{t \in T} = \{X_1, X_2, X_3, \ldots, X_n\}$$

where X_t denotes the value measured at time t, and $T = \{t_1, t_2, t_3, \ldots, t_n\}$ represents the set of time indices. In this study, the time interval between consecutive measurements ($t_i - t_{i-1}$) corresponds to the sensor sampling time, equal to 10 minutes.

Time series clustering consists in grouping together time series according to a given similarity measure. Formally, given a dataset of n time series $D = \{TS_1, TS_2, \ldots, TS_n\}$, the objective is to partition D into a set of clusters $C = \{C_1, C_2, \ldots, C_k\}$, where each C_i represents a cluster of similar time series.

In this chapter, a shape-based clustering approach is adopted [60], with the aim of identifying stem frequency time series that exhibit similar temporal patterns.

While in the previous analysis measurements were aggregated on a daily basis, here multiple temporal resolutions are considered, specifically: 1, 2, 3, 6, 12, and 24 hours. Since the raw data are sampled every 10 minutes, each temporal resolution is obtained by averaging the measurements within the corresponding time window.

As discussed in [60], a key step in time series clustering is the definition of a distance (or similarity) measure between time series. This can be based on standard metrics such as Euclidean distance (point-wise comparison) or more advanced techniques such as Dynamic Time Warping (DTW). In the present work, DTW [61] is adopted as the similarity measure between time series. DTW is a powerful algorithm that computes the optimal alignment between two time series by allowing non-linear distortions along the time axis. This makes it particularly suitable for comparing time series that may differ in speed or be temporally misaligned, as is often the case for plant growth dynamics observed through stem frequency measurements.

To avoid unrealistic alignments between time series with significantly different durations (e.g., due to shorter experimental iterations), constraints on the warping path and penalty terms are introduced.

Once the pairwise distances between all time series are computed using DTW, a distance matrix is obtained and used as input for an agglomerative hierarchical clustering algorithm.

Agglomerative clustering is a bottom-up hierarchical clustering method in which each time series initially forms its own cluster. At each step, the two closest clusters are merged according to a specified linkage criterion, until a desired number of clusters is reached.

The choice of linkage defines how the distance between clusters is computed. Common linkage strategies include:

- **Single linkage**: distance between the closest elements of two clusters
- **Complete linkage**: distance between the farthest elements
- **Average linkage**: average distance between all pairs of elements
- **Ward linkage**: minimizes the increase in within-cluster variance

In this work, the selected linkage criterion is **average linkage**. The entire procedure is implemented using the *Scikit-learn* library, in particular the `AgglomerativeClustering()` function.

When applying clustering algorithms, it is typically necessary to specify in advance the number of clusters into which the data should be partitioned. However, in many real-world applications,including the present study, this information is not known a priori. For this reason, several clustering evaluation metrics have been proposed, which can be broadly divided into external and internal indices [60].

External indices evaluate the quality of clustering with respect to externally provided labels (in this case, the experimental conditions: healthy, drought, and Fusarium), which represent the ground truth. In contrast, internal indices assess clustering quality without relying on external information, by measuring how similar the elements within each cluster are.

In this analysis, both perspectives are relevant. On the one hand, clustering performance is evaluated with respect to the imposed experimental conditions. On the other hand, it is necessary to determine the most appropriate number of clusters. Indeed, although three experimental conditions are defined, it cannot be assumed a priori that the observed plant responses are naturally separable into exactly three clusters. Such an assumption would be overly restrictive and potentially misleading.

For this reason, the optimal number of clusters k is determined using an internal validation metric, namely the *Silhouette Score*, defined as:

$$s(i) = \frac{b(i) - a(i)}{\max(a(i), b(i))} \tag{5.8}$$

where $a(i)$ is the average distance between sample i and all other points in the same cluster, and $b(i)$ is the minimum average distance between sample i and points in the nearest neighboring cluster.

The Silhouette Score takes values in the range $[0, 1]$, where values close to 1 indicate that a sample is well matched to its assigned cluster and poorly matched to neighboring clusters. In this work, the clustering quality is evaluated by computing the silhouette score for each time series (i.e., each plant) and then averaging over all samples.

This procedure is repeated for different values of k, and the number of clusters that maximizes the average silhouette score is selected as the optimal partition. It is important to note that all pairwise distances between time series are computed using Dynamic Time Warping, as previously described. In addition, the clustering procedure was repeated for different temporal granularities, as previously mentioned (1, 3, 6, 12, and 24 hours), in order to consider not only longer-term trends (as in the case of a 1-day granularity) but also shorter-term behaviors that may provide indications of physiological alterations due to suboptimal plant health conditions.

The results of the clustering procedure described above are reported in Figure 5.10. As a preliminary observation, it can be noted that the optimal number of clusters, as determined by the silhouette score, varies depending on the temporal resolution considered. In particular, for coarser resolutions (12 and 24 hours), the data are better partitioned into three clusters, whereas for finer resolutions (1, 3, and 6 hours), only two clusters are identified as optimal.

1. **24 hours step**: In this case, three main clusters emerge. The first cluster is characterized by a generally increasing stem frequency trend, with the onset of a plateau around the 30th day of measurement. The second cluster exhibits a monotonically decreasing trend, while the third cluster shows an initial increase followed by a decrease after approximately two weeks.

   It is worth noting that the second cluster (central panel) mainly includes plants subjected to stress conditions, with only one healthy plant. This behavior may be explained by plants that experienced stress from the early stages of the experiment, resulting in reduced growth.

   The first cluster (left panel), on the other hand, contains mostly healthy plants, which is consistent with the hypothesis that stem frequency follows plant

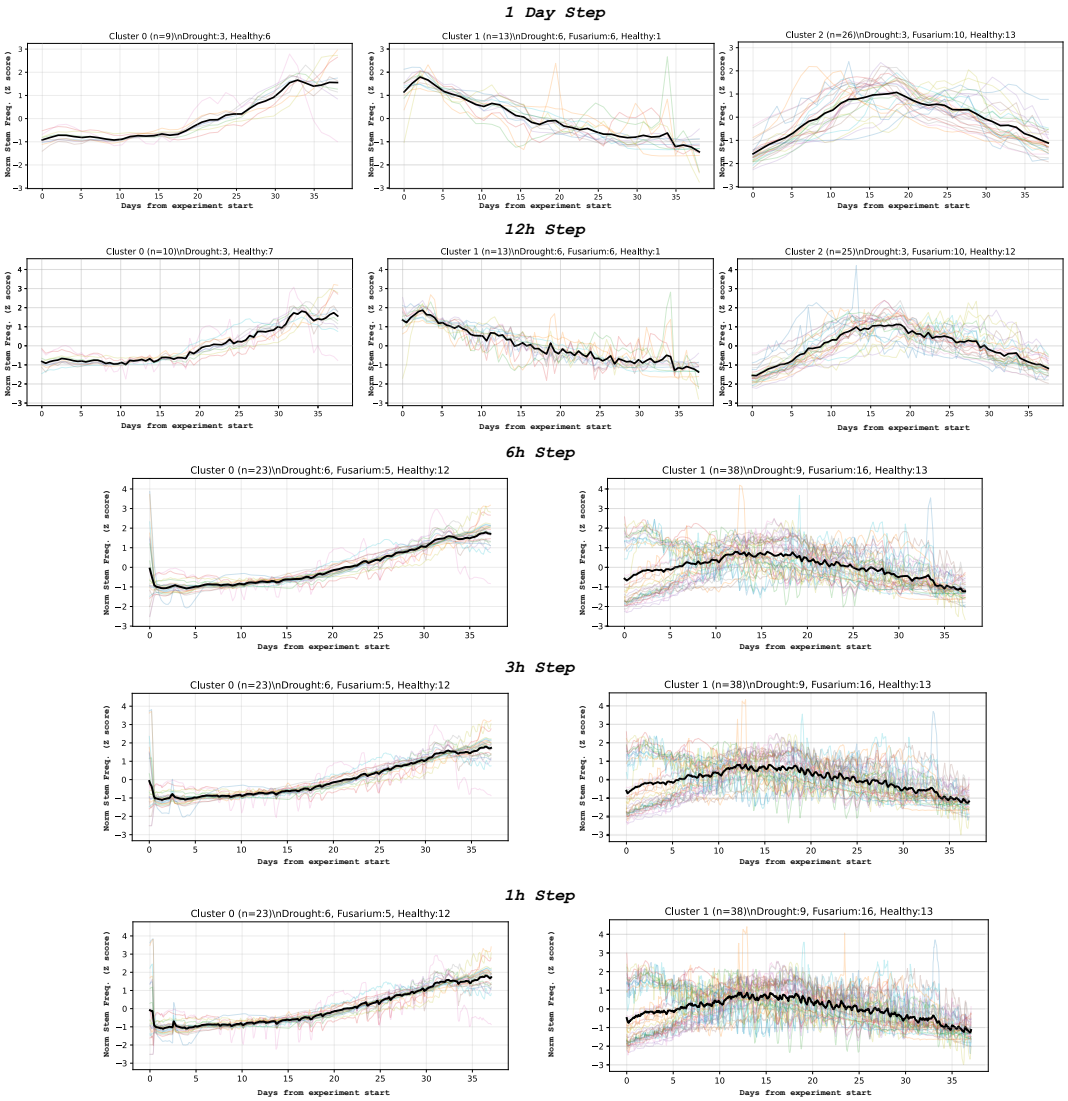


Fig. 5.10 Results of the clustering procedure with different time steps.

growth dynamics. Interestingly, this cluster also includes some drought-stressed plants, suggesting the presence of individuals that are more resilient and able to maintain growth despite suboptimal water availability.

The largest cluster is the third one, which includes the majority of healthy plants as well as many stressed ones, particularly from the Fusarium group. This overlap suggests a greater difficulty in distinguishing biotic stress conditions based solely on stem frequency measurements.

2. **12 hours step**: The results for this temporal resolution are largely consistent with those obtained at the 24-hour scale. However, the measurements

appear noisier, which is expected since a shorter aggregation window reduces the smoothing effect on short-term fluctuations. The same considerations discussed for the 24-hour case therefore apply here.

3. **6 hours step**: Starting from this temporal resolution, the optimal number of clusters reduces to two. The first cluster corresponds to plants exhibiting an increasing trend in stem frequency, which can be associated with higher water content in conductive tissues and overall stem growth.

   The second cluster, as can be observed from the average curve (shown in black), resembles the third cluster identified at coarser resolutions. However, it includes a wide variety of individual behaviors, indicating that the clustering algorithm struggles to clearly separate distinct patterns under these conditions. This is likely due to the higher level of noise present at this temporal resolution, where reduced averaging leads to the preservation of short-term variability in the signal.

4. **3 hours step**: Similar considerations apply as in the 6-hour case. The increased temporal resolution further amplifies signal variability, making it more difficult to distinguish well-defined clusters.

5. **1 hour step**: The same behavior observed for the 6-hour and 3-hour resolutions is confirmed. At this scale, the signal is dominated by short-term fluctuations, which limits the effectiveness of clustering in identifying meaningful long-term patterns.

Integrating the results just analyzed, Figure 5.11 reports the clustering performance in terms of silhouette score for different imposed numbers of clusters, which led to the selection of the optimal number of clusters for each sampling.

With regard to the clustering results and their correspondence with the imposed experimental groups, this can be evaluated using external validation indices, as previously introduced. In particular, the quality of the clustering with respect to the ground truth was assessed using two widely adopted metrics: the Adjusted Rand Index (ARI) and the Normalized Mutual Information (NMI). The ARI measures the agreement between two partitions by considering all pairs of samples and evaluating whether they are assigned to the same or different clusters in both the predicted clustering and the ground truth, correcting for chance. Its values range from -1

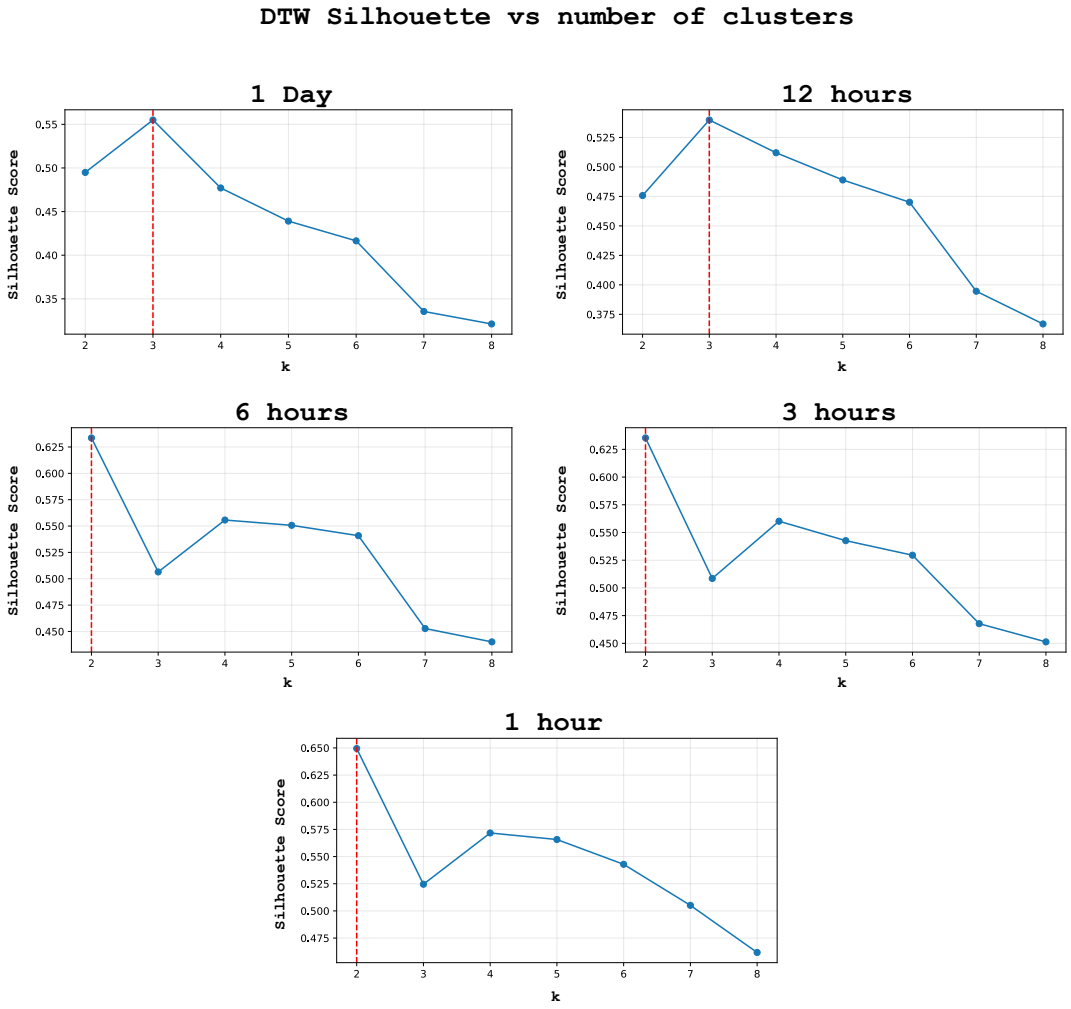


Fig. 5.11 Silhouette score against number of clusters with different time steps

to 1, where 1 indicates perfect agreement, 0 corresponds to random labeling, and negative values indicate worse than random guessing. The NMI, on the other hand, quantifies the mutual dependence between the clustering assignment and the true labels, normalized to yield values between 0 and 1, where higher values indicate better agreement.

As shown in Figure 5.12, both indices take values close to zero across all the analyzed scenarios. This indicates that the identified clusters have little correspondence with the experimental classes, i.e., the ground truth. This observation is consistent with the qualitative inspection of Figure 5.10, where the clusters do not clearly reflect the imposed experimental conditions. These low metrics reframe the unsupervised clustering analysis as a key limiting result. Rather than an algorithmic failure,

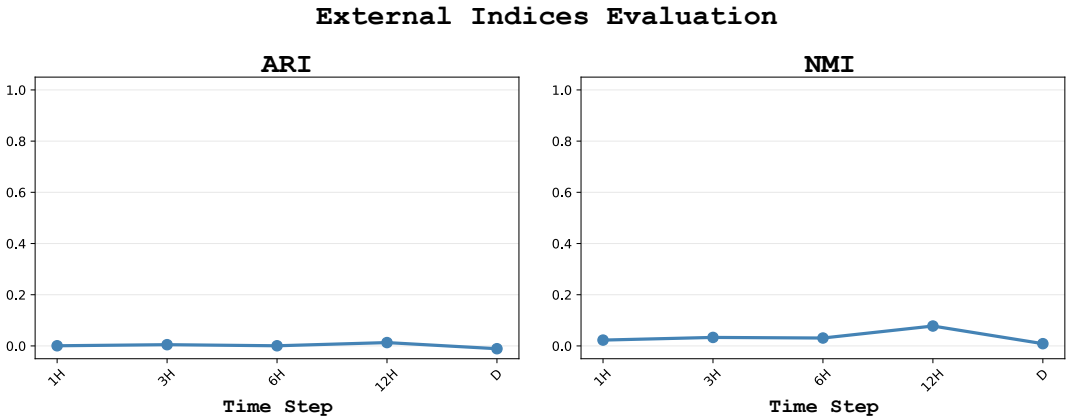


Fig. 5.12 Clustering performance evaluated using external indices (ARI and NMI) across different temporal resolutions.

this demonstrates that raw stem frequency time series lack the individual-level separability required to recover experimental conditions without supervision. High inter-plant variability and overlapping trajectories dominate the uncentered signal.

Moreover, it should be considered that the experiments were conducted in a greenhouse environment where, despite partial control over temperature, environmental conditions still varied depending on the season. For this reason, the analysis was further extended by partitioning the dataset into sub-periods corresponding to individual experimental iterations, hereafter referred to as *blocks*. The previously described clustering procedure was then repeated separately for each block. The results are reported in Figure 5.13.

In this figure, a temporal resolution of 3 hours was selected, as it provides a suitable trade-off between capturing short-term fluctuations and preserving long-term trends, facilitating interpretation.

A first observation is the high variability across different experimental iterations. This is partly due to inconsistencies in experimental protocols. In some cases, experiments were terminated early because plants exhibiting symptoms had already reached a severely compromised state. In other cases, technical issues with the data acquisition system led to premature interruptions (e.g., the last block). Although all data are reported for completeness, results from certain blocks (particularly blocks 0 and 5) should be interpreted with caution due to the limited number of samples. In all cases, clusters are displayed together with color-coded labels indicating the experimental group of each plant.

1. **Block 0**: This block is characterized by a limited number of measurements. As a result, the identified patterns are not clearly distinguishable, especially in the first cluster, making it difficult to draw strong conclusions. The only notable feature appears in the second cluster, where the average trend shows a decrease in stem frequency over time. However, no clear separation among experimental groups is observed.

2. **Block 1**: In this block, measurements span a longer period (approximately one month). Although clustering still does not align well with experimental conditions, more structured patterns emerge. In particular, one cluster (right panel) clearly groups three plants subjected to drought stress, showing a marked decrease in stem frequency following an initial growth phase. The other cluster exhibits an average behavior characterized by initial growth, followed by a plateau and a subsequent decline. This cluster includes both healthy plants and plants infected with Fusarium, highlighting once again the difficulty in distinguishing biotic stress based on stem frequency alone.

3. **Block 2**: In this experimental block, no drought-stressed plants are present, and only a limited number of Fusarium-infected plants are available. Consequently, the clustering results are less robust but still informative. Healthy plants exhibit behaviors that differ significantly from those of the stressed plants. At the same time, their average trend resembles the previously observed pattern, although with a shorter plateau phase.

4. **Block 3**: In this case, one cluster (the second) is composed entirely of stressed plants (one under drought stress and four infected with *Fusarium*). It is interesting to note how their temporal behavior differs markedly from that of the first cluster (left panel), which instead includes only healthy plants (five) and a smaller number of drought-stressed ones (three). Moreover, the behavior of this latter cluster resembles the pattern previously observed for healthy plants, characterized by an initial growth phase that has not yet reached a clear plateau.

5. **Block 4**: In this iteration, three distinct clusters are identified. The first cluster, comprising only healthy and *Fusarium*-infected plants, exhibits a growth–plateau–decline structure similar to that observed previously, although the plateau phase appears significantly shorter. This could suggest that, during

this period, the *Fusarium* infection was actively progressing. The second cluster shows a monotonically decreasing trend over time, with no evident initial growth phase in stem frequency, and consists exclusively of drought-stressed plants. The third cluster includes only healthy plants and displays the typical pattern of initial growth followed by the onset of a plateau. This may indicate slower growth dynamics in these plants, possibly due to intrinsic biological variability. It is worth noting that the experiment was prematurely interrupted, as symptomatic plants had already reached an advanced stage of decline; however, it would have been beneficial to continue monitoring at least the control group.

6. **Block 5**: The final experimental iteration can be considered an outlier. Due to sensor related issues, the measurements were interrupted at an early stage, limiting the amount of information that can be extracted from this dataset. All clusters exhibit very similar trends, with the exception of some spikes at the beginning of the time series, which drive the clustering separation. However, given the limited data quality and duration, it is difficult to draw meaningful conclusions or formulate reliable hypotheses. Therefore, this block will not be analyzed further in detail.

As a final remark, the average temperature and relative humidity measured during each experimental block are also reported. Although greenhouse conditions are partially controlled, they still vary significantly across different seasons. These variations can influence plant development, particularly in the case of biotic stress, as *Fusarium* is known to develop less efficiently at lower temperatures, with an optimal range around 25–28°C.

This effect can be observed in Block 2, where higher average temperatures were recorded and where the temporal patterns of *Fusarium*-infected plants appear more distinctly separated from those of healthy plants. Conversely, in the last block, characterized by lower average temperatures, a reduced differentiation between the observed patterns can be noted. This observation should, however, be interpreted with caution, given the previously discussed limitations affecting the reliability of the final experimental block.

This chapter presented a large experimental campaign conducted in a greenhouse facility across 73 tomato plants, evaluating the application of *stem frequency* mon-

itoring under controlled abiotic (drought) and biotic (*Fusarium oxysporum*) stress conditions.

The key findings and physiological insights derived from this chapter are summarized below:

- **Robust Response to Abiotic Water Stress:** Linear mixed-effects models and long-term trend analyses demonstrated that drought stress induces a statistically significant, progressive reduction in stem frequency ($p_{\text{GLS}} = 0.0344$, $p_{\text{CR1}} = 0.0038$). This decline correlates directly with reduced tissue water content and stem electrical conductivity, appearing up to one week prior to the onset of visible foliar symptoms.
- **Impact of Residual Autocorrelation on Biotic Stress Inferences:** Sensitivity analyses revealed that naive IID modeling severely understates standard errors due to high short-term persistence ($ACF_{20m} = 0.9872$). While naive models suggested a significant effect for *Fusarium* infection ($p \approx 10^{-92}$), adjusting for serial correlation via an $AR(2)$ model with a daily cycle expanded standard errors by $\approx 29\times$, rendering the *Fusarium* interaction statistically non-significant ($p_{\text{GLS}} = 0.4781$). This underscores the critical importance of rigorous covariance structure accounting in continuous physiological monitoring.
- **Biological Heterogeneity vs. Individual Separability:** Unsupervised shape-based time-series clustering (using DTW and average linkage) yielded low agreement with ground-truth experimental classes ($ARI \approx 0$, $NMI \approx 0$). This serves as a key negative finding: population-level statistical contrasts under drought do not easily translate into individual-level diagnostic separability, as baseline biological variability and individual plant growth dynamics dominate uncentered raw signals.

In conclusion, the findings suggest that stem frequency measurement can be able to capture physiological dynamics within the stem, as evidenced by its responsiveness to water deficit. While the current system lacks the sensitivity required to directly detect biotic pathogens such as *Fusarium*, its ability to reliably track water status can still offer practical value. Specifically, it can serve as a cost alternative or complement to traditional soil water potential sensors, helping to rule out abiotic water stress when diagnosing overall plant health. To fully exploit this technology, future experimental

campaigns must focus on expanding the biological sample size and improving the physical reliability of the sensing hardware. Addressing these hardware limitations will be an essential step to elevate measurement stability. Indeed, a key context of this research is that the validation of the stem frequency technique was carried out in parallel with the iterative development and prototyping of the sensing hardware itself. While such hardware related issues and spurious readings were an inevitable part of evaluating an emerging technology, they nonetheless constrained the volume of usable data and limited the statistical scope of this study.

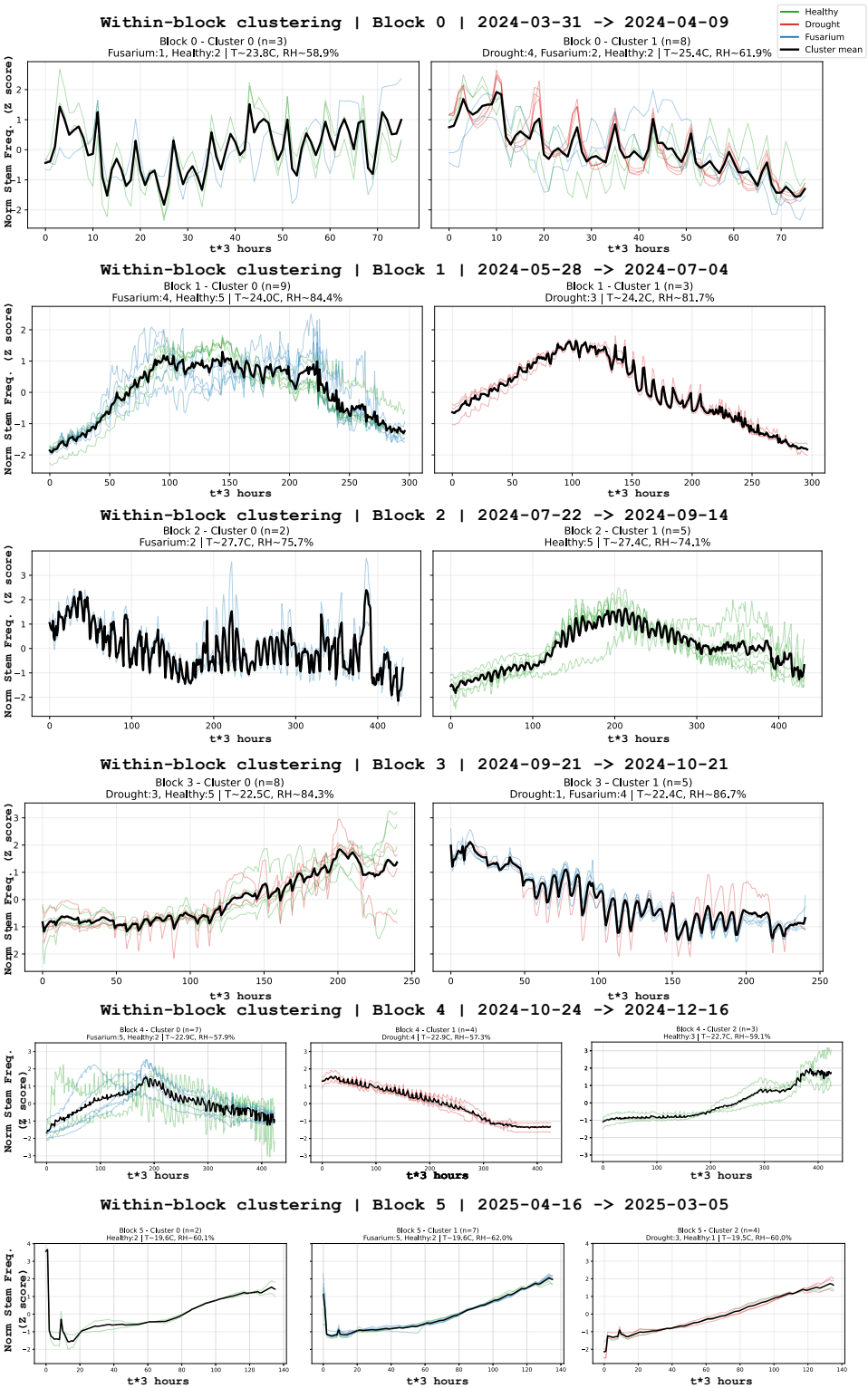


Fig. 5.13 Clustering results within individual experimental blocks at 3-hour temporal resolution.

Chapter 6

Open Field Long Term Measurements

The primary objective of this chapter is to present a preliminary evaluation of the proposed stem frequency setup for continuous, long-term (years scale) monitoring of apple trees in a professional orchard. In this final section, a measurement campaign of stem frequency is analyzed on plant species that differ substantially from those considered in the previous chapters. Up to this point, the analysis focused on herbaceous plants with soft stems, such as tomatoes. Here, instead, a preliminary long-term dataset, collected over several months, is presented for apple trees in a professional orchard. Another major difference lies in the experimental environment. Unlike the controlled conditions adopted in previous analyses, this study was conducted in open field conditions. This setting is closer to a realistic deployment scenario for monitoring a cultivar under operational conditions. The results presented in this chapter are based on a joint work carried out with Mattia Barezzi and published in [62]. It is important to emphasize the exploratory nature of this campaign. The dataset comprises measurements from only two individual apple trees ($n = 2$), corresponding to one monitored plant per experimental location (F2_CV2 and F2_EX2), without true biological replication per treatment arm. Consequently, the findings presented in this chapter are intended to demonstrate technical feasibility, signal stability, and preliminary alignment with known seasonal physiology, rather than to derive statistically generalizable conclusions for the entire cultivar.

6.1 Experimental Setup

The system described in the previous chapters for measuring stem conductivity through stem frequency [34] was employed to monitor apple trees in a professional orchard.

The main modification with respect to the previous setup concerns the electrodes. Due to the presence of bark, the use of small needle electrodes was not feasible. Therefore, two stainless steel nails were inserted into the trunk, approximately 15 cm apart. Each nail was inserted to a depth of about 2.0 cm, allowing contact with the internal vascular tissue while minimizing mechanical damage. Stainless steel was selected due to its resistance to oxidation and its biocompatibility.

In addition, as previously mentioned, the system is equipped with an HDC2080 sensor [57], enabling the measurement of air temperature and relative humidity. Data are transmitted via the LoRa protocol, allowing continuous in-field monitoring of trunk frequency. The sampling interval was set to 10 min. Additional environmental data were obtained from the WAPPSEN system, described in [19], in particular soil water potential measurements at two depths (-20 cm and -40 cm), acquired using TEROS21 sensors from METER Group [42]. The experimental site, described in [18], consists of two fields, referred to as CV2 and EX2. In each field, multiple measurement locations are present: some include both trunk frequency and WAPPSEN measurements, while others include only WAPPSEN data. For this analysis, only the locations equipped with trunk frequency sensors were considered, referred to as F2_CV2 and F2_EX2.

The objective of this section is to evaluate the effectiveness of the proposed setup for continuous, long-term (year-scale) monitoring of apple trees in a professional orchard and to investigate its relationship with environmental variables such as air temperature, relative humidity, and soil matric potential. Electrical bio-impedance and stem frequency measurements can be related to soil matric potential, enabling an indirect assessment of plant health status, as highlighted in previous studies [34, 63].

6.2 Methodology

Previous analyses primarily focused on tomato plants; however, this study targets a fundamentally different species. Beyond the required adaptation of the electrodes, apple trees and tomato plants differ significantly in their physiology and growth dynamics.

Apple trees are perennial plants, while tomato plants are herbaceous annuals that complete their life cycle within a single growing season. Furthermore, apple trees develop a deeper and more extensive root system, enabling a more effective exploration of the soil. In contrast, tomato plants have a more superficial root system, making them more susceptible to environmental stresses, particularly water stress. Growth dynamics also differ substantially, with apple trees exhibiting slower and more gradual development. Since apple trees are perennial deciduous species, their physiological behavior is strongly influenced by seasonal changes. In particular, they undergo dormancy during the cold season, as widely documented in the literature [64, 65].

The analysis focuses on both long-term variations (weeks to months) and short-term (daily) dynamics of trunk frequency. Data were collected from April 16th, 2024, to May 15th, 2025. Measurements acquired between April 16th and June 1st, 2024, were excluded from the analysis due to the wound healing process following electrode insertion; this aspect will be discussed in a later section.

Trunk frequency data were decomposed into long-term trend and seasonal components using STL seasonal-trend decomposition procedure based on locally estimated scatterplot smoothing (LOESS) [66]. In the following, the term *seasonal* refers to periodic behavior, primarily at a daily scale. To avoid ambiguity, the term *astronomical seasonality* will be explicitly used when referring to variations associated with the four seasons of the year. Given the variability in both environmental conditions and plant physiology across astronomical seasons, the analysis was divided into the following periods:

- **Winter**: December 1st 2024 to February 28th 2025;
- **Spring**: March 1st 2025 to May 31st 2025;
- **Summer**: June 1st 2024 to August 31st 2024;

- **Autumn**: September 1st 2024 to November 30th 2024.

STL is capable of capturing time varying trends and seasonal components; however, it implicitly assumes the presence of a consistent seasonal structure in the data, which may not always hold. For this reason, a strategy inspired by [67] was adopted to assess the presence of a significant seasonal component. For each astronomical season, seasonality strength was evaluated using a periodogram. A seasonality index was defined as the ratio between the amplitude of the dominant daily component and the sum of all other frequency components. Higher values of this index indicate a stronger daily periodic behavior in trunk frequency measurements.

6.2.1 Wound Healing after insertion

Inserting two needles into a mature apple plant causes physical damage to its tissue, and the effects, unlike in the previously presented experiments with tomato plants presented in chapters 4 and 5, are clearly visible in the measurements immediately after installation. As stated earlier, each needle was inserted for around 2 cm, with the electrodes placed 15 cm apart. Thinner needles increase the likelihood of breakage when in contact with the plant's woody structure. The two trunk frequency sensors were installed on April 16th 2024.

Figure 6.1 shows the data collected during the initial months from the two monitored plants, one at the EX2 site and the other at the CV2 site.

A significant amount of signal noise is evident for approximately the first one to one and a half months. This is likely due to the time needed for the mature apple trees to establish a stable interface with the stainless steel electrodes. Consequently, the analysis begins on June 1st 2024.
The insertion was done without wound sealants. Wound sealants, such as grafting mastic or pruning paste, are applied to plant injuries to promote healing, prevent infections, and protect the exposed tissue from pests and environmental stress. Their usage in the insertion operation could reduce the required recovery time.

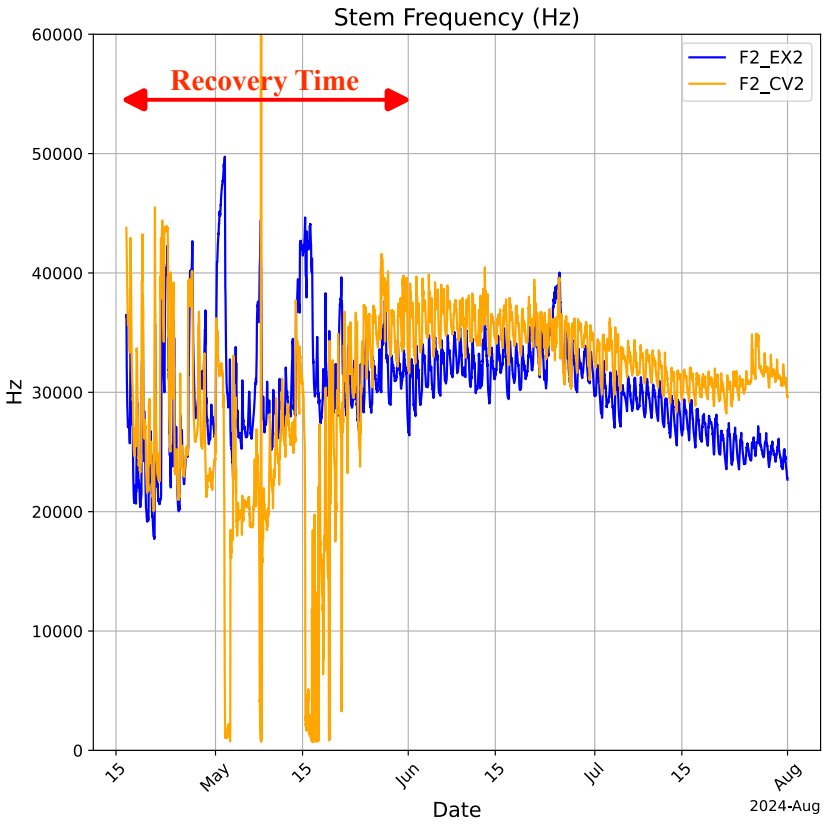


Fig. 6.1 Trunk frequency raw values recorded from April 16th 2024, the installation day. During the healing period, a significant amount of signal noise from the trunk sensors can be observed.

6.3 Data Collection Results and Analysis

The results of the data collection, together with the seasonal-trend decomposition segmented by loose astronomical seasons, are presented in figure 6.2. These are shown in relation to the environmental conditions surrounding the plants, namely air temperature, relative humidity, soil water potential, and day–night cycles.

To assess the presence and intensity of seasonal components, particularly daily ones associated with plant circadian rhythms, an additive decomposition of the trunk frequency signal was performed using STL. Mathematically, the acquired signal x_t was decomposed as:

$$x_t = T_t + S_t + R_t \tag{6.1}$$

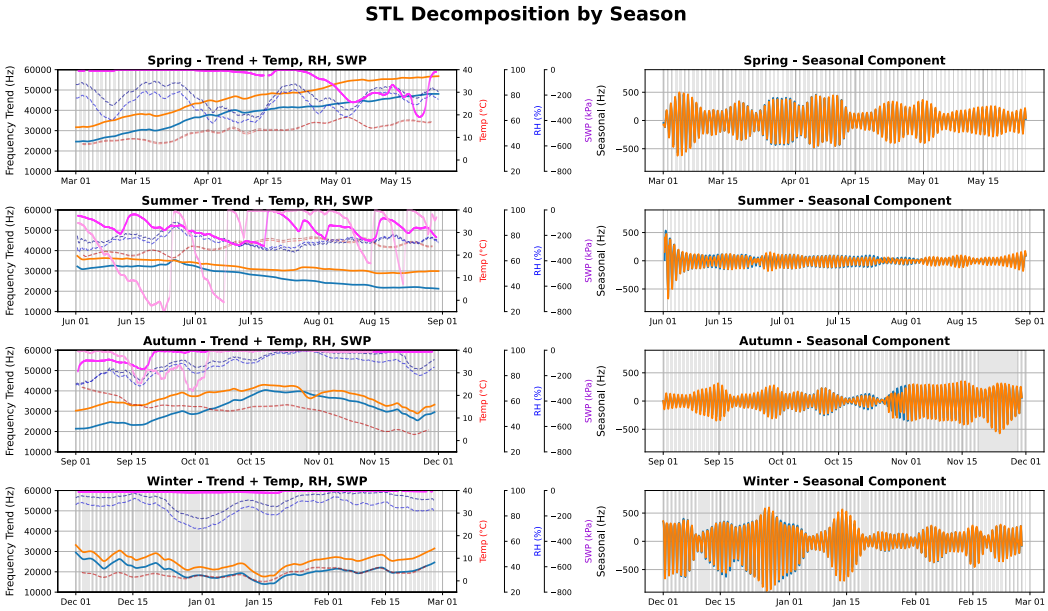


Fig. 6.2 Overview of trunk frequency measurements and corresponding environmental variables (air temperature, relative humidity, soil water potential, and day–night cycles), along with STL decomposition segmented by astronomical seasons.

where T_t represents the long-term trend, S_t the seasonal component, and R_t the residual term.

The analysis then focused on evaluating the presence of a daily seasonality, i.e., a recurring 24-hour cycle in trunk frequency, and on investigating how this component varies across different astronomical seasons. Once the periodic short-term component S_t was obtained, its spectral content was analyzed to quantify the contribution of the daily cycle and to verify that the extracted seasonality was not an artifact of the STL algorithm. Starting from S_t, a periodogram was computed using the `periodogram()` function from the Python `scipy` library [68]. This allowed the estimation of the spectral power density $P(f)$. In particular, the spectral power corresponding to a 24-hour periodicity, denoted as P_{24}, was considered. To quantify the strength of the daily component, a seasonality index s_{24} was defined as the ratio between P_{24} and the total spectral power excluding the 24-hour contribution:

$$s_{24} = \frac{P_{24}}{\sum_k P(f_k) - P_{24}}. \tag{6.2}$$

The results of this index, computed for each astronomical season, are reported in Table 6.1. As expected, the behavior of the analyzed plants varies across different astronomical seasons.

Table 6.1 Seasonality index by season and plant

Pseudo Astronomical Season	Plant 1	Plant 2
Summer	0.29	0.41
Spring	4.94	6.37
Autumn	2.70	2.04
Winter	2.16	2.14

Winter

The bottom subplot pair in figure 6.2 presents the measurements collected during the winter period. Air temperature generally decreased steadily until the second week of January, with average values remaining below 5 °C. Relative humidity generally ranged between 70% and 90%, partly influenced by rainfall events. These rain events positively affected soil hydration, as indicated by soil water potential values consistently close to 0 kPa (values of soil water potential close to 0 indicate wet soil, while drier conditions result in more negative values). In summary, the climate during this period was characterized by cold and humid conditions. The plot in the left-most winter section also shows the trend extracted through the decomposition procedure: trunk frequency, reflecting the conductivity of the plant's trunk section, steadily decreased until the second week of January, following a pattern similar to that of air temperature. The moderate-high overall winter seasonality index for both plants reported in table 6.1 indicates that overall during this season, daily behavior is present; however, the magnitude of it varies, as can be observed in figure 6.2. The intensity of the seasonal component during winter exhibits higher values till the third week of January, followed by an overall reduction.
The dormancy of apple trees during winter is a well-known mechanism; during this period, apple trees gradually enter a dormant phase in which photosynthetic activity and nutrient flow are significantly reduced. This behavior is consistent with the trends observed in both apple trees analyzed: a generally decreasing trend is evident up to the third week of January, followed by a reversal in the trend thereafter.
In the seasonal component plot (right-most plot in the winter section), a higher daily

activity is noticeable in both plants during the initial part of the period (as indicated by the amplitude of the seasonal component), which then transitions into a phase of reduced activity.

Spring

Spring measurements are shown in the top subplot pair in figure 6.2. Overall, air temperature increased steadily throughout spring, leading into summer. During this time, temperatures remained above 6–7 °C. Specifically, early spring was characterized by temperatures ranging between 6 and 8 °C; in late spring, temperatures rose to settle on average between 16 and 18 °C. Air humidity measurements were constantly above 60%, with periods near 90% due to rainfall events. During spring, apples accumulate chill hours (hours with the temperature above 7 °C), and when a certain quantity is reached, the dormancy period ends. During this period, it is expected an increase of photosynthetic activity, nutrients and water flow through the trunk.
During the analyzed spring period, the trunk frequency sensor recorded a constant and stable upward trend, indicating a gradual increase in trunk conductivity, suggesting a higher presence of nutrients, consistent with the hypothesis of dormancy break and the onset of vegetative growth. Furthermore, the seasonal component plot for the spring period shows generally higher activity compared to the preceding winter dormancy phase, confirmed also by high values of seasonality index in table 6.1 for both plants (4.94 and 6.37).

Summer

Summer showed higher temperatures, relative humidity around 70–80%, and strongly negative soil water potential values, indicating limited water availability in the field. The trend of trunk frequency decreases and no longer follows the temperature trend as it did in previous seasons. Interestingly, the seasonal plot revealed a reduced daily component compared to other astronomical seasons, further confirmed by the magnitude of the seasonality index in table 6.1 (0.24 and 0.41), indicating, likely due to prolonged hot weather conditions combined with limited water availability.

Autumn

During autumn, temperature measurements show a gradual decrease, and relative humidity exhibits an increase associated with rainfall events. These precipitation events also contribute to an overall increase in soil water potential, indicating improved water availability in the field. In response to these changing climatic conditions, a general upward trend in trunk frequency is observed, suggesting increased conductivity up to the first days of November. This behavior can be attributed to reduced water stress following the dry summer period, resulting in greater nutrient flow within plant tissues. As environmental stress decreases, the plant likely restores its internal water balance, improving physiological function and increasing trunk conductivity. Looking at the seasonal component graph, we noticed a general activity increase compared to the summer period and, within autumn itself, a generally higher activity starting from November till the beginning of winter.

6.3.1 Summary and Main Limitations

This chapter demonstrated the long-term field deployment of the trunk frequency monitoring system on two mature apple trees in a commercial orchard. Following an initial tissue recovery phase of approximately 1.5 months after nail electrode insertion, the sensors maintained continuous operational stability over an uninterrupted monitoring period of one year. To the best of the author's knowledge, this represents one of the few continuous, multi-seasonal *in-vivo* bio-impedance datasets collected on fruit trees under real-world open-field conditions.

The preliminary results showed trunk bio-impedance dynamics that align remarkably well with established physiological milestones in deciduous fruit trees, including winter dormancy, spring vegetative reactivation, and summer water-stress dampening. The quantified seasonality index (s_{24}) reflected these transitions, dropping from high values during peak spring growth (4.94 and 6.37) to minimal values during the dry summer period (0.29 and 0.41). Despite these promising qualitative and spectral alignments, the scope of these findings must be interpreted strictly within their preliminary context:

- **Lack of Biological Replication:** The current dataset is limited to two single trees ($n = 1$ per site), preventing formal statistical testing of treatment contrasts or cross-plant variance components.
- **Confounding Factors:** In open-field conditions, atmospheric drivers (temperature, vapor pressure deficit), soil water matric potential, and intrinsic physiological phenology operate simultaneously, making causal attribution challenging without larger cohorts.

Consequently, this campaign serves as a technical validation of the non-invasive trunk frequency methodology for multi-season tree monitoring. Future experimental iterations must expand the sample size to multi-plant cohorts per treatment block to enable robust inferential modeling and disentangle environmental forcing from plant physiological status.

Chapter 7

Conclusions and future works

This concluding chapter provides a synthesis of the experimental campaigns, analytical frameworks, and methodological findings presented throughout this dissertation. The core objective of this doctoral research was to systematically evaluate the diagnostic capacity of *stem frequency* as in vivo sensing parameter for real time plant health monitoring.

7.1 Synthesis of Experimental Findings

The validation strategy was designed as a progression, moving from controlled microclimates to complex, operational environment (i.e open field):

- **Climate Chamber Experiments (Chapter 4):** Initial trials established the baseline physical response of stem frequency under strictly regulated environmental conditions. The primary finding was that under optimal hydration, stem frequency tracks ambient microclimatic drivers (temperature and relative humidity). However, upon reaching critical soil water potential thresholds, this environmental coupling breaks down, producing distinct signal deviations that signal the onset of abiotic stress.
- **Greenhouse Campaigns (Chapter 5):** Scaling the validation to a larger biological cohort (73 tomato plants), this stage introduced both abiotic (drought) and biotic (*Fusarium oxysporum*) stress factors. Linear mixed effects modeling confirmed a statistically significant population-level decline in stem frequency

under water deficit ($p < 0.05$ after $AR(2)$ autocorrelation adjustment). Conversely, biotic stress induced by *Fusarium* did not yield a statistically separable signal once serial correlation was accounted for. Furthermore, unsupervised time series clustering revealed high inter plant heterogeneity, demonstrating that uncentered raw signals do not automatically separate into ground truth health states without baseline calibration.

- **Long-Term Field Deployment (Chapter 6):** The sensing architecture was deployed in an operational apple orchard for over a full year. This extended field deployment provided an acceptable experimental campaign for the mechanical and electrical durability of the stem frequency sensor across seasonal weather variations, freezing temperatures, and annual phenological transitions, confirming that stem frequency tracks long-term vascular activity and transpiration trends over macro-temporal scales.

7.2 Explicit Statement of Original Contributions

The primary scientific contributions of this doctoral work include:

1. **Multi Environment Validation:** Taking an emerging sensing technique beyond initial laboratory experiments and validating it across increasingly complex, real-world agricultural settings.
2. **Assessment of Sensor Capabilities:** Quantifying the actual diagnostic performance of stem frequency, clearly establishing its statistical validity for detecting abiotic water deficit while rigorously demonstrating its current limitations in discriminating specific biotic stresses (*Fusarium*).

7.3 Demonstrated Capabilities vs. Unproven Hypotheses

It is essential to specify what has been proven by this thesis from what remains unproven:

- **What Has Been Demonstrated:** Stem frequency measurement is a viable, and cost effective proxy for detecting abiotic water deficit situations in tomato plants. It can serve as a functional alternative or complement to traditional soil water potential sensors for ruling out drought stress. Furthermore, long term operational viability (>1 year) in orchard environments has been successfully proven.
- **What Remains Unproven:** The current methodology does not yet demonstrate reliable, individual plant diagnosis or stress specific classification. The system cannot currently discriminate between abiotic drought and early stage biotic fungal infections (*Fusarium*) at the single plant level without additional contextual data.

7.4 Methodological Limitations

The main limitations encountered during this research stem from both biological variability and hardware prototyping challenges:

- **Biological Heterogeneity and Unmodeled Dynamics:** Intrinsic biological variations—such as differences in stem geometry, baseline vascular conductivity, and individual plant vigor—introduced high inter-plant variance. Furthermore, physiological trends in healthy tomato plants (e.g., initial growth, plateau, decline) strongly mirror crop evapotranspiration coefficients (K_c), suggesting that unmodeled metabolic or transpiration dynamics heavily influence the raw signal.
- **Co-Evolution of Hardware and Validation:** Because experimental testing was conducted in parallel with early-stage prototype development, spurious readings, signal drift, and sensor degradation led to the exclusion of several plant replicates, limiting the effective sample size and statistical power of certain sub-trials.
- **Integration of Sensor Dynamics with Visual Observations:** Combining continuous stem frequency monitoring with daily visual data.

7.5 Future Work and Research Outlook

The author believe future efforts should focus on:

1. **Sensor Robustness and Hardware Iteration:** Upgrading hardware platform reliability to prevent data loss, eliminate spurious readings, and ensure more consistent future experimental campaigns.
2. **Complementary Ground Truth Validation:** Integrating non invasive or minimally invasive physiological metrics (such as SPAD chlorophyll indices, stomatal conductance, and destructive biomass sampling) to cross validate stem frequency trends against definitive biological ground truth indicators.
3. **Multivariate & Machine Learning Integration:** Fusing stem frequency signals with local microclimatic parameters within multivariate predictive frameworks or machine learning architectures to improve single plant stress identification and classification.

In conclusion, while stem frequency sensing is not ready for immediate, uncalibrated disease diagnosis, it represents a promising, low cost tool for monitoring plant water status and supporting daily irrigation management.

References

[1] ICT International. *SFM1 Sap Flow Meter User Manual (Version 5.2)*, 2023.

[2] Nicola Coppedè, Michela Janni, Manuele Bettelli, Calogero Leandro Maida, Francesco Gentile, Marco Villani, Roberta Ruotolo, Salvatore Iannotta, Nelson Marmiroli, Marta Marmiroli, and Andrea Zappettini. An in vivo biosensing, biomimetic electrochemical transistor with applications in plant science and precision farming. *Scientific Reports*, 7(1):16195, November 2017.

[3] Luca Rolle. Signal amplitude monitoring system for in-plant communication based on multi-source energy harvesting: design and characterization. Master's thesis, Politecnico di Torino, 2023. Accessed: 2026-04-19.

[4] IRROMETER Company, Inc. Soil moisture sensors - irrometer, 2025. Accessed: 2026-04-08.

[5] Ritchie, Hannah, Roser, Max, and Rosado, Pablo. Co_2 and greenhouse gas emissions by sector, 2020. Our World in Data.

[6] World Resources Institute. 4 charts explain greenhouse gas emissions by countries and sectors, 2020.

[7] Ritchie, Hannah, Roser, Max, and Rosado, Pablo. Water stress, 2020. Our World in Data.

[8] Hannah Ritchie. Food production is responsible for one-quarter of the world's greenhouse gas emissions. *Our World in Data*, 2019. Accessed: 2025-04-29.

[9] Ritchie, Hannah and Roser, Max. Climate change, 2020. Our World in Data.

[10] Robert KD Peterson and Leon G Higley. Biotic stress and yield loss. 2000.

[11] Prachi Pandey, Vadivelmurugan Irulappan, Muthukumar V. Bagavathiannan, and Muthappa Senthil-Kumar.

[12] United Nations. United nations, 2026.

[13] Alexandru Lavric and Adrian Ioan Petrariu. LoRaWAN communication protocol: The new era of IoT. In *2018 International Conference on Development and Application Systems (DAS)*, pages 74–77, May 2018.

[14] LoRa Project. Lora documentation. https://lora.readthedocs.io/en/latest/, 2025. Accessed: 2026-02-03.

[15] Thomas N. Buckley. How do stomata respond to water status? *New Phytologist*, 224(1):21–36, 2019.

[16] S. Neill, R. Barros, J. Bright, R. Desikan, J. Hancock, J. Harrison, P. Morris, D. Ribeiro, and I. Wilson. Nitric oxide, stomatal closure, and abiotic stress. *Journal of Experimental Botany*, 59(2):165–176, February 2008.

[17] Mattia Barezzi, Alessandro Sanginario, Davide Canone, Davide Gisolo, Alessio Gentile, Luca Nari, Francesca Pettiti, and Umberto Garlando. Wappfruit—an automatic system for drip irrigation in orchards based on real-time soil matric potential data. *IEEE Transactions on AgriFood Electronics*, 2(2):293–305, 2024.

[18] Mattia Barezzi, Umberto Garlando, Francesca Pettiti, Luca Nari, Davide Gisolo, Davide Canone, and Danilo Demarchi. Long-range low-power soil water content monitoring system for precision agriculture. In *2022 IEEE 13th Latin America Symposium on Circuits and System (LASCAS)*, pages 1–4, 2022.

[19] Mattia Barezzi, Umberto Garlando, Francesca Pettiti, Luca Nari, Davide Gisolo, Davide Canone, and Danilo Demarchi. Long-range low-power soil water content monitoring system for precision agriculture. In *2022 IEEE 13th Latin America Symposium on Circuits and System (LASCAS)*, pages 1–4, 2022.

[20] Mattia Barezzi. *Smart Electronic Systems for Precision Agriculture*. Phd thesis, Politecnico di Torino, 2025.

[21] L. Pereira, Rick Allen, Paula Paredes, Ramón López-Urrea, Dirk Raes, Martin Smith, Ayse Kilic, and Salman Maher. Crop evapotranspiration – guidelines for computing crop water requirements. second edition, revised 2025. fao irrigation and drainage paper, no. 56 rev.1. rome, fao., 03 2026.

[22] Zhe Gu, Zhiming Qi, Rasika Burghate, Shouqi Yuan, Xiyun Jiao, and Junzeng Xu. Irrigation scheduling approaches and applications: A review. *Journal of Irrigation and Drainage Engineering*, 146:04020007–1 15, 03 2020.

[23] Sha Huang, Lina Tang, Joseph P. Hupy, Yang Wang, and Guofan Shao. A commentary review on the use of normalized difference vegetation index (NDVI) in the era of popular remote sensing. *Journal of Forestry Research*, 32(1):1–6, February 2021.

[24] Alanna V. Zubler and Jeong-Yeol Yoon. Proximal Methods for Plant Stress Detection Using Optical Sensors and Machine Learning. *Biosensors*, 10(12):193, December 2020.

[25] Implexx. Implexx sap flow sensor, 2026.

[26] Martin Thalheimer. A leaf-mounted capacitance sensor for continuous monitoring of foliar transpiration and solar irradiance as an indicator of plant water status. *Journal of Agricultural Engineering*, November 2022.

[27] Michela Janni, Nicola Coppede, Manuele Bettelli, Nunzio Briglia, Angelo Petrozza, Stephan Summerer, Filippo Vurro, Donatella Danzi, Francesco Cellini, Nelson Marmiroli, Domenico Pignone, Salvatore Iannotta, and Andrea Zappettini. *In Vivo* Phenotyping for the Early Detection of Drought Stress in Tomato. *Plant Phenomics*, 2019:6168209, January 2019.

[28] Chiara Diacci, Tayebeh Abedi, Jee Woong Lee, Erik O. Gabrielsson, Magnus Berggren, Daniel T. Simon, Totte Niittylä, and Eleni Stavrinidou. Diurnal *in vivo* xylem sap glucose and sucrose monitoring using implantable organic electrochemical transistor sensors. *iScience*, 24(1):101966, January 2021.

[29] Stefano Calvo. *Plant-Wearable Electronics for Climate-Smart Agriculture: Toward Energy-Autonomous Bio-Impedance Monitoring Systems*. Doctoral dissertation, Politecnico di Torino, 2025.

[30] Federico Cum, Luca Alfarano, Massimo Pugliese, Danilo Demarchi, and Umberto Garlando. Preliminary analysis of biotic and abiotic stress on tomato plants using impedance measurements and time series clustering. In *2024 IEEE 2nd Conference on AgriFood Electronics (CAFE)*, pages 125–129, 2024.

[31] Umberto Garlando, Stefano Calvo, Mattia Barezzi, Alessandro Sanginario, Paolo Motto Ros, and Danilo Demarchi. Ask the plants directly: Understanding plant needs using electrical impedance measurements. *Computers and Electronics in Agriculture*, 193:106707, 2022.

[32] Umberto Garlando, Lee Bar-On, Paolo Motto Ros, Alessandro Sanginario, Stefano Calvo, Maurizio Martina, Adi Avni, Yosi Shacham-Diamand, and Danilo Demarchi. Analysis of in vivo plant stem impedance variations in relation with external conditions daily cycle. In *2021 IEEE International Symposium on Circuits and Systems (ISCAS)*, pages 1–5, 2021.

[33] U. Garlando, L. Bar-On, P. M. Ros, A. Sanginario, S. Peradotto, Y. Shacham-Diamand, A. Avni, M. Martina, and D. Demarchi. Towards optimal green plant irrigation: Watering and body electrical impedance. In *2020 IEEE International Symposium on Circuits and Systems (ISCAS)*, pages 1–5, 2020.

[34] Stefano Calvo, Mattia Barezzi, Danilo Demarchi, and Umberto Garlando. In-vivo proximal monitoring system for plant water stress and biological activity based on stem electrical impedance. In *2023 9th International Workshop on Advances in Sensors and Interfaces (IWASI)*, pages 80–85, 2023.

[35] Umberto Garlando, Lee Bar-On, Paolo Motto Ros, Alessandro Sanginario, Stefano Calvo, Maurizio Martina, Adi Avni, Yosi Shacham-Diamand, and Danilo Demarchi. Analysis of in vivo plant stem impedance variations in relation with external conditions daily cycle. In *2021 IEEE International Symposium on Circuits and Systems (ISCAS)*, pages 1–5, 2021.

[36] European Commission. Farms and farmland in the european union, 2025.

[37] ISPRA. Aziende e superficie agricola utilizzata, 2024.

[38] Aralab. Fitoclima 600–1200 stability testing chambers, 2024. Environmental reach-in chambers for stability testing with temperature range -5 to 60 °C and humidity control from 20% to 95% RH.

[39] Stefano Calvo, Mattia Barezzi, Danilo Demarchi, and Umberto Garlando. In-vivo proximal monitoring system for plant water stress and biological activity based on stem electrical impedance. In *2023 9th International Workshop on Advances in Sensors and Interfaces (IWASI)*, pages 80–85, June 2023.

[40] Texas Instruments. *LMC555 CMOS Timer*. Texas Instruments, 2024. Datasheet.

[41] Mattia Barezzi, Alessandro Sanginario, Davide Canone, Davide Gisolo, Alessio Gentile, Luca Nari, Francesca Pettiti, and Umberto Garlando. Wappfruit—an automatic system for drip irrigation in orchards based on real-time soil matric potential data. *IEEE Transactions on AgriFood Electronics*, 2(2):293–305, 2024.

[42] METER Group. Teros 21 soil water potential sensor, 2024. Accessed: 2026-04-26.

[43] Redmond Ramin Shamshiri, James W Jones, Kelly R Thorp, Desa Ahmad, Hasfalina Che Man, and Sima Taheri. Review of optimum temperature, humidity, and vapour pressure deficit for microclimate evaluation and control in greenhouse cultivation of tomato: a review. *International agrophysics*, 32(2):287–302, 2018.

[44] Dietmar Schwarz, Andrew J. Thompson, and Hans-Peter Kläring. Guidelines to use tomato in experiments with a controlled environment. *Frontiers in Plant Science*, Volume 5 - 2014, 2014.

[45] S. Sato, M. M. Peet, and J. F. Thomas. Physiological factors limit fruit set of tomato (Lycopersicon esculentum Mill.) under chronic, mild heat stress. *Plant, Cell & Environment*, 23(7):719–726, 2000.

[46] Organisation des Nations Unies pour l'alimentation et l'agriculture, Société internationale de la science horticole, and Centre national pour la recherche agricole et la vulgarisation, editors. *Good Agricultural Pratices for Greenhouse Vegetable Crops: Principles for Mediterranean Climate Areas*. Number 217 in FAO Plant Production and Protection Paper. FAO, Rome, 2013.

[47] NumPy Developers. numpy.polyfit — numpy documentation, 2026. Accessed: 30 March 2026.

[48] S Zolnier, R.S Gates, J Buxton, and C Mach. Psychrometric and ventilation constraints for vapor pressure deficit control. *Computers and Electronics in Agriculture*, 26(3):343–359, May 2000.

[49] Joseph Redmon, Santosh Kumar Divvala, Ross B. Girshick, and Ali Farhadi. You only look once: Unified, real-time object detection. *CoRR*, abs/1506.02640, 2015.

[50] Ultralytics. Ultralytics yolo. https://github.com/ultralytics/ultralytics, 2025. Accessed: 2026-04-16.

[51] Roboflow. Roboflow: Computer vision platform, 2025. Accessed: 2026-04-16.

[52] Wikipedia. Gaussian blur. Accessed: 2026-04-16.

[53] Adam Paszke, Sam Gross, Francisco Massa, Adam Lerer, James Bradbury, Gregory Chanan, Trevor Killeen, Zeming Lin, Natalia Gimelshein, Luca Antiga, et al. Pytorch: An imperative style, high-performance deep learning library. In *Advances in Neural Information Processing Systems*, volume 32, 2019.

[54] PyTorch Contributors. torch.optim.adamw — pytorch documentation. https://docs.pytorch.org/docs/stable/generated/torch.optim.AdamW.html, 2025. Accessed: 2026-04-16.

[55] H Schuhl, KE Brown, H Sheng, PK Bhatt, J Gutierrez, D Schneider, AL Casto, L Acosta-Gamboa, JG Ballenger, F Barbero, et al. Plantcv v4: Image analysis software for high-throughput plant phenotyping. *Plant Phenome Journal*, 9:e70065, 2026.

[56] Federico Cum, Luca Alfarano, Massimo Pugliese, Danilo Demarchi, and Umberto Garlando. Lstm neural networks anomaly detection for biotic and abiotic early stress detection on tomato plants. *IEEE Transactions on AgriFood Electronics*, 3(2):348–356, 2025.

[57] Texas Instruments. HDC2080 Low-Power Humidity and Temperature Sensor. https://www.ti.com/product/HDC2080, 2024. Accessed: 2026-04-18.

[58] Xavier A. Harrison, Lynda Donaldson, Maria Eugenia Correa-Cano, Julian Evans, David N. Fisher, Cecily E.D. Goodwin, Beth S. Robinson, David J. Hodgson, and Richard Inger. A brief introduction to mixed effects modelling and multi-model inference in ecology. *PeerJ*, 6:e4794, May 2018.

[59] Statsmodels Developers. MixedLM: Linear Mixed Effects Models, 2024. Accessed: 2026-04-21.

[60] Saeed Aghabozorgi, Ali Seyed Shirkhorshidi, and Teh Ying Wah. Time-series clustering – a decade review. *Information Systems*, 53:16–38, 2015.

[61] Pavel Senin. Dynamic time warping algorithm review. *Information and Computer Science Department University of Hawaii at Manoa Honolulu, USA*, 855(1-23):40, 2008.

[62] Federico Cum, Mattia Barezzi, Danilo Demarchi, and Umberto Garlando. Preliminary analysis of trunk electrical bio-impedance in professional apple orchards. In *2025 IEEE Conference on AgriFood Electronics (CAFE)*, pages 1–5, 2025.

[63] Umberto Garlando, Stefano Calvo, Mattia Barezzi, Alessandro Sanginario, Paolo Motto Ros, and Danilo Demarchi. A "plant-wearable system" for its health monitoring by intra- and interplant communication. *IEEE Transactions on AgriFood Electronics*, 1(2):60–70, 2023.

[64] Jake J. Grossman. Phenological physiology: seasonal patterns of plant stress tolerance in a changing climate. *New Phytologist*, 237(5):1508–1524, 2023.

[65] Benjamin K. Blackman. Changing responses to changing seasons: Natural variation in the plasticity of flowering time. *Plant Physiology*, 173(1):16–26, 11 2016.

[66] Robert B Cleveland, William S Cleveland, Jean E McRae, Irma Terpenning, et al. Stl: A seasonal-trend decomposition. *J. off. Stat*, 6(1):3–73, 1990.

[67] Imre Cseresnyés, Anna Füzy, Sándor Kabos, Bettina Kelemen, K. Rajkai, and Tünde Takács. Monitoring of plant water uptake by measuring root dielectric properties on a fine timescale: diurnal changes and response to leaf excision. *Plant Methods*, 20, 01 2024.

[68] Pauli Virtanen, Ralf Gommers, Travis E. Oliphant, Matt Haberland, Tyler Reddy, David Cournapeau, Evgeni Burovski, Pearu Peterson, Warren Weckesser, Jonathan Bright, Stéfan J. van der Walt, Matthew Brett, Joshua Wilson, K. Jarrod Millman, Nikolay Mayorov, Andrew R. J. Nelson, Eric Jones, Robert Kern, Eric Larson, C J Carey, İlhan Polat, Yu Feng, Eric W. Moore, Jake VanderPlas, Denis Laxalde, Josef Perktold, Robert Cimrman, Ian Henriksen, E. A. Quintero, Charles R. Harris, Anne M. Archibald, Antônio H. Ribeiro, Fabian Pedregosa, Paul van Mulbregt, and SciPy 1.0 Contributors. SciPy 1.0: Fundamental Algorithms for Scientific Computing in Python. *Nature Methods*, 17:261–272, 2020.